Mochammad Agoes Moelyadi

Stage Separation Aerodynamics of Future Space Transport Systems

Lehrstühl für Aerodynamik
der Technischen Universität München

TECHNISCHE UNIVERSITÄT MÜNCHEN

aer Lehrstuhl für Aerodynamik

Lehrstuhl für Aerodynamik
Technische Universität München

Stage Separation Aerodynamics of Future Space Transport Systems

Mochammad Agoes Moelyadi

Vollständiger Abdruck der von der Fakultät für Maschinenwesen der Technischen Universität München zur Erlangung des akademischen Grades eines

Doktor-Ingenieurs

genehmigten Dissertation.

Vorsitzender : Univ.-Prof. Dr. rer. nat. Ulrich Walter

Prüfer der Dissertation :

1. Univ.-Prof. Dr. -Ing. Boris Laschka, em.
2. Univ.-Prof. Dr. -Ing. habil. Nikolaus A. Adams
3. Prof. Dr. i.r. H. R. Harijono Djojodihardjo, Sc.D., Univ. Al Azhar, Jakarta / Indonesien

Die Dissertation wurde am 28.03.2006 bei der Technischen Universität München eingereicht und durch die Fakultät für Maschinenwesen am 05.09.2006 angenommen.

ACKNOWLEDGEMENTS

Many thanks need to go out, it is a monumental accomplishment for me to graduate. I would like to express firstly my utmost gratitude to God for His Help and Bounty and to my loving parents, Mochammad Sutadi and Murdaningsih, as well as my parents in law, Mochammad Faisal and Nuriah.

I am very thankful to my supervisor, Univ.-Prof. Dr.-Ing. Boris Laschka, em., for giving me opportunity to work on this interesting research field and for his pioneering work on unsteady aerodynamics which served as a starting point for my doctoral research at Technical University München and also for his invaluable advice and discussion during the research time. My honourable thanks must also go out to Univ.-Prof. Dr. -Ing. Gottfried Sachs for his encouragement and support and for his valuable advice and discussion. It is also my worthy thanks to Prof. Dr. Harijono Djojodihardjo for kindly help to conduct the research here and for his advice and discussion in the beginning research time. My special thanks go to Univ.-Prof. Dr.-Ing Nikolaus A. Adams who heads of the institute of Aerodynamics giving me the support during the final time of my writing. I would also like to thank Dr.-Ing. Christian Breitsamter for spending countless hours trying to help me understand the space vehicle problems and for his generosity and help.

I would also like to thank all my friends at Technical University München, Dipl.-Ing. A. Allen, Dipl.-Ing. M. Iatrou, Dipl.-Ing. L. Jiang, W. Sekar, M.Sc., Dr.-Ing. U. Sickmüller, Dipl.-Ing. A. Pechloff, Dipl.-Ing. C. Bellastrada, Dipl.-Ing. A. Schmid, Dipl.-Ing. R. Reß and also all my colleges in the Institute of Aerodynamics. This work would not have been possible without their friendship and their helpful discussions and suggestions on both the technical and non-technical topics.

Most importantly, I cannot thank enough my loving wife, Ratna Dewi Angraeni for her endless support and patience. To my son, Ihsanuddin, and my daughters, Qonita and Tazkiya, thank you for giving me so much happiness.

München, September 2006 Mochammad Agoes Moelyadi

ABSTRACT

Steady and unsteady Euler investigation is carried out to simulate the unsteady flow physical phenomena on the complex geometry of two stage space transportation system during a separation phase. The dynamic computational grids and local smoothing techniques as well as the solution of unsteady Euler equations based on the finite explicit finite volume shock capturing method are used to obtain accurate unsteady flow solution. The staging path is approached with the one-minus-cosine function applied for the relative angle of attack and relative distance. The effects of numerical factors on flow solution including grid density and grid smoothing are investigated. The results obtained include the static pressure contours on symmetry plane as well as on the aerodynamic coefficients of the orbital and carrier stages that are compared to the corresponding experimental data.

Zusammenfassung

Stationäre und instationäre Euler Untersuchungen werden durchgeführt, um die physikalischen Phänomene der instationären Strömungen auf der komplexen Geometrie des zweistufigen Raumtransportsystems während der Trennungsphase zu simulieren. Die dynamischen Rechengitter und das lokale Glätten sowie die instationäre Euler Lösung, die auf der expliziten Finite Volumen Methode mit *shock capturing* basiert, werden verwendet, um genaue stationäre und instationäre Strömungslösungen zu erreichen. Der Lösungsweg wird mit dem “1 minus cosine“- Gesetz angenähert, das auf den relativen Anstellwinkel und den relativen Abstand angewendet wird. Die Effekte auf die Strömungslösung durch numerische Faktoren wie Gitterpunktdichte und Gitterglättung werden analysiert. Die erzielten Resultate schließen die Druck Verteilungen in der Symmetrieebene sowie die aerodynamischen Beiwerte der Ober- und Unterstufe ein. Sie werden mit entsprechenden experimentellen Daten verglichen.

LIST OF CONTENTS

*) Two Stage to Orbit

LIST OF FIGURES

LIST OF TABLES

NOMENCLATURE

ABBREVIATION	Meanings
AUSM	Advection Upstream Splitting Method
CAD	Computer-Aided Design
CCD	Charged Coupled Device
CFD	Computational Fluid Dynamics
CFL	Courant-Friedrichs-Lewy number
CUSP	Convective Upwind Split Pressure
ELAC1C	Elliptical Aerodynamic Configuration 1C
EOS	ELAC Orbital Stage
FLM	Fluid Mechanics
ICEM	Integrated Computer Engineering and Manufacturing
ISTP	Integrated Space Transportation Plan
ITAM SB RAS	Institute of Theoretical and Applied Mechanic of the Siberian Branch of the Russian Academy of Science
JAXA	Japan Aerospace Exploration Agency
LDFSS	Low-Diffusion Flux-Splitting Scheme
MAPS	Mach number–based Advection Pressure Splitting
NURBS	Non-Uniform Rational B-Splines
PC	Personal Computer
RANS	Reynolds Averaged Navier-Stokes
RLV	Reusable Launch Vehicle
SSTO	Single-Stage To Orbit
TSTO	Two-Stage To Orbit
TVD	Total Variation diminishing

SYMBOL	Meanings	The first used in page
Bold Latin Letters:		
F, **G**, **H**	mass flux curvilinear and dimensionless coordinate system	24
P	source terms in grid smoothing	35
Q	state variables in curvilinear and dimensionless coordinate system; source terms in grid smoothing	24
R	right hand side equation (residual); source terms in grid smoothing	35
f, g, h	convective mass flux in Cartesian coordinate system	22
$\mathbf{h_{KOS}}$	distance between EOS and flat plate or ELAC1C	25
q	vector of conservative variables	22
r	coordinate vector	35
$\mathbf{X_{EOS}}$, $\mathbf{Y_{EOS}}$, $\mathbf{Z_{EOS}}$	axes of Cartesian coordinate system of EOS vehicle	25
$\mathbf{X_{ELAC}}$,$\mathbf{Y_{ELAC}}$, $\mathbf{Z_{ELAC}}$	axes of Cartesian coordinate system of ELAC 1C vehicle	26
Normal Latin Letters:		
C_D	total drag coefficient	30
C_L	total lift coefficient	30
C_M	total pitching moment coefficient	30
C_X	total axial force coefficient	30
C_Z	total normal force coefficient	30
CFL	Courant-Friedrichs-Lewy number	52
D	drag	30
H	total enthalpy	42
J	Jacobi matrix for the coordinate transformation	148
L	lift	30
M	pitching moment	30

M_∞	Free-stream Mach number	28
M	advective Mach number in AUSM scheme	42
R	gas constant	23
S	surface area of a control volume cell	42
$Sref$	reference area	30
T	absolute temperature	23
U, V, W	contravariant velocities	149
V_∞	free stream velocity	30
a	speed of sound	42
b_{EOS}	EOS span	26
c_p	pressure coefficient	71
c_p	specific heat at constant pressure	23
c_v	specific heat at constant volume	23
e	specific internal energy	23
g^{ij}	contravariant metric coefficient with superscripts I,j=1,2,3	35
g_{ij}	covariant metric coefficient with subscripts I,j=1,2,3	155
h	enthalpy	23
h/l_{EOS}	relative distance for the EOS and ELAC1C	25
k_{red}	reduced frequency	28
$l_{ref,}$ l_{EOS}	reference length of EOS	26
l_μ	mean aerodynamic chord (MAC)	30
n_x , n_y „ n_z	components of normal vector of the surface of control volume	22
p	air pressure	23
p_∞	free stream air pressure	28
q_∞	dynamic pressure	30
s	limiter function	46
s_x , s_y „ s_z	components of surface vector	43

$\vec{t}$	tangential vector	49
t	real physical time	28
t^*	pseudo-time	53
$\vec{v}$	velocity vector	49
u, v, w	velocity components	22
x, y, z	cartesian coordinates	22
$\dot{x}, \dot{y}, \dot{z}$	speed of cell face	150

Greek Leters:

$\Delta\alpha$	relative angle of attack	26
$\Lambda_{\xi,}\Lambda_{\eta,}\Lambda_{\zeta}$	characteristic values of Jacobi matrix	52
Φ	numerical dissipation coefficient	42
Ω	control volume	22
α	angle of attack; stage coefficient for Runge-Kutta scheme	26
γ	ratio of the specific heats	23
δ	numerical dissipation parameter in AUSM	44
ε	residual error; parameter in AUSM to suppress limiting of solution	46
κ	control of accuracy in MUSCL scheme	45
ξ, η, ζ	curvilinear coordinates	24
ρ	density	23
ρ_∞	free stream density	28
τ	time in curvilinear coordinates	24
φ_l	lower bow shock angle	83
φ_u	upper bow shock angle	83
υ	numerical dissipation parameter in AUSM	44
ω	numerical dissipation parameter in AUSM	44

Upper Indices:

Mod AUSM	index for modified AUSM	44
VL	index for van Leer formular	44

Lower Indices:

L	index for the left side	160
R	index for the right side	160
i, j,k	integer index for the point in curvilinear coordinates	40
$k + \frac{1}{2}$	index for the point	40
∞	index for free stream	28
0	reference state	49

Other Symbols:

$\vec{\nabla}$	nabla vector	49

GLOSSARY

Schlieren Picture	An image that is obtained by blocking portions of light that have been refracted through a fluid density gradient.
Shadowgraph	An optical method of rendering fluid flow pattern visible by using index of refraction differences in the flow. The fluid is usually illuminated by a parallel beam of ligt.
Strain-gauge balance	A device for measuring all components of aerodynamic forces and moments that are working based on the principle of a deformation (strain) in the body/ balance.

CHAPTER I
INTRODUCTION

1. Overview

In the globalization era, the growing demands on new space transportation systems such as Unmanned Space Vehicles (USV) and future generation Reusable Launch Vehicles (RLV) have pulled research activities in many hypersonic technological areas in many institutions all over the world [1][2][3]. In the United States, NASA has put the second generation RLV as a major program of the Integrated Space Transportation Plan (ISTP) with 4.8 B$ spent to run this program covering the period 2001-2006 [4]. In Europe several system studies were conducted since the 90's to investigate possible concepts for a European RLV. Some of the national programs (e.g. SAENGER, STAR-H, TARANIS) favour to investigate the concepts of Two-Stage To Orbit (TSTO) systems instead of Single-Stage To Orbit (SSTO) vehicles [1]. A similar program is also being performed in Japan by the institution of Japan Aerospace Exploration Agency (JAXA). This institution has conducted the High-Speed Flight Demonstrator project as the latest in a series of flight experiment in a research program for reusable space transportation systems [5].

Efforts to develop such hypersonic transportation systems until this time have been performed in Europe with substantial advancements in lightweight, high temperature structural materials, thermal protection systems, propulsion systems, etc. Particularly, in Germany, intensive efforts dealing with the key technologies for a two-stage space transportation system have been supported by three research centers (Sonderforschungsbereich, SFB), namely SFB 253 (RWTH Aachen), SFB 255 (TU München) and SFB 259 (University of Stuttgart). In particular, unsteady aerodynamics has been studied and Euler and Navier-Stokes as well have been developed for that project at the Institute of Fluid Mechanics under its chair Prof. Dr. Ing. B. Laschka. At the Technische Universität

München the researchs efforts have been focused on Transatmospheric Flight Systems including fundamentals of aerothermodynamics, powerplants and flight Mechanics. The design concept of a fully two-stage hypersonic vehicle deals with a delta-winged first stage powered by airbreathing engines and a rocket-propelled upper stage [6], see Fig. I.1. The concept was initiated by the idea of E. Sänger. According to Sänger's concept the upper and lower stages are designed as high lift over drag vehicles [2].

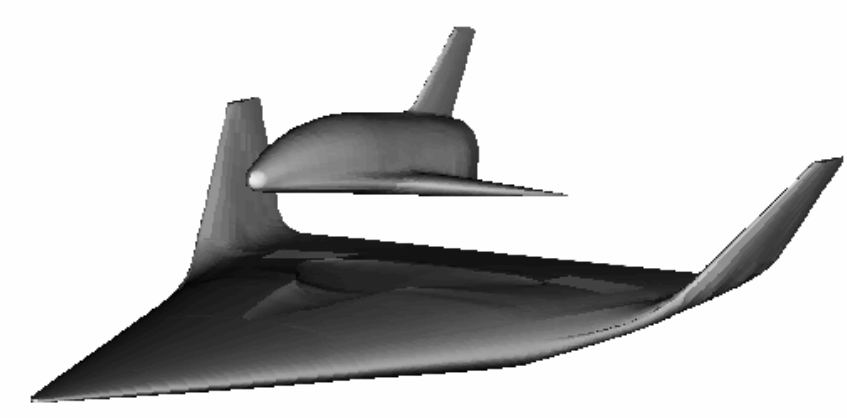

Figure I.1: Layout of two-stage to orbit (ELAC-EOS) configuration

Such a space vehicle has a flight mission consisting of three phases each of which showing specific characteristics as shown in Fig. I.2.

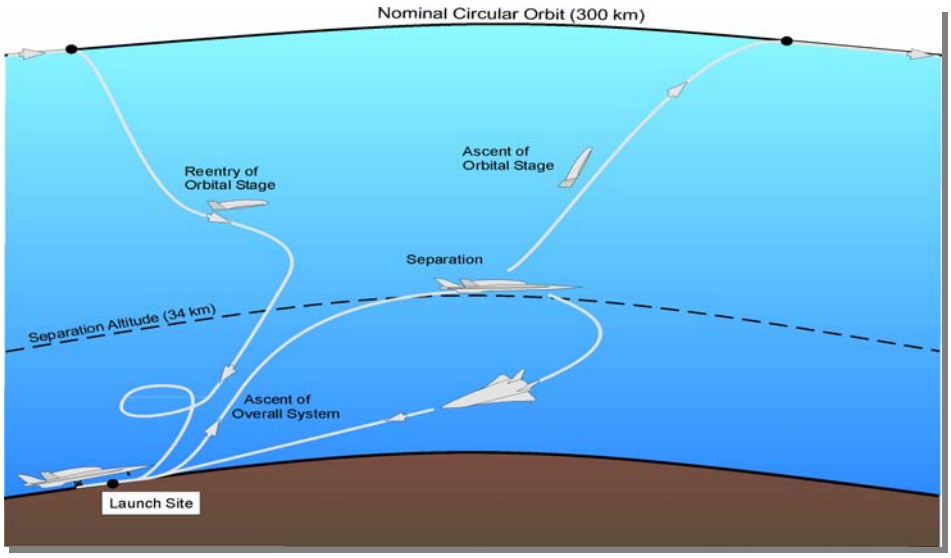

Figure I.2: A flight mission of the two stage space transportation system [Ref. 7]

The first phase is defined as the “Pull-up phase”, the orbital stage is mounted on the top of the hypersonic aircraft. It is launched horizontally to reach the flight speed of Mach about 6.8 at altitudes of 35 km. At this altitude the orbital stage is released and the “Separation process” starts as the second phase. The orbital stage separates from the carrier stage until the “Stand-alone flight” phase takes place at which no interaction occurs between the stages. The upper stage continues the ascent to the orbit while the lower stage flies back to its launch site like an aircraft. After the mission of the orbiter is accomplished it also returns to earth through re-entry and landing like the Space Shuttle [8][9]. Among the phases of the ascent flight mission the separation manoeuvre will be the most critical one for the vehicle system. In such a phase, very high dynamic pressures about 18.100 N/m^2 are subject to the space vehicle system. Under these conditions aerodynamic interferences occur between the stages, namely complex interactions of incident and reflected shockwaves and expansion waves with each other as well as with boundary layers. Furthermore, the separation process influences the position and intensity of the shockwaves and also the points of interaction of the reflected shockwaves which provides strong unsteady air-loads on both stages. This may have an impact on the stability of the vehicle during the separation manoeuvre causing a hazard during the space vehicle operation.

In order to guarantee a safe separation of two-stage space transportation system, investigation on the configuration aerodynamics are mainly required, particularly to describe flow fields and to determine aerodynamic characteristics such as aerodynamic forces and moments for the flight conditions during separation. In addition, unsteady aspects of the separation and the amplitude and phase of aerodynamic forces should be considered. By this investigation the results of aerodynamic data can be of great importance for other fields of hypersonic research (e.g. structure mechanics,

flight performances, stability and controls, propulsions, thermodynamics) at a realization of the designed hypersonic transport system.

There are three techniques be used to obtain aerodynamic data for hypersonic vehicles, namely flight testing, wind tunnel experiment and numerical computation. The aerodynamic data collection from a flight testing is costliest as compared to the two other techniques because of the necessity to build a space vehicle demonstrator with its supporting system facilities and operating costs. However, in November 2004, NASA has been just successful to fly the ummanned X-43A vehicle at Mach number of 10 dropped from a converted B-52 bomber at an altitude of 33.5 km. This Hyper-X program with 41.6 M$ was intended to test the “Scramjet” engine in flight [10]. Morever, wind tunnel experiments for the two-stage space vehicle systems have been conducted in Refs. [11][12]. They were intended to provide the aerodynamic data base of the two-stage space transport systems for the steady flow state. However, unsteady flow measurements of the stage separation of the vehicle have not yet been accomplished due to the very high operational cost of the wind tunnel. Alternatively, the aerodynamic data for the vehicle may be obtained using a computational method. Such methods have been widely developed as a tool for design and analysis of numerous aerodynamic configurations of the space vehicles. However, the unsteady problems of two-stage space transportation systems at the separation manoeuvre still require thorough computational investigations, especially for complex configurations and flow phenomena.

Therefore, this dissertation focuses on unsteady stage separation of the full two-stage space transportation configuration by means of computational method. This introductory chapter presents the problems and challenges of the unsteady aerodynamic simulations for space vehicles, the progress in analysis of hypersonic space transport systems, the objectives and scope of the problem solution and the methodology applied.

2. Problems and Challenges in the Computational Simulations of Unsteady Stage Separation of Two-Stage Space Transport Systems.

In this investigation the computational simulations dealing with unsteady stage separation of two-stage space transport systems have two main problems, namely:

(1) the complex geometry of the two-stage space transport systems.

(2) the complex physical flow phenomena involving unsteady flows in hypersonic speed during the separation process.

The detail descriptions of these problems are given as follows.

The complexity of two-stage space transport systems is indicated by the presence of two vehicles at once arranged as the upper and lower stages as shown in Fig. I.1. Besides this, both the configurations have different designs for shape and size in order to fulfill the requirements of the flight mission [2][8]. The lower stage called as carrier stage has two and half times of the total length of the upper stage which is referred as an orbital stage. The carrier stage is designed with a sharp nose, while the orbital stage has a blunt nose. In turn, the carrier stage body is designed as a slender blended wing-body shape like a wave rider with the fixed swept winglets. And in the middle part of the upper surface of the carrier stage a large cavity is made to place the orbital stage. In addition, the lower surface of the carrier stage was designed as a ramp due to the placement of air breathing propulsion. Moreover, the orbital body was designed as a circular cross section like the space shuttle equipped with a delta wing and vertical stabilizer. The presence of some lifting surface components such as the wing tip of the carrier stage and the highly swept wing of the orbital stage have made some researchers [13][14] perform some simplifications in simulating the two-stage space vehicle, namely by cutting off the rear part of the carrier stage where the wing tips are located. The wing tips cause the computational grid to be more complex. This problem requires appropriate building of block topologies in the physical domain.

Concerning the separation process, the orbital stage is initially placed at a certain incident angle and distance, lifted up using a strut mechanism from the carrier stage. Then, the orbital stage itself moves up along a given trajectory until it reaches the stand-alone condition. In the beginning of separation, the flow field at the region above the cavity of the carrier stage is accommodated with aerodynamic interferences due to the interactions of incident and reflected shockwaves and expansion waves with each other as well as with boundary layers. The flow field becomes increasingly complex when the down wash effects appear during the separation process. Then, the unsteady stage separation problems occur as seen in the change of the position and intensity of the shockwaves as well as the interaction points of the reflected shockwaves. This causes strong unsteady airloads on both stages.

These stage separation problems have been successfully investigated using available solver code (FLM solver) for the configuration of two-stage space vehicle system with an idealized flat plate for the carrier stage [7][14][15] and [16]. However, for the full configuration of two-stage space vehicle the solver code can not be directly applied because it has been developed based on the global physical domain solution in which the whole grids are assumed to be moving. While, in the case of unsteady stage separation on the full configuration of TSTO space vehicle, the part of mesh around the carrier stage is stationary, and the part of mesh around the orbital stage is moving. Therefore, to perform the calculations of the unsteady problem, a further development of the code is necessary to be developed. In addition, the improvement of grid quality in the moving region requires the local grid smoothing instead of the global grid smoothing which is used in the previous flow solver.

Subsequently, flow phenomena relating to viscous effects of air occur at regions close to the body, namely boundary layers that are generated along the surfaces of the carrier and orbital stages. Such a boundary layer

occurring over hypersonic body has a specific behavior which is characterized by temperature increase. This is due to the higher kinetic energy of hypersonic flow dissipated by the influence of the friction within the boundary layer. This extreme viscous dissipation can create very high temperature. At higher temperature, the air viscosity coefficient increases, and this by itself will make the boundary layer thicker. Together with this, a decrease in density ρ occurs within the boundary layer, so that in order to pass the required mass flow through the boundary layer at reduced density, the boundary-layer thickness must be larger. Both of these phenomena combine to make hypersonic boundary layers grow more rapidly than at slower speeds [18]. The thick boundary layer in hypersonic flow can exert a major displacement effect on the inviscid flow outside the boundary layer causing a given body shape to appear much thicker than it really is. Due to the extreme thickness of the boundary layer, the outer inviscid flow is changed, these changes in the inviscid flow in turn feed back to affect the growth of the boundary layer [19]. This viscous interaction also has important effects on the surface distribution, hence on lift, drag, and stability on the hypersonic vehicles.

The other flow phenomena on associated with boundary layer may occur in the gap region between the stages, namely when a strong incident shock wave impinges on boundary layer at some downstream location. The large pressure rise across the shock wave acts as severe adverse pressure gradient imposed on the boundary layer, thus causing the boundary layer to locally separate from the surface. The separated boundary layer may induce a shock wave defined as the induced separation shock occurring at the head of the impingement point of the incident shock wave. Subsequently, the separated boundary layer turns back toward the body, reaching to the surface at a certain downstream location, and causing a reattachment shock. Between the separation and reattachment shocks, expansion waves are generated where the boundary layer is turning back toward the surface [18][20].

The accurate solution of the viscous problem requires an appropriate turbulent model for hypersonic flows. This last problem is not considered in the present investigation.

3. Progress in Analysis of Unsteady Stage Separation of the Hypersonic Space Transport Systems

The problems of two-stage space transport systems during separation manoeuvre have been investigated in numerous experimental and numerical studies. In 1960s, Decker and Gera have performed analysis of the aerodynamic performance and the aerodynamic interference effects of the Parallel-staged simple configurations at Mach numbers of 3 and 6 during separation [21], where the aerodynamic data obtained constitutes the input for the system of equations of dynamic motion. Then, during the Space Shuttle program in the 1970's, several measurements and calculations dealing with the separation of the liquid-fuel tank from the shuttle orbiter were accomplished [22]. In addition, the experimental studies [23][24] deal with separation of two winged stages accomplished in the mid 1990's. These results extended the knowledge on such class of complicated flows and are necessary for testing the numerical methods developed. The recent experimental measurements on the separation of two-stage space transport systems were carried out with the full configuration of the carrier and orbital stages [11][12]. These experiments provide data base of aerodynamic characteristics of separating models of the orbital and carrier stages including their interferences.

Moreover, in the period between 1985 and 1990 there was significant increase in the application of CFD for modeling hypersonic flows [25]. For example, a method for calculating aerodynamic characteristics of the first stage (fuel tank) and the orbital stage (Buran vehicle) during separation is proposed in [26]. The flow field in the vicinity of the first stage is calculated using the McCormack scheme and used to calculate the characteristics of the second stage. The other examples are the computations of several flight

situations of the ascent flight including the separation manoeuvre. These were performed using the three-dimensional Euler and three-dimensional Navier-Stokes methods [13][14][27].

However, all investigations above assume a steady flow field and, thus, neglect additional velocities induced from separation maneuver. Based on the results in [17][28] showed that the effects of unsteady flows during separation due to the shock interactions between the upper stage and lower stage are non-negligible. This indication is also supported by Cvrlje et al. who performed numerical simulation involving both roll and yaw oscillations of an orbital vehicle for different reduced frequencies [16]. Cvrlje also presented the effects of unsteady flows including laminar boundary layers on the longitudinal motions of an idealized Two-Stage Hypersonic vehicle during separation [15]. Although the phenomena of unsteady flows on the two-stages space vehicle have a significant effect on safety during separation maneuver few investigations exist for unsteady cases as presented in references [7][14][16][29]. The investigations have been accomplished for incomplete geometries and simple trajectories of the separation manoeuvre. This is due to the difficulty in generating proper meshes in physical domain around the complex geometry model. Also, the complex geometry will produce more complex flow behavior in flow field. Therefore, the investigation of unsteady flows for the complex configuration is a challenging research in order to make realistic simulation of unsteady flow of two-stage space transport systems during separation manouevre.

4. Objectives and Scope of the Study

From the above discussions, the objectives of the study is firstly to obtain numerical simulations of unsteady stage separation of two-stage space transport systems, and secondly to analyze the unsteady effects of the dynamic separation process on flow behaviours and unsteady airloads of the vehicle system.

To achieve the objectives, the scope of the present study is as follows:

1. Further development of unsteady numerical code in order to be able to solve the unsteady stage separation with the complex geometry and to obtain efficient solution by improving the quality of grids by insuring orthogonality using local smoothing technique.
2. Generating appropriate block topologies for obtaining higher quality of the initial grids.
3. Performing the grid quality improvement by using the smoothing technique to achieve the orthogonal grids.
4. Carrying out the steady flow calculations by the use of two carrier stage models, namely a flat plate for simplifying interference effects and a fully detailed vehicle (ELAC1C), each of which linked to the detailed orbital stage (EOS). The simpler configuration is used to study the effects of numerical factors on flow solution including grid density and grid smoothing. In addition, both configurations are used to validate the simulation method by comparing with experimental data.
5. Performing further analysis of the influences of “separation” parameters at steady flow condition on the flow fields and aerodynamic characteristics for the idealized and full configurations.
6. Carrying out the unsteady simulations for the full configuration and studying the effects of a downwash due to the orbital motion during the separation process on flow fields and aerodynamic characteristics of the overall vehicle system.

5. Problem Solution and Methodology

In order to perform stage separation simulations and to investigate the effects of “separation” parameters on flow behaviour and aerodynamic characteristics of the TSTO space transportation system, numerical simulations of stage separation are carried out in two ways: firstly, a stage separation is simulated in quasy-steady state flow by setting the computational model of the orbital stage at various positions relative to the carrier stage; secondy, the stage separation is simulated as truly unsteady

flow, time dependent by including the downwash effects due to the orbital motion.

The computational simulations start with the definition of computational domain by generating a block topology. The proper block topology is a good start for obtaining high quality grid and hence accurate solution. For the complex region, a multi-block technique is used to provide more accurate solution rather than the use of only single block. This requires a good understanding about the detail of the geometry of the model including the shape and location of all lifting surface components and the flow features.

After the block topology is formed, the initial (coarse) grids in the volume and surfaces of the blocks are generated by an interpolation technique called as transfinite interpolation that is based on the algebraic method.

The next step is to improve the grid quality from coarse grids becoming finer grids. This is accomplished iteratively by solving Poisson's equation [30][31]. The use of a Poisson algorithm results in smoothing the initial grid in order to achieve small cell deformation and continuous cell growth. The connection between adjacent blocks is organized by mother-child relations where the grids points located at block connection are allowed to move during the iteration process [7]. The convergence criterion for sufficient smoothness is fulfilled if the change in the residual is below 10^{-4}.

For a simulation of unsteady stage separation, further development of the solver code is performed by adding subroutine to determine the static and moving blocks. The moving grids are then smoothed locally to increase the grid orthogonalily at each time step. The local smoothing technique is performed based on Laplace's solution.

Furthermore, the computation of flow properties such as density, velocity, pressure, etc. in the computational domain requires a mathematical model as

governing equation of the flow motion. The unsteady Euler equations are considered an adequate approximate level for simulating unsteady stage separation of the space vehicle. This is based on wind tunnel experiments [11][12] that the boundary layer at Reynolds number of 50×10^6 is very thin and hence, viscous effects can be neglected. The flow governing equations are then discritized using a numerical technique based on the method of lines, namely a separate discretization in space and in time [32][33]. The spatial discretization for the equations is carried out using finite volume method. The surface integral is approximated by the sum of fluxes crossing individual faces of the control volumes.

The evaluation of shock waves occurred in many regions especially in the region between the stages is carried out by a numerical scheme based on shock capturing approach. The principle of the shock capturing approach is to allow shock waves to form within the computational domain as a consequence of general flow-field algorithm, without any special shock relations being introduced [25][34]. This approach is suitable for complex flow problems involving shock waves for which we do not know either the locations or number of shocks. This approach will smear shock wave over a number of grid points in the computational mesh. The drawback can be overcome by applying an upwind flux splitting scheme. One of the advanced upwind schemes which is able to obtain efficient solutions is the modified AUSM scheme (Advection Upstream Splitting Method) proposed by Liou [35][36].

Furthermore, a time marching technique based on the explicit Runge-Kutta intergration method is used [37]. Applying boundary conditions real solutions will be achieved. However, the final solutions are just obtained after the iterative computation reaching the given convergence criteria or steady state condition.

For unsteady flow field calculations, a dual time-stepping methodology proposed by Jameson is used [38]. This method employs a pseudo-time to redefine the unsteady flow problem into a steady flow problem, with the physical time derivative included in the discretized equations. Unsteady solutions are carried out for the number of time steps per cycle. The solution of each time step depends on the position of the orbital stage. The orbital stage motion is approached using harmonical motions simultaneously in the orbital stage angle of attack and separation distance stated in one-minus-cosinus function. The unsteady flow calculation requires the steady flow solution as an initial input.

6. Outline of the Present Analysis

The dissertation is organized as follows: Chapter II describes the computational aerodynamic simulation, computational approach to physics of stage separation of two-stage transportation system, the mathematical models, physical models of two-stage transportation system and the model of separation manouevre path. The definitions of aerodynamic forces and moment are also presented.

Chapter III presents grids in computational fluid simulation, the grid methods for stage separation of TSTO space transportation systems including multi-grid method, structured grid generation and elliptic grid smoothing techniques. The dynamic grid technique for TSTO Space vehicle system is presented at the end of this section.

Chapter IV describes the numerical methods for solving Euler equations. Numerical techniques for stage separation of the TSTO space transportation system are discussed including finite volume discretization method, convective flux discretization, temporal integration, the applied boundary conditions and unsteady simulation technique.

In Chapter V the steady aerodynamic of stage separation analysis for two TSTO configurations, namely the EOS - flat plate and EOS - ELAC1C are accomplished. Firstly, the test models and conditions for experiment and computation are described then followed by the discussions of the computational procedures. The effects of grid smoothing and grid density on the computational efficiency and accuracy are investigated. The validation of the computation results with the corresponding experimental data for both the configurations is performed. In addition, the detail analysis related to the effects of separation parameters ends this chapter.

Chapter VI presents the unsteady stage separation analysis of the fully two-stage space transport system. The procedures and results of the unsteady simulations are discussed. The influences of “separation” parameters on the flow field and aerodynamic characteristics of both the stages are discussed. The comparison between the steady and unsteady are elaborated.

Chapter VII contains the conclusions and recommendations for further studies.

7. Research Contributions

1. Solving the simulation problem of stage separation aerodynamics of two-stage space trasport system which involves complex computational domains due to the complex geometry of the vehicle system and time-dependent flow due to the influence of the orbital motion during separation manoeuvre. The complexity of the space vehicle geometry has been described in the section 2. Because the orbital stage (EOS) is move up relatively to the carrier stage (ELAC1C), the computational domain at which both stages located can not be considered only as a single moving domain, so that a procedure of computational domain division is required. In this research, the computational domain division is proposed by separating the domain into stationary domain around the carrier stage (ELAC1C) and moving domain around orbital stage (EOS).

The way how to build block topology plays an important rule in a part of the success in solving of the simulation problem. This is necessary to carry out in the beginning of the topology definition by using O-grid topology tool in ICEMCFD.

2. Further development code based on locally smoothing grid technique is carried out for unsteady flow simulation. It is noted that during the orbital movement from one to another physical time, the grids in the moving domain always changes. The change of the grid points on internal block boundary and inside the moving blocks must be handled in order to obtain the high grid quality (grid orthogonal). This is firstly done by adjusting and distorting with the movement orbital stage and the fixed outer boundary according to the movement rule. Secondly, the resulted grids are then smoothed locally at each block by solving the Laplace's equation iteratively until the maximum grid error less than 10^{-4} .

3. The approximate rule of the harmonic motion, namely one-minus–cosinus fuction is proposed in the research in order to approximate the real orbital trajectory during separation manoeuvre. In addition, the simultaneous motion in distance and agle of attack of the orbital stage is also introduced. For this purpose, some subroutines in the numerical program are necessary to modify by considering a simultaneous alteration in translation (distance) and rotation (angle of attack). The movement rule is only applied on the moving domain by specifying the corresponding blocks. In addition, the code is also added to have the capability to compute an arbitrary simultaneously harmonic motion.

4. After having investigated the numerical methods for unsteady flow equations in the FLM numerical program and performed a literature study of some corresponding previous works [7][17][39][72], my decision is to elaborate the existing numerical methods, namely the

upwind method based on the modified AUSM for the flux evaluation and the dual time-stepping method for time integration used for solving the complex problem of stage separation of the space vehicle system which involves many time-dependent aerodynamic interferences.

CHAPTER II
COMPUTATIONAL AERODYNAMIC SIMULATION

1 Simulation of Stage Separation of TSTO Space Transportation Systems

As mentioned in the previous chapter, in order to perform a safe flight mission of two-stage space transportation systems including stage separation, it is essential to evaluate the whole system components such as structural materials, propulsion, thermal protection systems as well as aerodynamic performances and stability of the vehicle. This is usually done by testing them in the ground using either experimental simulations or computational simulations at the time of design phase. These simulations are to provide a set of database for analyzing behaviors and characteristics of the systems, so that their performances are well-known and system failures during the flight can be anticipated. Generally, simulations are carried out by simplifying complex real physics of the systems into scaled models with taking some approximation levels such as a physical scale, spatial as well as dynamic. In addition, simulations may include the identification of important parameters which have great influences on the system, the formulation of interaction rules between variables of the systems, and the construction of physical or mathematical models as well as the development of experimental or numerical procedures.

In particular, for the computational aerodynamic simulations of two-stage space transportation systems, both physical and numerical are required to obtain efficient numerical solutions. The physics deals with the geometric configuration and flow features. Moreover, the numerics considers a determination of the optimum way to predict airflows of high interest. The structure of computational aerodynamic simulation is shown in Fig. II.1, [32]. The detail description of the computational aerodynamic simulations relating to the physics and numerics for unsteady stage separation of the space vehicle will be given in the present and two following chapters.

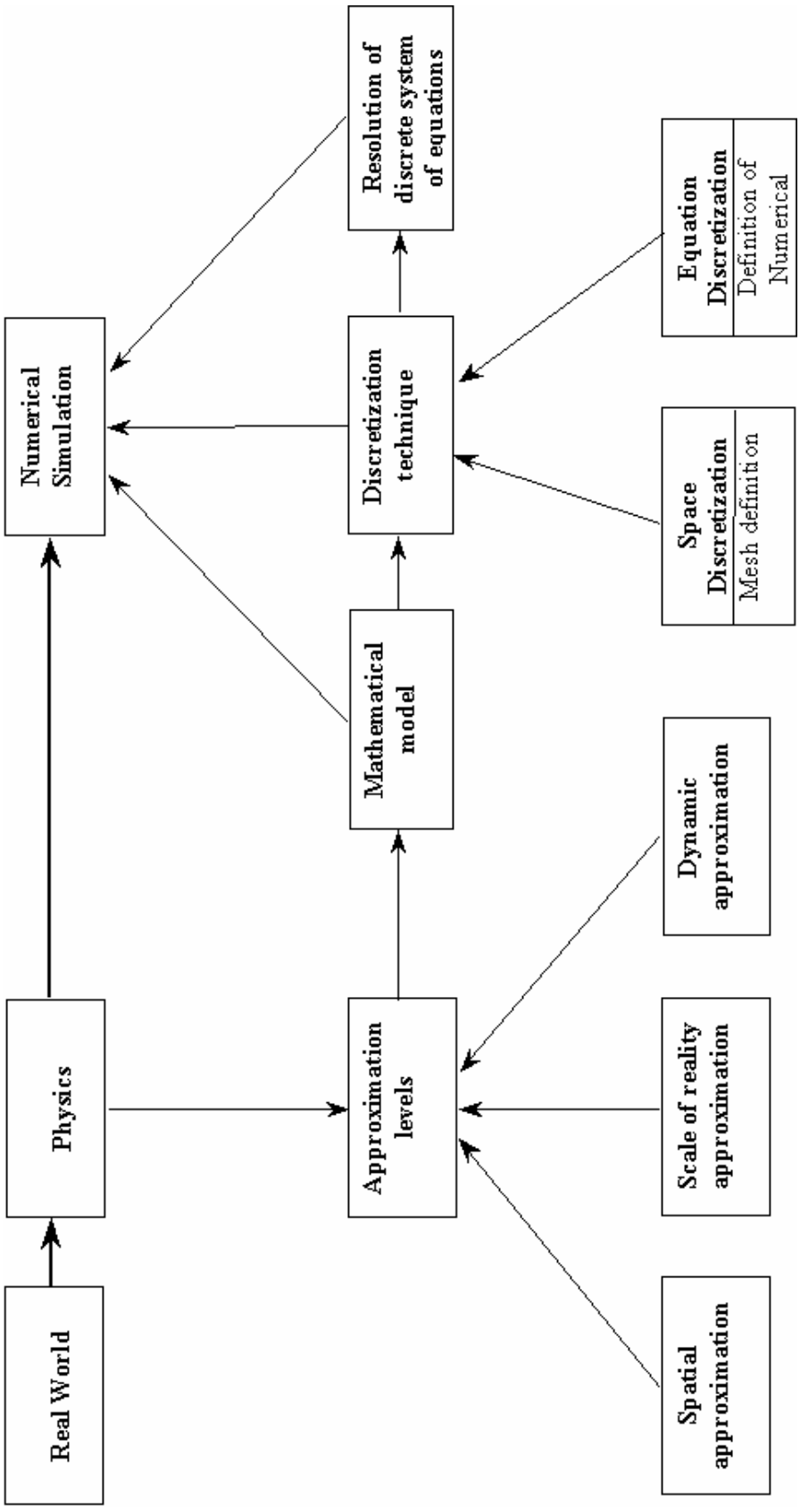

Figure II.1: Structure of computational aerodynamic simulations [Ref. 32]

2 Computational Approach to Physics of Stage Separation of the TSTO Space Vehicle System

Physics of stage separation of the TSTO space transportation systems is very complex. The complexity of the stage separation process is due to the present of the TSTO configuration consisting of two vehicles simultaneously arranged as the upper and lower stages, and aerodynamic interferences between the stages, namely the complex interactions of the incident and reflected shock waves and expansion waves with each other as well as with boundary layers. In addition, by increasing the gap area between both stages, the orbital stage produces a downwash which influences the position and intensity of the shock waves as well as the points of inflection of the reflected shock waves. Thus, to obtain numerical simulations of the stage separation of the TSTO space transport system, appropriate definitions of the geometry of the model, physical flow model and the model of the stage separation path of the orbital stage are required.

The model of the geometry of the space transport system should be defined as closed as possible to the real geometry of the vehicle. However, due to the limitations of the computation technology and the computation time and cost, the use of less complex geometry models are preferred to obtain reasonable numerical solutions at the beginning of the simulations. They may be obtained by simplifying a part of or the entire component surfaces of the TSTO vehicle system. At the beginning of the computational evaluation of the aerodynamics of the stage separation of the vehicle system, for example, the effects of the engines of both stages may not be taken into account, so that the air breathing propulsion on the lower surface of the carrier stage can be simplified as a ramp surface and rockets at the base of the orbital stage may be eliminated.

Furthermore, in addition to the geometry of the model, the accuracy of the numerical solutions depends on the description of physical flow model which stated in mathematical models. The mathematical models can be

derived from the real flow system by introducing the approximation levels as shown in Fig. II.1. For analyzing aerodynamics of the space transport system which flies at the very high altitude, the proper mathematical flow model may be obtained with considering the “physical scale” approximation, namely whether the flow problem will be solved based on a microscopic point of view (molecular approach) or on a macroscopic approach. The first approach is suitable for the case of a reentry space vehicle moving in very rarefied atmosphere at an altitude above 92 km. At this condition the air density is low enough that only a few molecules impact the vehicle surface per unit time, and after these molecules reflect from the surface, they do not interact with the incoming molecules [18]. In this case, continuum assumptions are no longer valid, and the mathematical models are derived from kinetic theory. Whereas, the problem of the stage separation of the space transport system taking place at altitude of 35 km is more appropriate by using the second approach because the flow particles around the vehicle can be considered as a continuum [7]. For continuum flows, flow mathematical models can be determined based on the dynamic approximation which estimates the influences of the relative forces and their components on the flow behaviors such viscous, elastic and inertial forces. Using fundamental principles in mechanics, namely mass and energy and the fluid motion satisfy Newton’s second law and applying it to the fluid flow, the mathematical flow models in the various approximation levels can be derived as shown in Fig. II.2. The full Navier-Stokes flow model describes unsteady viscous compressible flows. One can obtain very accurate flow solutions using this flow model, but in their applications, this remains for the limited geometry models and requires much computational time. At the present time, the problem of stage separation of the TSTO space transport system may be solved by using the solution of Reynolds Averaged Navier-Stokes (RANS) with introducing a turbulence model, or the solution of Euler equations when viscous effects can be neglected.

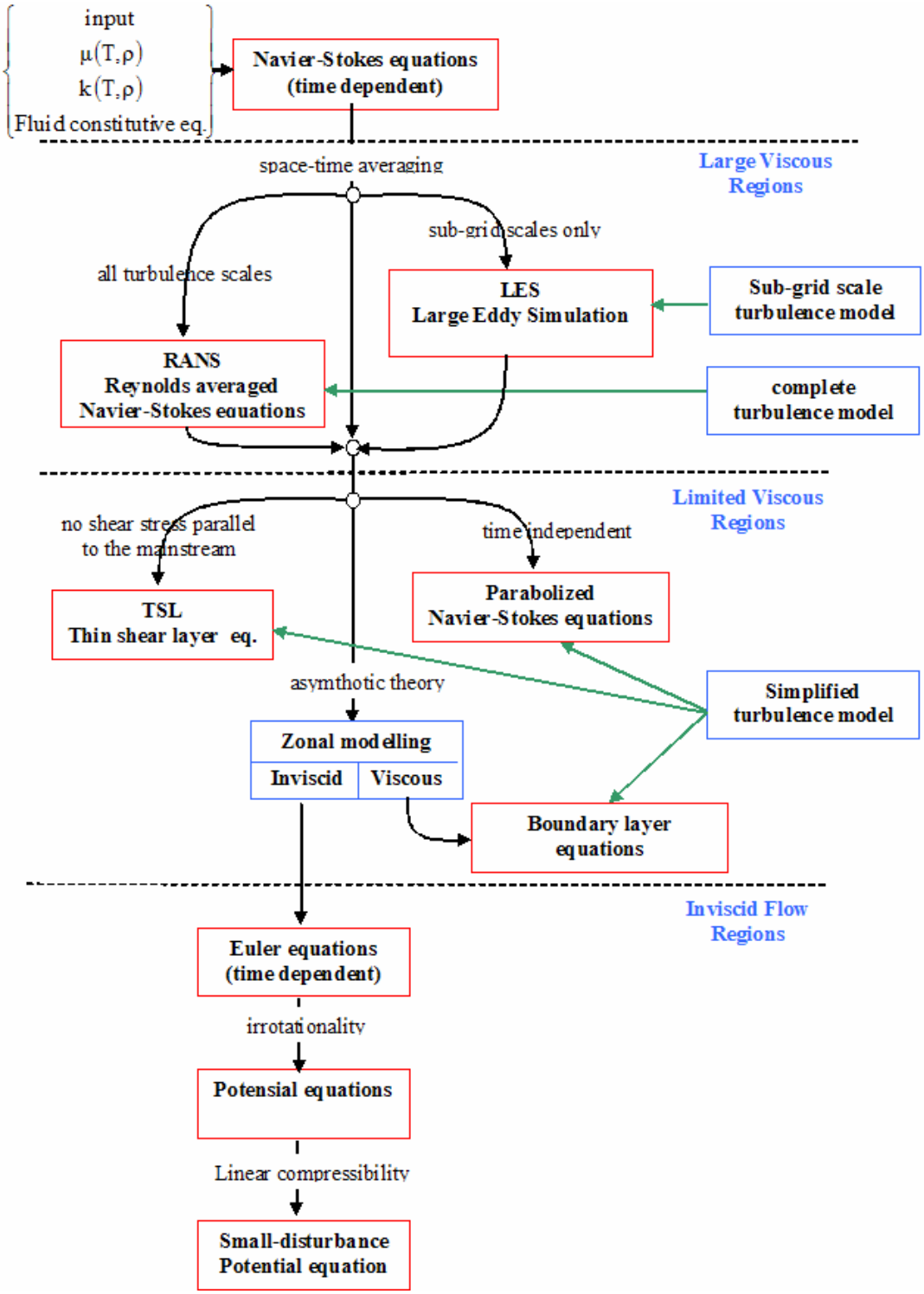

Figure II.2: Flow approximation levels

3 Basic Mathematical Flow Models

By considering the approximation levels discussed in the previous section led to select the appropriate mathematical models for solving the problem of unsteady hypersonic flow. Based on the wind tunnel experiments [11][12], the two-stage space vehicle was tested at Mach number of 4.04 with the unit Reynolds number of about 50.0 x 10^6. Under this condition, the boundary layer thickness for a flat plate surface is very thin, $\delta/x = 0.017$. Only small effects of viscous may occur on the vehicle system. The whole flow field can be assumed as inviscid flow and solved by Euler equations with neglecting the viscous effects.

3.1 The unsteady Euler equations

The unsteady Euler equations consist of two scalar equations and one vector equation. The first scalar equation expresses conservation of mass for the fluid flow. The second scalar equation expresses conservation of energy stated by the first law of thermodynamic. The vector equation expresses conservation of momentum and is obtained by applying Newtow's second law to a moving finite control volume. In compact form, the Euler equations in a moving finite control volume Ω with S as the boundary can be written as [39]

$$\frac{\partial}{\partial t}\iiint_{\Omega} \mathbf{q}\, d\Omega + \iint_{S}\left[\mathbf{f}\cdot n_x + \mathbf{g}\cdot n_y + \mathbf{h}\cdot n_z\right] dS = 0 \qquad \text{(II.1)}$$

where **q** is the vector of conservative variables, **f**, **g** and **h** are the convective terms in the vector component of x, y, and z, respectively. The vector of conservative variables is:

$$\mathbf{q} = \begin{bmatrix} \rho \\ \rho u \\ \rho v \\ \rho w \\ e \end{bmatrix} \qquad \text{(II.2)}$$

while the convective fluxes are:

$$\mathbf{f}=\begin{bmatrix}\rho u\\ \rho u^2+p\\ \rho uv\\ \rho uw\\ (e+p)u\end{bmatrix}\quad \mathbf{g}=\begin{bmatrix}\rho v\\ \rho vu\\ \rho v^2+p\\ \rho vw\\ (e+p)v\end{bmatrix}\qquad \mathbf{h}=\begin{bmatrix}\rho w\\ \rho wu\\ \rho wv\\ \rho w^2+p\\ (e+p)w\end{bmatrix} \tag{II.3}$$

The system of the equations still needs supplementary relationships as there are now more variables, i.e. ρ, u, v, w, e and p, than the number of the equations, i.e. five. For a gas of a fixed composition the thermodynamic state principle states that the complete thermodynamic state is determined by two variables. The other thermodynamic variables then follow from so-called equation of state. For air at normal temperature and pressure, the perfect gas relation defines a relation between the thermodynamic properties of the flow as given by the following thermal equation of state

$$p=\rho \mathbf{R}T \tag{II.4}$$

where T is the absolute temperature and R is the gas constant. In the international unit system, R=287 J/kgK. For a callorically perfect gas the internal energy and enthalpy are unique functions of temperature, i.e.:

$$e=c_v T \tag{II.5}$$

$$h=c_p T \tag{II.6}$$

where h is the enthalpy, c_v and c_p are the specific heat at constant volume and the specific heat at constant pressure, respectively. Both c_v and c_p are constant and thus internal energy and enthalpy are linear functions of temperature. Using these relations, the pressure is obtained as:

$$p=(\gamma-1)\rho e \tag{II.7}$$

where $\gamma=c_p/c_v$ is the ratio of the specific heats.

The Euler equations have two important mathematical properties, namely hyperbolic character of the unsteady Euler equations and the existence of discontinuities allowed in the solution, i.e. shock waves, vortex sheets and contact discontinuity surfaces. The first property of the unsteady Euler equations is hyperbolic with respect to time. They are demonstrated by the existence of wave-like solutions in the form of [40][41]:

$$\mathbf{q}\left(x,t\right)=\hat{\mathbf{q}}\,e^{i\left(n\cdot x-\omega t\right)} \tag{II.8}$$

where $i=\sqrt{-1}$, x is the position vector and n is a normal to the wave front surface (surface which separates the region which has been and the one which has not been influenced by the wave). Morreti and Abbett [42] show that the utilization of a time-marching approach on the unsteady Euler equations is a properly posed mathematical problem in all regions of the flow, and allows the solution of both subsonic and supersonic regions simultaneously without using two different numerical techniques. The second property of the unsteady Euler equations is contrary to the Navier-Stokes equations where in principle the density, pressure and velocity fields are continuous due to the presence of elliptic viscosity and heat conduction terms. The numerical methods to solve the system of Euler equations are based on these mathematical properties.

The Euler equations in Eq. (II.1) can be written in the form of conservative differential either in Cartesian coordinate system x, y, z :

$$\frac{\partial\mathbf{q}}{\partial t}+\frac{\partial\mathbf{f}}{\partial x}+\frac{\partial\mathbf{g}}{\partial y}+\frac{\partial\mathbf{h}}{\partial z}=0\ , \tag{II.9}$$

or in Curvilinear coordinate system as follows

$$\frac{\partial\mathbf{Q}}{\partial\tau}+\frac{\partial\mathbf{F}}{\partial\xi}+\frac{\partial\mathbf{G}}{\partial\eta}+\frac{\partial\mathbf{H}}{\partial\zeta}=0 \tag{II.10}$$

The derivations of Euler equations in Eqs. (II.9) and (II.10) can be seen in Appendix A. The mathematical model for the unsteady Euler equations with moving grid is given in Appendix B.

4 Geometry Models of TSTO Space Transportation System

As shown in Fig. I.1, the space transportation system consists of two stages, namely carrier stage and orbital stage. In this study, the simulations of stage separation of the vehicle system are carried out using two carrier stage models, i.e. a flat plate used as the preliminary study and a fully detailed vehicle (ELAC1C). In both cases, the orbital stage consists of a detailed configuration (EOS). The geometry layouts for the EOS – flat plate model and the EOS - ELAC1C model are depicted in Figs. II.3 and II.4, respectively.

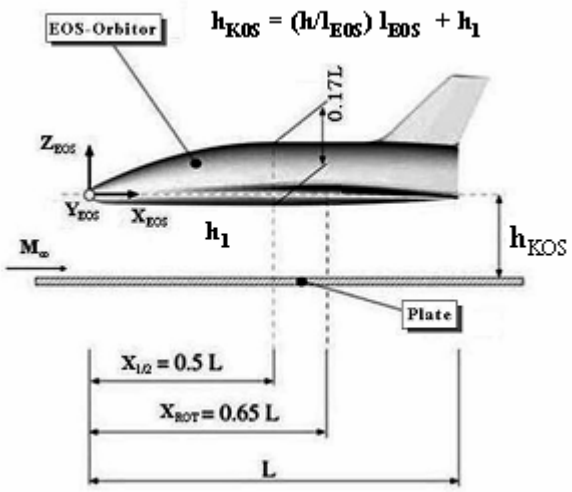

Figure II.3: Basic geometry of EOS and flat plate [Ref. 43]

Concerning the flat plate, it is a simplified model of the carrier stage with a flat surface. The parameter h_{KOS} refers to the distance from axis X_{EOS} to the flat plate; L is the body length of EOS.

For the full TSTO space transportation system, the carrier stage was designed as a slender blended wing-body shape with the fixed swept winglets. It has a large cavity located in the middle part of the upper side of

the carrier stage to place the orbital stage. In addition, the present of the air breathing propulsion on the lower side of ELAC1C is modeled as a ramp surface. While, the orbital body was designed a nearly circular cross section equipped with a delta wing and vertical stabilizer.

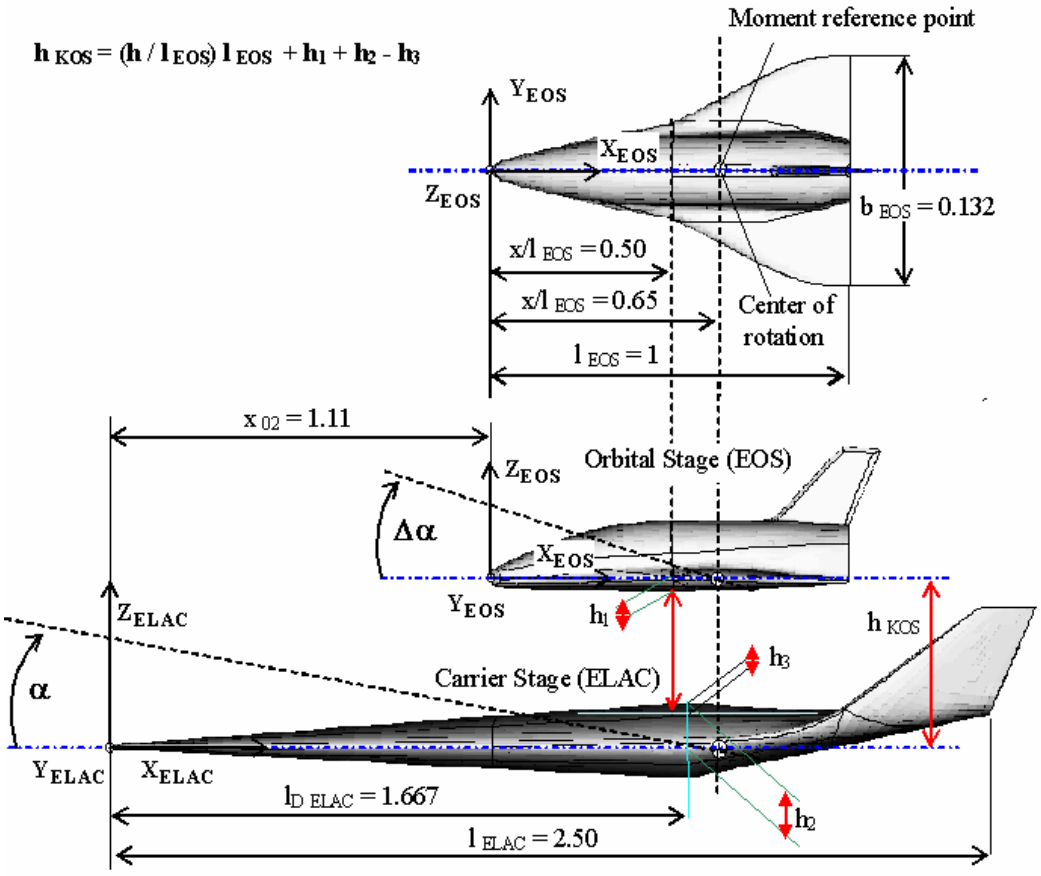

Figure II.4: Configuration and geometric reference values of the EOS-ELAC1C two-stage transportation system.

The distance $\mathbf{h}_{KOS}$ is between the axes $\mathbf{X}_{ELAC}$ and $\mathbf{X}_{EOS}$ of the stages. The parameter $\mathbf{h}_{KOS}$ of each model is measured with a mathematical relation stated in each figure. The parameter of the relative distance is given by h/l_{EOS}. The angle of attack (α) is measured based on the X-axis of the ELAC1C model, and the relative angle of attack ($\Delta\alpha$) of the EOS model is calculated based on the X-axis of the flat plate or the ELAC1C model.

5 The model of Separation Path of the Orbital Stage

The separation path of the orbital stage is taken from the flight mechanic analysis data for the TSTO space transport system as shown in Fig. II.5 [44]. The separation process takes place with the orbital stage relatively moving simultaneously in the separation distance and orbital stage angle of attack. The graphs of the relative angle of attack ($\Delta\alpha$) and relative distance (h/L_{EOS}) against time are shown in Fig. II.6 (a and b), respectively.

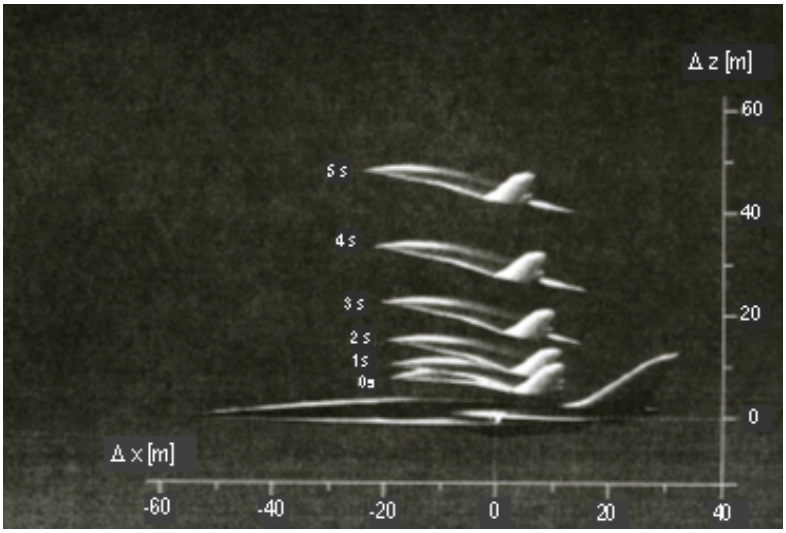

Figure II.5: The trajectory of stage separation of TSTO space vehicle system [Ref. 44]

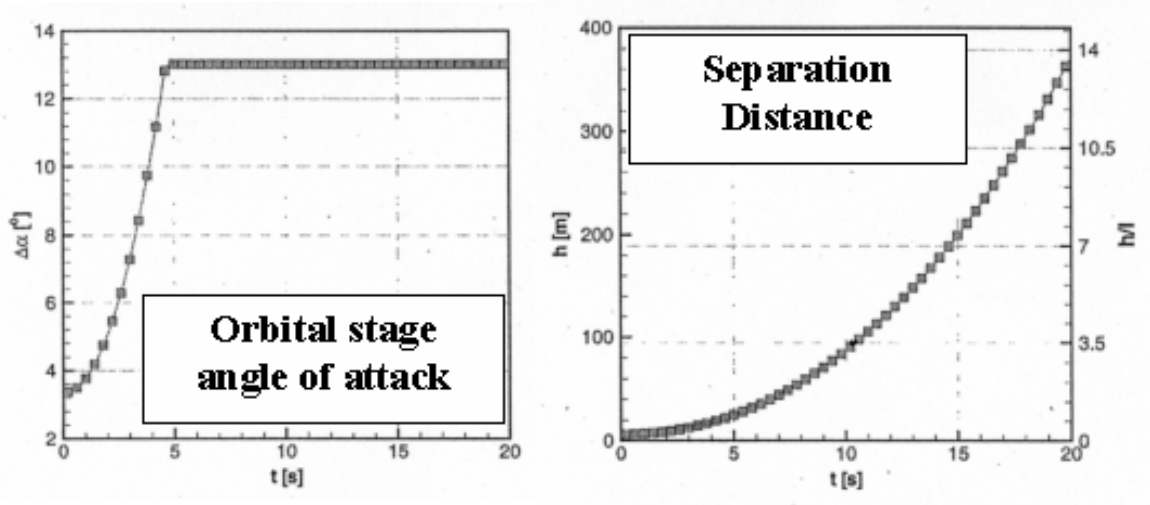

Figure II.6: The parameters of stage separation of the TSTO space vehicle system [Ref. 45]

In order to perform the computational simulations of the stage separation, the staging path is approached with a harmonic function, namely one-minus-cosines function that applied for the relative angle of attack and relative distance as follows

$$\Delta\alpha(\tau) = \Delta\alpha_0 + \frac{(\Delta\alpha_1 - \Delta\alpha_0)}{2}\left(1 - \cos(k\tau)\right) \tag{II.11}$$

$$h(\tau) = h_0 + \frac{(h_1 - h_0)}{2}\left(1 - \cos(k\tau)\right) \tag{II.12}$$

where α_0, h_0, α_1 and h_1 are constants of the orbital stage angle of attack and separation distance at the initial position and the end position of the separation process, respectively. The τ is time step that the amplitude of the orbital stage changes at every time step. The smaller time step the more step number is required to the complete solution, hence it requires more computational time. The reduced frequency, k constitutes a number expressing a ratio of the angular velocity to the free-stream velocity. Increasing the reduced frequency provides the higher angular velocity, hence a downwash due to the orbital stage motion becomes greater. The non-dimensional time step size, τ and reduced frequency, k for unsteady flow are written as [15][46]:

$$\tau = \frac{V_\infty}{l_{ref}} t \qquad \text{and} \qquad k = \frac{l_{ref}}{V_\infty}\omega \tag{II.13}$$

Referring to free-stream condition with $V_\infty = M_\infty\sqrt{\gamma}\sqrt{\frac{p_\infty}{\rho_\infty}}$, the equation (II.13) is written :

$$\tau = \frac{M_\infty\sqrt{\gamma}}{l_{ref}}\sqrt{\frac{p_\infty}{\rho_\infty}}\, t \qquad \text{and} \qquad k = \frac{l_{ref}}{M_\infty\sqrt{\gamma}}\sqrt{\frac{\rho_\infty}{p_\infty}}\,\omega \tag{II.14}$$

6 Aerodynamic Force and Moments

The motion of air around the vehicle system in the atmosphere produces pressure and velocity variations which yield aerodynamic forces and moments. Figure II.7 shows the force and moment components acting on the aerodynamic center of the space vehicle. In three dimensional flows, the force components can be defined either using a aerodynamic reference system, as lift, drag, and side force, or using a body reference system as normal, axial and side forces.

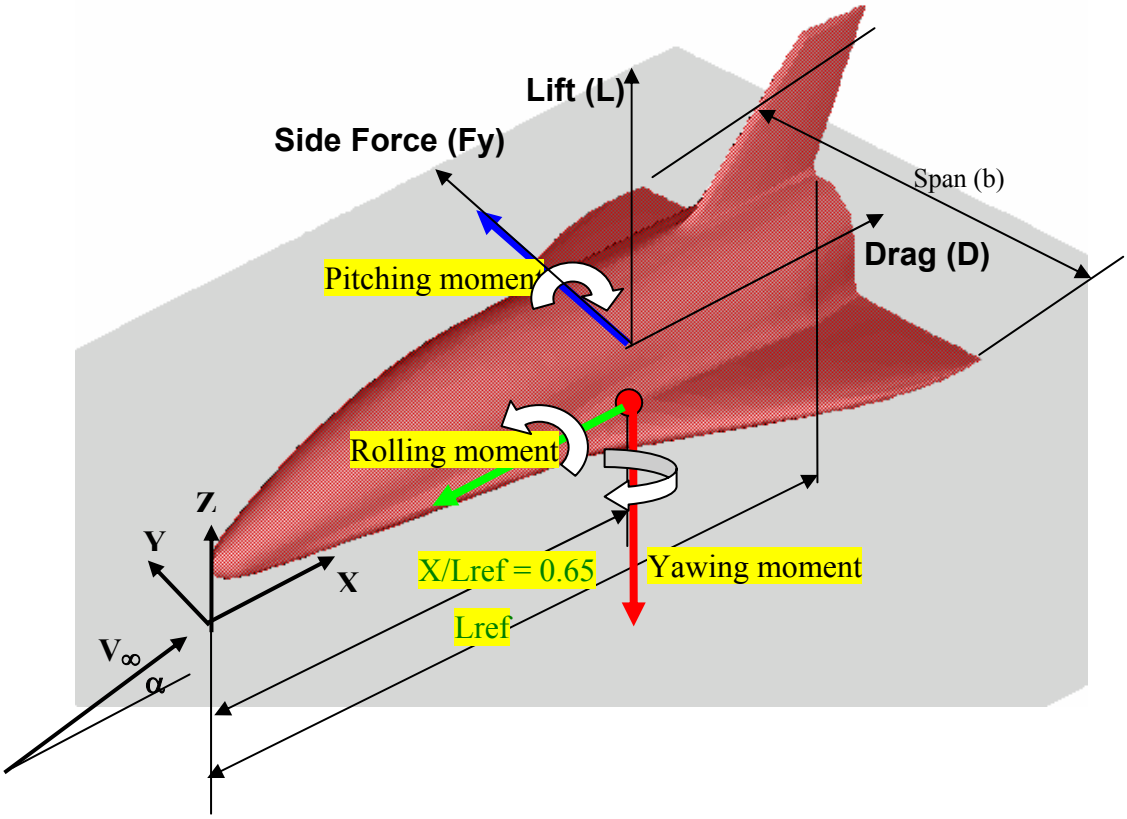

Figure II.7: the force and moment components acting on the space vehicle

In order to calculate the aerodynamic force and moment coefficients from wind tunnel experiment or numerical computation, it is necessary to divide the measured or calculated forces by a given free-stream dynamic pressure and reference area, and the measured or calculated moments by a given free-

stream dynamic pressure, reference area and length. The aerodynamic force and moment coefficients are expressed as follows [47].

- Drag coefficient : $C_D = \dfrac{D}{q_\infty * S_{ref}}$ (II.15)
- Lift coefficient : $C_L = \dfrac{L}{q_\infty * S_{ref}}$ (II.16)
- Pitching moment coefficient : $C_m = \dfrac{M}{q_\infty * S_{ref} * l_\mu}$ (II.17)

q_∞ is the free-stream dynamic pressure, $q_\infty = \dfrac{\rho_\infty V_\infty}{2}$ (II.18)

and S_{ref} is the reference area and l_μ is the mean aerodynamic chord.

When the output aerodynamic data are extracted from the numerical computation, they refer to the body fixed co-ordinate system. In order to calculate the aerodynamic coefficients based on the wind reference system, a transformation from the body fixed co-ordinate system to the wind co-ordinate system is required. The relationship between the two sets of the co-ordinate systems with a given angle of attack, α, is given as follows; with the C_X as the longitudinal force coefficient and C_Z as the normal force coefficient of the body fixed system:

$$C_D = C_X * \cos(\alpha) + C_Z * \sin(\alpha) \quad \text{(II.19)}$$

$$C_L = -C_X * \sin(\alpha) + C_Z * \cos(\alpha) \quad \text{(II.20)}$$

CHAPTER III
COMPUTATIONAL GRID

1 Grids in Computational Fluid Simulations

In computation fluid dynamics (CFD), grids in the computational flow domains play an important role in calculating flow properties. Error in the alignment of grid points in computational domain can lead to an inaccuracy of the numerical solution and apparent instability or lack convergence as well as an increase of the computation cost and time. Thus, the generation of proper grid distributions in the computational domains constitutes a great task in the numerical simulation.

In order to generate the proper grids, some important considerations including the model geometry and the prevailing flow phenomena as well as the computation time and cost should be taken into account. Concerning the geometry of the model, the generated grid nodes must adequately approximate the original geometry that is the distance between one grid node to the nearest grid nodes is not be too large, expecially for the grid nodes at the higher curvature of the geometry of the model. However, the complexity of the model geometry of the TSTO space transportation system will require the great number of grids that cause large computational time and cost. On the contrary, the lack of the grid number will affect on the accuracies of the computation and interpolation of the solution over the whole region. Furthermore, related to the flow phenomena, capturing flows with rapid changes in the flow properties such as shock waves and boundary layers requires the greater number of the grid nodes, so that the computational time and cost increase, too. This leads to the need to carry out further development of grid generation to obtain the efficient simulation of the stage separation of the TSTO space transportation system.

2. Grid Generation Methods for Stage Separation of TSTO Space Systems

Before the grid nodes are generated in the computational domain around the geometry of the model, the kind of topologies for the grids must be defined namely, whether one block grid topology or many block grid topologies will be used. This leads to the selection of appropriate methodology for generating the grids.

For the complex geometry such as the TSTO space transportation system, one may use adequately single block topology to cover all flow fields including the solid body of the vehicles by applying unstructured grids [48]. However, the unstructured grids require a more complicated numerical algorithm than the structured grids because of an inherent data management problem. In addition, the extra memory is needed to store the information about the connections between the cells of the grids. Furthermore, the application of unstructured grids for moving boundaries or moving internal surfaces of the physical complex domains is difficult.

The other possiblity to generate the grids for the complex geometry is the use of multi-block topologies [49]. The underlying idea of the use of many block topologies is to reduce geometrically the complex region into several smaller, more manageable regions or blocks. Each block is represented mathematically by a number of discrete grid points, ordered in a three dimensional array of the constant dimensions. There are three methods based on this concept, namely overset (chimera), multi-block and hybrid. Using the overset (chimera) method blocks are allowed to overlap which significantly simplifies the block problems. In fact, each block may be a subdomain which is associated only with a single geometry or physical features. In this method, the data between the blocks are communicated using an interpolation in overlapped areas of the blocks. This method may face a problem to handle the non-linear flow behaviour in the overlapped area of the blocks which a cell to cell on the block sometimes does not match. In order to eliminate the complex interpolations between the blocks

and to circumvent the flow field conservation problem across the boundaries the requirement of the cell to cell matching has to be fulfilled. The multi-block method met this requirement because it does not require that one wall of a given block must match exactly with a wall of another block, but only that each cell on an interface wall match with a cell of an interface wall somewhere in the grid system as shown in Fig. III.1. So that, on the same block faces, it is possible to define different boundary conditions through segmentation [50][51]. This provides indeed some advantages in terms of the overall reduction of the block number. The segmentation also provides means to reduce the memory needed to store the information concerning the block relationship, as well as the computing time for the evaluation of the governing equations.

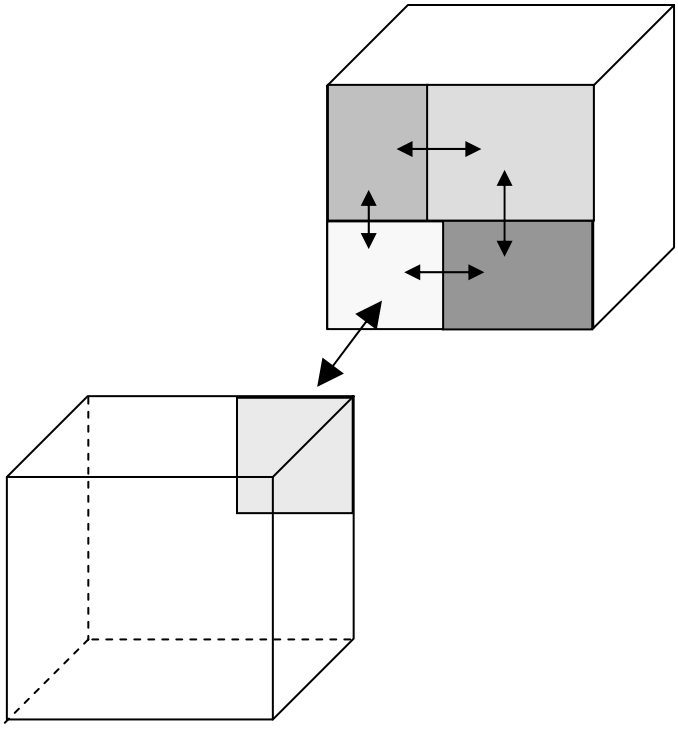

Figure III.1: Block segmentation

Furthermore, in order to estimate completely the domain block limit, it is necessary to know additional information on the significant mesh points, which represent in fact the closest layer mesh point situated within the

neighbour block. This concept is even extended with the concept of ghost/ dummy cells that contain the necessary information to define the relations between the blocks or the proximity of a physical boundary. Figure III.2 shows the schematic connection between two blocks.

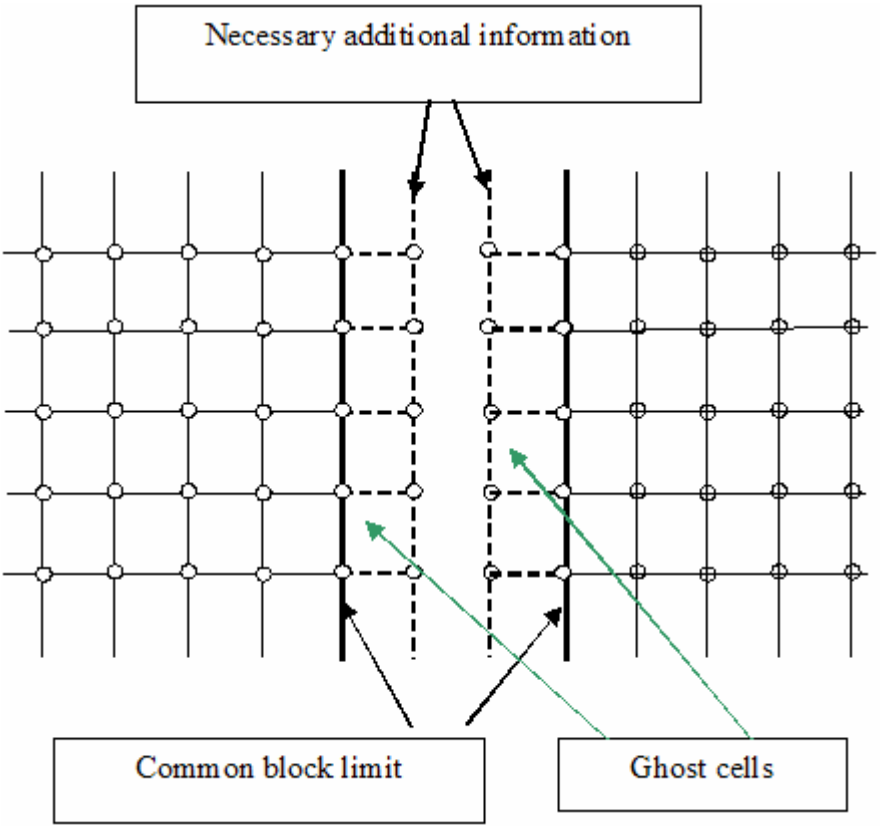

Figure III.2: Schematic block connection

2.1 Structured Grid Generation Techniques

After having defined the blocks over all computational domains, further step is to generate the grids on the faces and inside the volume of each block. There are two approaches that usually use to generarate the structured grids, namely algebraic and partial differential equation methods [52]. The algebraic grid method is usually used for generating the basic structured grids. While, the improvement of the quality of the basic grids is performed by using the grid generation based on the solution of elliptic equation such as Poisson and Laplace equations.

The basic grid generation on the faces and inside the volume of the blocks is performed by interpolating grid points on the boundary curves of the blocks. Transfinite interpolation (TFI) technique proposed by Errickson [53] is the fast interpolation technique used in this study for generating the structured grids. This technique also considers the corner points of the boundary curves to obtain more accurate grids. The expression for a TFI grid with linear interpolation function is

$$\begin{aligned}\mathbf{X}(\xi_I,\eta_J,\zeta_K) = \mathbf{U}(\xi_I,\eta_J,\zeta_K) + \mathbf{V}(\xi_I,\eta_J,\zeta_K) + \mathbf{W}(\xi_I,\eta_J,\zeta_K) - \mathbf{UW}(\xi_I,\eta_J,\zeta_K) \\ - \mathbf{UV}(\xi_I,\eta_J,\zeta_K) - \mathbf{VW}(\xi_I,\eta_J,\zeta_K) + \mathbf{UVW}(\xi_I,\eta_J,\zeta_K)\end{aligned} \tag{III.1}$$

where **X** is the position vector giving the values of the x, y, z Cartesian coordinates of a grid point. **U**, **V** and **W** are the univariate interpolation functions and tensor products. The detail description of the Transfinite interpolation technique for the structured grid generation is given in Appendix C.

The improvement of the grid point distribution and the orthogonality properties of the grids for the steady and unsteady calculations is performed by the elliptic grid smoothing process, namely by iteratively solving the Laplace and Poisson equations [7][30]. The three dimensional representation of the Poisson's equation can be written:

$$g^{11}\left(\mathbf{r}_{\xi\xi} + \mathbf{P}\,r_{\xi}\right) + g^{22}\left(\mathbf{r}_{\eta\eta} + \mathbf{Q}\mathbf{r}_{\eta}\right) + g^{33}\left(\mathbf{r}_{\zeta\zeta} + \mathbf{R}\,\mathbf{r}_{\zeta}\right) = 0 \tag{III.2}$$

with **r** is the vector of the physical coordinates that defined as $[x, y, z]^T$, ξ, η, ς curvilinear coordinates, and g^{ij} as the contravariant metric coefficients with superscripts i, j =1,2,3. The **P**, **Q**, **R** are the source terms of

Poisson equation. Detail description of Poison and Laplace equation is given in appendix D or in Ref. [7].

During the grid smoothing process, connections between the adjacent blocks are organized by mother-child relations where the grid points located at the block connection are allowed to move [7]. The source terms are determined at the solid body by inverting the Poisson equation. The mirror points with a fixed distance from the solid body wall are employed to calculate the derivatives at the block boundaries. The Laplace equation is used to spread the source terms into the computation domain. The convergence criterion for sufficient smoothness is fulfilled if the change in the source strength does not exceed 10^{-4}. The elliptic smoothing is applied for each block. The mechanism described presents a stable and flexible tool avoiding cell singularities or overlaps. The distribution of the mesh points is performed to represent adequtely the geometry shape of the body and to concentrate them in regimes with high gradients of flow variables.

2.2 Dynamic Grid Technique for TSTO Space Vehicle System

In order to carry out unsteady calculations which involving a moving solid surface, a dynamic adaption of mesh to the actual body position must be performed for each time step in the computational domain. Concerning this, there are two methods for defining the moving grids [7]. The first possibility exists in the so-called rigid body movement. With this method the model together with the whole computational domain moves in the way of the prescribed movement. Such a movement causes the farfield boundaries changed with the speed resulting from the movement. The advantages of this method are the simple treatment of the computational grid, and the grid structure remains unchanged during the entire calculation. However, this method can not be implemented for the computational domain containing both the dynamic grids and stationary grids, such as the case of unsteady stage separation of the two-stage space transportation system as shown in Fig. III.3.

The second method, which is used in the present study, is the use of the deformation of the computational grid. In contrast to the rigid body movement, this method assumes that the edges of the outer boundaries remains unchanged, and only the configuration itself is moved. According to that the grid must be adjusted and distorted by the movement of the solid body and the fixed outer boundaries. Moreover it must be guaranteed that during this deformation the quality of the computational grid remains good. This can be carried out by locally smoothing the mesh by solving the Laplace equations.

For the simulation of the stage separation of the TSTO space transportation vehicle, the computational domain for the moving grids is limited in given regions around the EOS model that was generated with the O-grid topology as shown in Fig. III.3. The inner boundary of the mesh at which the solid surface resides has to conform to the motion of the EOS surface at all times. The mesh outer boundary of the O-grid is free to move or is fixed. The velocity of the mesh as well as the deformation of the cells is considered in the unsteady transformation of the Euler equations.

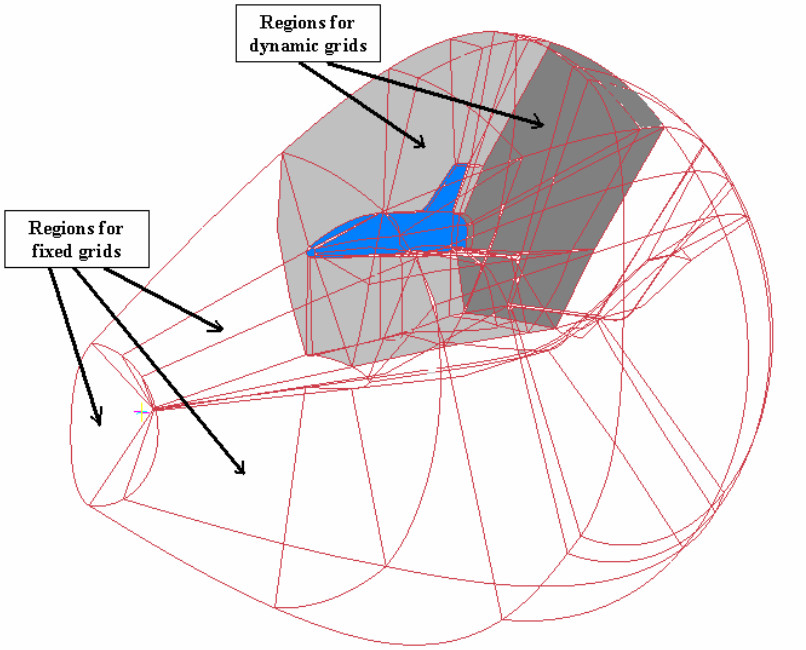

Figure III.3: Computational domain for dynamic grids

CHAPTER IV
NUMERICAL METHOD

1 Numerical Solutions for Euler Equations

Having obtained the unsteady Euler equations in Eq. (II.10) and the grids in Ch. III, this chapter presents the numerical method used for solving the unsteady Euler equations. Such equations have a hyperbolic character with respect to time and allow discontinuities in the solution. For the first character, numerical solutions based on a time-marching are a properly posed mathematical problem in all regions of the flows. For the second character, the used finite volume shock capturing approach can maintain the conservation of flow properties in the discontinuity region. In order to offer the largest flexibility to apply numerical approximations for the spatial and temporal derivatives with different accuracy levels in solving the unsteady Euler Equations, the numerical method based on the separate discretization in space and time – the so called *method of lines* is considered.

Based on the space discretization, numerical methods can be categorized into two groups, namely central difference and upwind difference schemes [54]. The upwind difference scheme is more suitable for flows dominated by a convection, such as the high speed flows around the TSTO space transportation system. This scheme considers physical propagation properties of the Euler equations that are indicated from information on the sign of the Jacobian eigen values. In such a scheme the introduction of the physical properties in the discretization process of the Euler equations can be done at different levels. In the first level, only information on the sign of the eigen values are introduced, whereby the vector of the convective fluxes are split and discretized directionally according to the sign of the associated propagation speeds. This leads to the *flux-vector splitting* scheme. The first flux vector splitting schemes were developed in the beginning of the 1980's by Steger and Warming [55][56] and by Van Leer [57], respectively. The second level of the upwind scheme is based on the solution of locally one-

dimensional Euler equations for discontinuous states at an interface. This corresponds to a Riemann (shock tube) problem. The values either side of the interface are generally termed the *left* and *right* states. In order to reduce the numerical effort required for an exact solution of the Riemann problem, approximate Riemann solvers were developed, e.g., by Oscher et al. [58] and Roe [59]. They are also known as the *flux difference splitting* scheme. Another approach of the upwind scheme with the aim at preventing the generation of numerical oscillations around the shock discontinuities is based on the concept of non-linear limiters. The most popular scheme based on this concept is the Total Variation diminishing (TVD) schemes introduced by Harten [60] in 1983. The principal conditions for the TVD scheme are that maxima must be non-increasing, minima non-decreasing, and no new local extrema may be created.

Furthermore, the new upwind schemes with a primary goal of maximizing accuracy with less computational time and cost were performed by improving the flux vector splitting scheme to have the characteristics like the flux difference splitting. These schemes decompose the flux vector into a convective and pressure (acoustic) parts. This idea is followed by more recent method like the Advection Upstream Splitting Method (AUSM) of Liou et al. [61][62], or the Convective Upwind Split Pressure (CUSP) scheme of Jameson [63]. Further similar approaches are the Low-Diffusion Flux-Splitting Scheme (LDFSS) introduced by Edward [64], or the Mach number–based Advection Pressure Splitting (MAPS) scheme of Rossow [65][66].

Concerning the discretization in time, the numerical methods can be grouped into implicit and explicit schemes. The implicit scheme can produce numerical solutions without any problem related to the numerical stability limitation [67]. However, the numerical algorithm of the implicit scheme is more difficult and requires a more memory space for the computation compared to the explicit scheme.

2 Numerical Methods for Stage Separation of TSTO Space Vehicle Systems

The numerical method for solving the flow problems of stage separation of the TSTO space transportation system considers the finite volume shock capturing method for the spatial discretization and modified AUSM scheme for the convective fluxes evaluation. The temporal discretization uses the explicit scheme of the multistage Runge-Kutta [37]. For the unsteady flow calculations, a dual time-stepping method proposed by Jameson is used [38]. This method redefines the unsteady flow problem into a steady flow problem by introducing a pseudo-time, with the physical time derivative included in the discretized equations.

2.1 Finite Volume Discretization Method

The cell-centered finite volume method is used for the spatial discretization of the unsteady Euler equation. This discretization method assumes that the conservation variables are constant in infinite small control volumes (cells) in the computational domain. Corresponding to different time, the state variables inside the cell will change due to the influence of in-/out- flow of the neighbouring cells through the cell faces. The flow fluxes through the cell faces constitute the continuous values. In particular, the problem of the discontinuity such as shock waves can be handled by the shock capturing technique which allows the shock wave to form within the computational domain as a consequence of the numerical flow-field algorithm.

Using the finite volume method, the unsteady Euler equation in Eq. II.10 can be discretized that written down for each control volume as:

$$\frac{d(\mathbf{Q}\Omega)_{,j,k}}{dt} = -\left[(\mathbf{F}\Delta S)_{\mathbf{i}+\frac{1}{2},j,k} - (\mathbf{F}\Delta S)_{\mathbf{i}-\frac{1}{2},j,k} + (\mathbf{G}\Delta S)_{\mathbf{i},j+\frac{1}{2},k} - (\mathbf{G}\Delta S)_{\mathbf{i},j-\frac{1}{2},k} + (\mathbf{H}\Delta S)_{\mathbf{i},j,k+\frac{1}{2}} - (\mathbf{H}\Delta S)_{\mathbf{i},j,k-\frac{1}{2}}\right] \quad \text{(IV.1)}$$

where $\Omega_{i,j,k}$ is the volume at a cell *i,j,k* and ΔS is the surface area at a cell *i,j,k*.

2.2 Evaluation of Convective Fluxes

The evaluation of the convective fluxes ***F***, ***G***, ***H*** at each cell face in Eq. (IV.1) uses the modified AUSM (Advection Upstream Splitting Method) that developed by taking the positive values of the Flux Vector Splitting (FVS) and Flux Difference Splitting (FDS) upwind schemes. The FVS and FDS are described in detail in Appendix E. The original AUSM scheme proposed by Liou [68][69] treat the convective and pressure terms separately. The convective terms are upstream-biased using the properly defined cell-interface velocity, while the pressure term is strictly dealt with the use of acoustic waves. However, the original AUSM was found to generate local pressure oscillations at shocks and in cases where flow is aligned with computational grid. The modified AUSM suggested by Rediespiel et al [70] has introduced improvement to get the better shock solution that is by switching at the shocks to Van Leer's scheme.

The modified AUSM scheme used in this study is described in detail as follows: the convective flux terms $\mathbf{F}$, $\mathbf{G}$, $\mathbf{H}$ in Eq. (IV.1) can be considered each as the convective and pressure terms. To show the discritization of the modified AUSM scheme, only the term corresponding to $\mathbf{F}$ through a cell surface perpendicular to x direction will be discussed. The other flux terms can be derived in similar way. This flux transportation about mass, momentum, and energy are discritized on a cell surface (*i+1/2, j, k*), which is the middle surface between cell (*i, j, k*) and cell (*i+1, j, k*), and it is written as:

$$\left(\mathbf{F}\Delta\mathbf{S}\right)_{i+1/2,j,k} = \mathbf{F}^{c}_{i+1/2,j,k} \cdot \left|S\right|_{i+1/2,j,k} + \mathbf{p}_{i+1/2,j,k}\left|S\right|_{i+1/2,j,k} \qquad \text{(IV.2)}$$

The term $\mathbf{F}^{c}_{i+\frac{1}{2}}$ is the convective term that characterized with an advective Mach number $M_{i+\frac{1}{2},j,k}$ and a scalar dissipative term, $\Phi_{k+1/2,l,m}$.

$$\mathbf{F}^{c}_{i+\frac{1}{2},j,k} = \frac{1}{2} M_{i+\frac{1}{2},j,k}\left(\mathbf{W}_{i+1,j,k} + \mathbf{W}_{i,j,k}\right) - \frac{1}{2}\Phi_{i+\frac{1}{2},j,k}(\mathbf{W}_{i+1,j,k} - \mathbf{W}_{i,j,k}), \quad \text{(IV.3)}$$

where

$$S_{i+\frac{1}{2},j,k} = \begin{pmatrix} s_x \\ s_y \\ s_z \end{pmatrix}_{i+\frac{1}{2},j,k}, \quad \mathbf{W}_{i,j,k} = \begin{pmatrix} \rho a \\ \rho u a \\ \rho v a \\ \rho w a \\ \rho \mathrm{H} a \end{pmatrix}_{i,j,k}, \quad \mathbf{p}_{i+\frac{1}{2},j,k} = \begin{pmatrix} 0 \\ p_{i+\frac{1}{2},j,k} \\ 0 \\ 0 \\ 0 \end{pmatrix} \quad \text{(IV.4)}$$

S is a surface vector, and its components s_x, s_y, s_z are the projection of S on coordinates *x, y, z*. Furthermore the total enthalpy $\mathrm{H} = (e + p)/\rho$, and a is the sound speed.

From Liou and Steffen [61], the advective Mach number $M_{i+\frac{1}{2},j,k}$ is determined by a combination of wave velocity $M^{\pm}$ on the cell (*i, j, k*) and cell (*i+1, j, k*). This is

$$M_{i+\frac{1}{2},j,k} = M^{+}_{i,j,k} + M^{-}_{i+1,j,k}. \quad \text{(IV.5)}$$

Van Leer defines the Mach number M^{+}_{i} and M^{-}_{i+1} through the "Flux Vector Splitting" method [57] written as follows:

$$M^{+} = \begin{cases} M & if \quad M \geq 1 \\ \frac{1}{4}(M+1)^2 & if \quad |M| < 1 \\ 0 & if \quad M \leq -1 \end{cases} \quad \text{(IV.6)}$$

$$M^{-} = \begin{cases} 0 & if \quad M \geq 1 \\ -\frac{1}{4}(M-1)^2 & if \quad |M| < 1 \\ M & if \quad M \leq -1 \end{cases}$$

Mach number M is defined by the velocities *u, v, w* and the surface vector *S,* where the velocities are evaluated on a cell, that is on cell (*i, j, k*) or cell (*i+1, j, k*) and the surface vector is determined on the surface (*i+1/2, j, k*),

$$M = \frac{1}{|S|}\frac{s_x u + s_y v + s_z w}{a}. \tag{IV.7}$$

Similarly to the advective Mach number term, the pressure is defined as

$$p_{i+\frac{1}{2},j,k} = p^{+}_{i,j,k} + p^{-}_{i+1,j,k}. \tag{IV.8}$$

By a second-order weighted characteristic polynomial of velocity, the terms for pressure are defined.

$$p^{+} = \begin{cases} p & if \quad M \geq 1 \\ \frac{1}{4}p(M+1)^2(2-M) & if \quad |M| < 1 \\ 0 & if \quad M \leq -1 \end{cases} \tag{IV.9}$$

$$p^{-} = \begin{cases} 0 & if \quad M \geq 1 \\ \frac{1}{4}p(M-1)^2(2+M) & if \quad |M| < 1 \\ p & if \quad M \leq -1 \end{cases} \tag{IV.10}$$

For the scalar dissipative term, $\Phi_{k+1/2,l,m}$ in Eq. (IV.3), Radespiel et al. [70] introduce it as a combination of numerical dissipation in the AUSM and Flux Vector Splitting method.

$$\Phi_{i+\frac{1}{2},j,k} = (1-\omega)\Phi^{VL}_{i+\frac{1}{2},j,k} + \omega\Phi^{\text{mod } AUSM}_{i+\frac{1}{2},j,k}. \tag{IV.11}$$

The dissipation in the Flux Vector Splitting method is defined as

$$\Phi^{VL}_{i+\frac{1}{2},j,k} = \begin{cases} \left|M_{i+\frac{1}{2},j,k}\right| & if \quad M_{i+\frac{1}{2},j,k} \geq 1 \\ \left|M_{i+\frac{1}{2},j,k}\right| + \frac{1}{2}(M_{i+1,j,k}-1)^2 & if \quad 0 \leq \left|M_{i+\frac{1}{2},j,k}\right| < 1 \\ \left|M_{i+\frac{1}{2},j,k}\right| + \frac{1}{2}(M_{i,j,k}+1)^2 & if \quad -1 < M_{i+\frac{1}{2},j,k} \leq 0 \end{cases} \tag{IV.12}$$

and the dissipation in the AUSM is written as

$$\Phi^{\text{mod } AUSM}_{i+\frac{1}{2},j,k} = \begin{cases} \left|M_{i+\frac{1}{2},j,k}\right| & if \quad \left|M_{i+\frac{1}{2},j,k}\right| > \tilde{\delta} \\ \dfrac{(M^2_{i+\frac{1}{2},j,k} + \tilde{\delta}^2)}{2\tilde{\delta}} & if \quad \left|M_{i+\frac{1}{2},j,k}\right| \leq \tilde{\delta} \end{cases} \tag{IV.13}$$

where $\tilde{\delta}$ is a small parameter $0 < \tilde{\delta} \leq 0.5$ and ω is a constant $0 < \omega \leq 1$. For $\omega = 0$ the method behaves as the classical van Leer flux vector splitting scheme [70]. In the case of $\omega = 1$ and $\tilde{\delta} = 0$ the original AUSM developed by Liou and Steffan is recovered [61]. The van Leer scheme is more robust but less accurate than the original AUSM scheme. The hybrid flux ensures both the clean and sharp shock resolution of the van Leer scheme and the low diffusive solution of the AUSM in smooth regions. This is realized by relating the parameter ω to the second difference of the pressure,

$$\omega = \max(v_{i,j,k}, v_{i+1,j,k}) \tag{IV.14}$$

$$v_{i,j,k} = \max(1 - \alpha \left| \frac{p_{i-1,j,k} - 2p_{i,j,k} + p_{i+1,j,k}}{p_{i-1,j,k} + 2p_{i,j,k} + p_{i+1,j,k}} \right|, 0). \tag{IV.15}$$

$\upsilon_{i,j,k}$ and $\upsilon_{i+1,j,k}$ are two numerical dissipation parameters with α = O(5). The equation (IV.15) constitutes a sensor shock by checking pressure value in the computational domain. The value of ω is 1 in smooth regions and switches to 0 in the vicinity of shocks.

Furthermore, when the state variables on (*i+1/2, j, k*) simply use the value on (*i, j, k*) or (*i+1, j, k*), then the first order accuracy of the flux is achieved. While, the higher-order accuracy of the flux can be obtained by defining flow variables on the right and left sides of the faces using the variable extrapolation scheme of van Leer. This higher-order flux is called the Monotonic Upwind Scheme for Conservation Law (MUSCL) scheme [71][72]. The general form of the MUSCL scheme is:

$$Q^{+}_{i+\frac{1}{2}} = Q_{i+1} - \frac{s^{+}}{4}\left[(1-\kappa)\Delta_{+} + (1+\kappa)\Delta_{-}\right]Q_{i+1}$$

$$Q^{-}_{i+\frac{1}{2}} = Q_{i} - \frac{s^{-}}{4}\left[(1-\kappa)\Delta_{-} + (1+\kappa)\Delta_{+}\right]Q_{i} \qquad \text{(IV.16)}$$

The forward (Δ_{+}) and backward (Δ_{-}) difference operators are defined as $\Delta_{+}Q_i = Q_{i+1} - Q_i$ and $\Delta_{-}Q_i = Q_i - Q_{i-1}$. The parameter of κ controls the accuracy of the extrapolations, κ = -1 is the second-order fully upwind scheme, κ = 1/3 is the third-order upwind biased scheme, κ = 0 correspond to a second order, upwind-biased linear interpolation and κ = 1 constitutes the second order central scheme. The limiter function *s* is used to prevent the generation of non-physical oscillation of the solution in regions of high gradients (e.g. at shocks). At strong discontinuities, the limiter reduces the slope of the interpolation of flow variables to the face of a cell to be zero (s = 0) in order to prevent the generation of a new extremum. While, in smooth flow regions the limiter obtain a certain value in order to keep the amount of numerical dissipation as low as possible. The limiter of Albada is used in the computation, primarily because of its continuous behaviour [72][73]:

$$s^{+} = \frac{2\,\Delta_{+}Q_{i+1}\,\Delta_{-}Q_{i+1} + \varepsilon}{\left(\Delta_{+}Q_{i+1}\right)^2 + \left(\Delta_{-}Q_{i+1}\right)^2 + \varepsilon} \qquad s^{-} = \frac{2\,\Delta_{+}Q_{i}\,\Delta_{-}Q_{i} + \varepsilon}{\left(\Delta_{+}Q_{i}\right)^2 + \left(\Delta_{-}Q_{i}\right)^2 + \varepsilon} \qquad \text{(IV.17)}$$

The small quantity ε ensures the limiter to behave properly in smooth flow regions.

2.3 Initial and Boundary Conditions

To obtain the real and efficient flow solution, the specification of suitable initial and boundary conditions are required. The initial condition determine the state of the fluid at the time t = 0, or, at the first step of an iterative process. Clearly, the better (the closer to the solution) the initial guess will be, the faster the final solution will be obtained. Therefore, it is important that the initial solution satisfied at least the governing equations and the additional thermodynamic relations. In common practice the initial values for the whole flow field is determined by prescribing the freestream values of pressure, density and velocity component (given as Mach number and angle of attack).

Subsequently, the evaluation of fluxes on boundaries of the computational domain to obtain a well-posed problem for the Euler equations requires the proper definition of boundary conditions. The information concerning the direction of the propagation of the waves plays a very important role in determining the correct boundary conditions. These directions are determined by evaluating the eigenvalues of the Euler equations. At the boundary a value associated with each wave can then be specified or extrapolated depending on the sign of the corresponding eigen value.

There are several types of the boundary conditions in used in the present study, namely solid wall, farfield, symmetry and boundary between blocks. The boundary conditions are applied by introducing additional layers of dummy cells outside the physical domain [7][33]. The purpose of the dummy cells is to simplify the computations of the fluxes, gradients,

dissipations, etc. along the boundaries. This is achieved by the possibility to extend stencils of the spatial discretization scheme beyond the boundaries. Each boundary has the specific numerical treatment that requires a particular care to obtain the appropriate simulation of the real system. The improper implementation can negatively influence to the stability and convergence speed of the simulation. The numerical treatment of the used boundary conditions is given as follows:

2.3.1 Body boundary condition

The specification of the solid boundary condition is relatively straightforward, that is only one eigenvalue is positive so that only one variable may be prescribed, namely the normal velocity. The other variables have to be extrapolated from the interior of the flow domain to the surface. The normal velocity is zero at all time, since no mass or convective flux can penetrate into the surface.

$$\vec{v} \cdot \vec{n} = 0 \qquad \text{at the surface} \tag{IV.18}$$

where $\vec{n}$ denotes the unit normal vector at the surface. The application of the solid boundary is carried out as follows: The velocity in each dummy point consists of two components: the normal component which is determined from the corresponding mirrored value in the computational domain and the tangential component which is obtained from the extrapolation from the computational domain. Due to the vanishing normal velocity at the body surface, the vector of the convective fluxes equation (II.10) reduces to the pressure terms alone.

$$F_{c\,\mathbf{b}ody} = p_{\mathbf{b}ody} \begin{bmatrix} 0 \\ n_x \\ n_y \\ n_z \\ 0 \end{bmatrix} \tag{IV.19}$$

with the p_{body} being the body pressure.

2.3.2 Farfield boundary condition

The implementation of the farfield boundary conditions has to fulfil two basic requirements. First, the truncation of the domain should have no notable effects on the flow solution as compared to the infinite domain. Second, any outgoing disturbances must not be reflected back into the flow field [33][74]. Various methodologies were developed which are capable of absorbing the outgoing waves at the farfield boundaries [41][75][76].

One of the methods, proposed by Whitfield and Janus [76], which based on the characteristic variables of the one-dimensional Euler equations (II.10) normal to the boundary surface pointing outward is used in the present study. Two basic flow situations at the farfield boundary are sketched in Fig. IV.1. The flow can either enter or it can leave the domain. Therefore, depending on the local Mach number, there are four different types of farfield boundary conditions: supersonic inflow and outflow, subsonic inflow and outflow. Only two supersonic farfield boundaries are explained that used in the calculations.

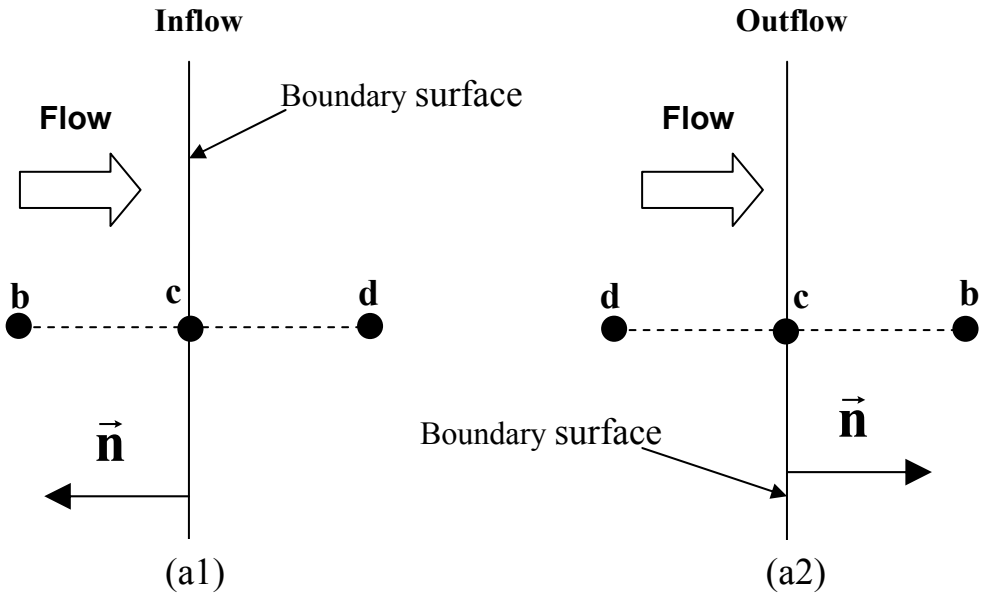

Figure IV.1: Farfield boundary conditions

- **Supersonic Inflow and Outflow**

For supersonic inflow, all eigenvalues are negative. Since the flow is entering into the computation domain, the conservative variables on the boundary (point **c** in Fig. IV.1 (a1)) are set at the freestream values. Thus,

$$\mathbf{Q}_c = \mathbf{Q}_b . \tag{IV.20}$$

The values $\mathbf{Q}_b$ are specified based on the given Mach number and two other flow parameters, such as pressure and temperature. While, for supersonic outflow all eigenvalues are positive. The flow leaves the computation domain and all conservative variables at the boundary must be extrapolated from the values inside the computation domain toward the boundary. This leads to the following set of the conditions [76].

$$\begin{aligned}
p_c &= \frac{1}{2}\left\{ p_b + p_d - \rho_0 a_0 \left[n_x \left(u_b - u_d\right) + n_y \left(v_b - v_d\right) + n_z \left(w_b - w_d\right) \right] \right\} \\
\rho_c &= \rho_d + \left(p_c - p_d\right)/ a_0^2 \\
u_c &= u_d + n_x \left(p_d - p_c\right)/\left(\rho_0 a_0\right) \\
v_c &= v_d + n_x \left(p_d - p_c\right)/\left(\rho_0 a_0\right) \\
w_c &= w_d + n_x \left(p_d - p_c\right)/\left(\rho_0 a_0\right)
\end{aligned} \tag{IV.21}$$

where ρ_0 and a_0 represent reference state. The reference state is set equal to the state at the interior point (point **d** in Fig. IV.1).

2.3.3 Symmetry boundary condition

The first condition to be met at the symmetry boundary is that there is no flux across the boundary. The following gradients have to vanish:

- gradient normal to the boundary of the scalar quantity, namely $\vec{n} \cdot \vec{\nabla} S = 0$
- gradient normal to the boundary of the tangential velocity, $\vec{n} \cdot \vec{\nabla}\left(\vec{v} \cdot \vec{t}\right) = 0$
- gradient along the boundary of the normal velocity , $\vec{t} \cdot \vec{\nabla}\left(\vec{v} \cdot \vec{n}\right) = 0$

where S stands for the scalar variable and $\vec{t}$ denotes the vector tangential to the symmetry boundary.

2.3.4 Boundary between grid blocks

For the multiblock grid, the boundary of each block may be divided into a number of non-overlapping patches (see Fig. III.4). The physical solution in a particular block will depend on the flow in one or multiple neighboring blocks. The exchange of flow properties between two blocks is performed in two steps as sketched in Fig. IV.2. In the first step, the variables from the part of the domain, which is overlapped by the dummy layer of the adjacent patch are written to the own dummy cells or to a temporary storage (A' and B' in Fig. IV.2). This is done for all blocks. In the second step, the data in A' and B' is exchanged between both blocks. This means that A' is written to the dummy layers of the block B and B' to the dummy layers of block A. If the two patches have a different orientation, the data are transformed accordingly. In cases where the grid lines do not match at the block interface, further operations are required as described in detail [33][50][51].

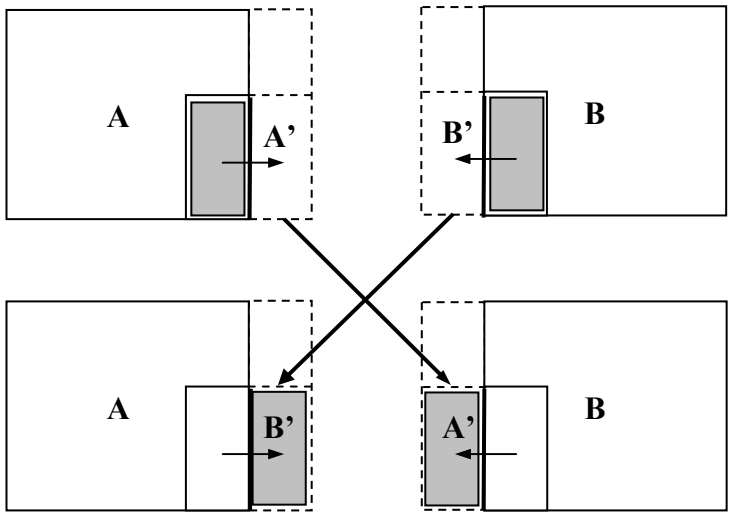

Figure IV.2: Exchange of flow variables between two blocks A and B

2.4 Temporal Discretization

After having determined all terms in the Right-hand side of the equation (IV.1) both inside of the computational domain and on the boundaries, the

further step is to integrate in time of the equation system. The system equation (IV.1), written down for all control volume $\Omega_{i,j,k}$ can be rewritten as a system of coupled ordinary differential equation in time, as follows.

$$\frac{d(\Omega \mathbf{Q})_I}{dt} = -\mathbf{R}_I \tag{IV.22}$$

where **R** is the residual and the index *I* denotes the particular control volume. The residual is a non-linear function of the conservative variable **Q**. This equation system has to be integrated in time, either to obtain a steady-state solution ($\mathbf{R}_I = 0$) or to reproduce the time history of an unsteady flow.

Solutions of the steady flow use a static grid so that the cell Ω can take outside from the equation (IV.22) resulting the time derivative as follows

$$\frac{d\mathbf{Q}_I}{dt} = -\frac{1}{\Omega_I}\,\mathbf{R}_I \tag{IV.23}$$

In order to solve the system of equation given by Eq. (IV.23) the explicit multistage time-stepping scheme is employed. This scheme was first proposed Jameson et al. [37]. An m-stage of Runge-Kutta scheme are written as

$$\begin{aligned}
&\mathbf{Q}_I^{(0)} = \mathbf{Q}_I^n \\
&\mathbf{Q}_I^{(1)} = \mathbf{Q}_I^{(0)} - \alpha_1 \frac{\Delta t_I}{\Omega_I}\mathbf{R}_I^0 \\
&\bullet\bullet\bullet\bullet \\
&\mathbf{Q}_I^{(m-1)} = \mathbf{Q}_I^{(0)} - \alpha_{m-1} \frac{\Delta t_I}{\Omega_I}\mathbf{R}_I^{m-2} \\
&\mathbf{Q}_I^{(m)} = \mathbf{Q}_I^{(0)} - \frac{\Delta t_I}{\Omega_I}\mathbf{R}_I^{m-1} \\
&\mathbf{Q}_I^{n+1} = \mathbf{Q}_I^{(m)}
\end{aligned} \tag{IV.24}$$

with

$$\Delta t_I = CFL \ \frac{\Omega_I}{\left(\Lambda_{\xi,\max} + \Lambda_{\eta,\max} + \Lambda_{\zeta,\max}\right)_I} \tag{IV.25}$$

and CFL is in range of (0,1) and Ω_I is the volume of the cell in curvilinear coordinates, $\Lambda_{\xi,}\Lambda_{\eta,}\Lambda_{\zeta}$ are characteristic values of Jacobian matrix [7]. In the expression of Eq. (IV.25), α_k represents the stage coefficients given as follows

$$\alpha_1 = \frac{1}{m}, \quad \alpha_2 = \frac{1}{m-1}, \bullet\bullet\bullet\bullet, \ \alpha_{m-1} = \frac{1}{2}, \ \alpha_m = 1 \tag{IV.26}$$

The scheme starts from a known solution $\mathbf{Q^n}$ and employs the evaluation of the corresponding residual at intermediate states with the use of suitable boundary conditions to obtain a new solution $\mathbf{Q^{n+1}}$ at time ($t + \Delta t$). In order to overcome the restricted stability of the explicit scheme, numerical artificial dissipation is added in the residual for a certain stage (77). In the present study, the calculations of steady flow use the first order Runge-Kutta scheme to obtain reasonable solutions with less computational time.

In the case of moving grids for unsteady flow calculation, the new size of the control volume, i.e., Ω^{n+1} changes and has to satisfy the Geometry Conservation Law (see Appendix A). The solutions of the unsteady flow are performed by employing the dual time methodology proposed by Jameson [38]. The dual time-stepping approach is a second order in time that written as

$$\frac{3\left(\Omega\right)_I^{\mathbf{n+1}}\mathbf{Q}_I^{\mathbf{n+1}} - 4\left(\Omega\right)_I^{\mathbf{n}}\mathbf{Q}_I^{\mathbf{n}} + \left(\Omega\right)_I^{\mathbf{n-1}}\mathbf{Q}_I^{\mathbf{n-1}}}{2\Delta t} = -\mathbf{R}_I^{\mathbf{n+1}} \tag{IV.27}$$

where Δt denotes the global physical time step. Equation (IV.27) employs a 3-point backward-difference approximation of the time derivative in Eq. (IV.22). For the numerical calculation, this equation is approximated by introducing a pseudo-time variable t^* and can written as

$$\frac{d}{dt^*}\left(\Omega_I^{n+1}\mathbf{Q}_I^*\right) = -\mathbf{R}_I^*\left(\mathbf{Q}_I^*\right), \tag{IV.28}$$

where $\mathbf{Q}^*$is the approximation of Q^{n+1}. The unsteady residual is defined as

$$\mathbf{R}_I^*\left(\mathbf{Q}_I^*\right) = \mathbf{R}_I\left(\mathbf{Q}_I^*\right) + \frac{3}{2\Delta t}\left(\Omega_I^{n+1}\right)\mathbf{Q}_I^* - S_I^* \tag{IV.29}$$

All terms which are constant during the time-stepping in Eq. (IV.29) are gathered is a source term, i.e.,

$$S_I^* = \frac{2}{\Delta t}\left(\Omega\right)_I^{\mathbf{n}}\mathbf{Q}_I^{\mathbf{n}} - \frac{1}{2\Delta t}\left(\Omega\right)_I^{\mathbf{n-1}}\mathbf{Q}_I^{\mathbf{n-1}} \tag{IV.30}$$

To solve the pseudo problem in Eq. (IV.28), the explicit multistage Runge-Kutta scheme in Eq. (IV.24) is used by employing the pseudo-time step t^* and , the new size of the control volume Ω^{n+1}. The time-marching process is started with the values of the steady solution. Then, it is continued until the values of the conservative variable at the new pseudo-time level ($\mathbf{Q}_I^*$) approximates the conservative value at $t + \Delta t$ ($\mathbf{Q}_I^{n+1}$) with sufficient accuracy i.e. when the residual $\mathbf{R}_I^*$ reduces by three order of magnitude.

3. Unsteady Flow Simulations

The procedure of the calculations of the unsteady separation of the TSTO space transportation system follows the flowchart given in Fig IV.3. The computation starts with the input data of the steady flow solution. Subsequently, the unsteady simulations for the first time step according to a

given path of the orbital stage are computed by solving the unsteady Euler equations with the numerical method discussed in the section 2 until the residual reaching the convergence criteria or a given iteration number. The second time step and the subsequent steps can be computed with the similar way. Each time step, the grid distribution around the orbital stage must be adjusted to the movement of the orbital stage and the fixed outer boundaries. The improvement of the grid quality is performed by solving Laplace's equation.

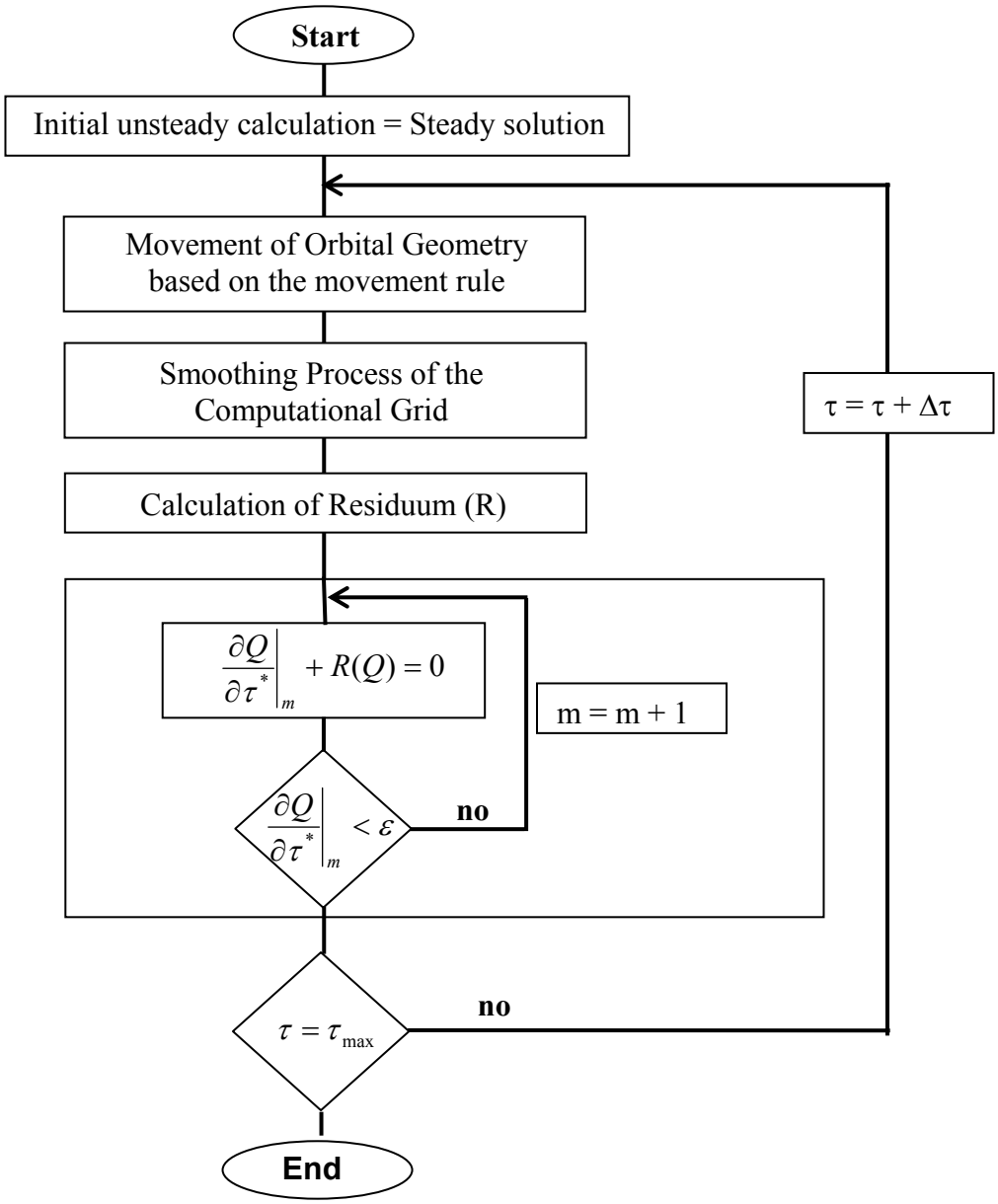

Figure IV.3: The flow chart of the unsteady calculation [Ref: 7]**.**

CHAPTER V
STEADY AERODYNAMICS OF STAGE SEPARATION OF TSTO SPACE VEHICLE SYSTEM ANALYSIS

In this chapter the analysis of the steady aerodynamics of stage separation of the TSTO space vehicle system is performed using two configurations, namely the EOS – flat plate and EOS - ELAC1C. The efficiency of the simulation method including the accuracy and computation time is investigated at various grid aspects on the flat plate and EOS model. The computational results are compared to the corresponding experimental data at various conditions to validate the simulation method for both the configurations. In addition, the effects of the parameters of quasy-steady of the stage separation including orbital stage angle of attack, carrier stage angle of attack and separation distance as well as Mach number on flow features and aerodynamic forces and moment of the space vehicle system are studied. The chapter starts with the important information about the experimental and computational tests.

1 Experiment : Test Models and Conditions

Experimental data for the validation are taken from the supersonic wind tunnel T-313 at ITAM (Institute of Theoretical and Applied Mechanics, Russian Academy of Sciences, Siberian Branch), Novosibirsk for the low hypersonic speed [11] and Shock Tunnel TH2-D of the RWTH Aachen for the high hypersonic speed [12][78].

Related to the T-313 wind tunnel at the ITAM, the test models of the flat plate /EOS configuration and EOS /ELAC1C configurations mounted in the wind tunnel test section are shown Figs. V.1 and V.2, respectively. The EOS and ELAC1C models were manufactured at the ITAM with scale of 1:150. The EOS test model has a length of 192 and a height of the total body of 63.5 mm and a wide of the wing span of 108 mm. While, an overall length

of the ELAC1C test model is 480 mm and a span width of 262 mm. The moment reference point is 0.65 of the EOS length from the EOS nose [79].

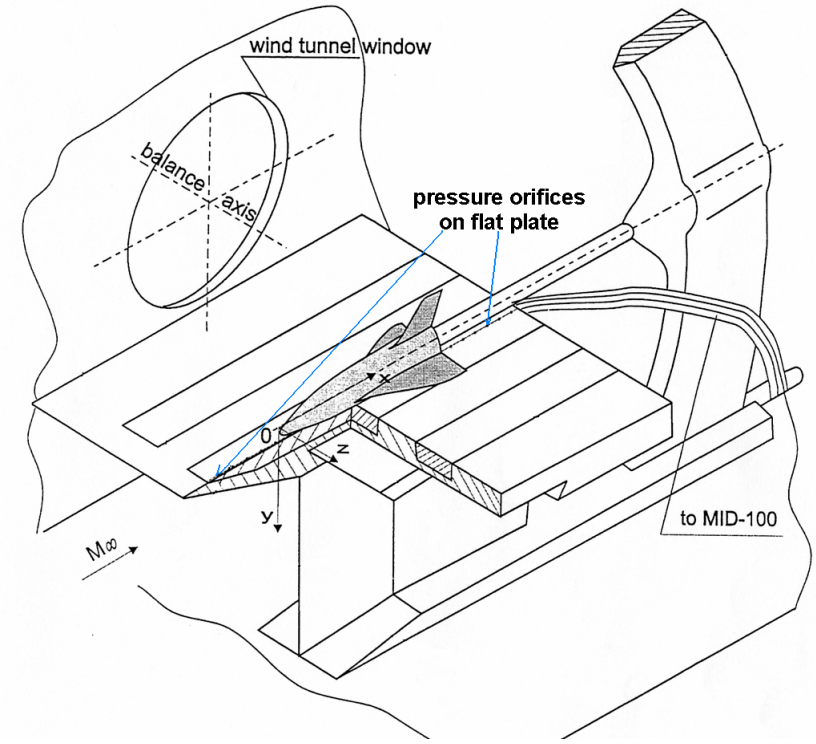

Figure V.1: The test model of the EOS - flap plate [Ref. 79]

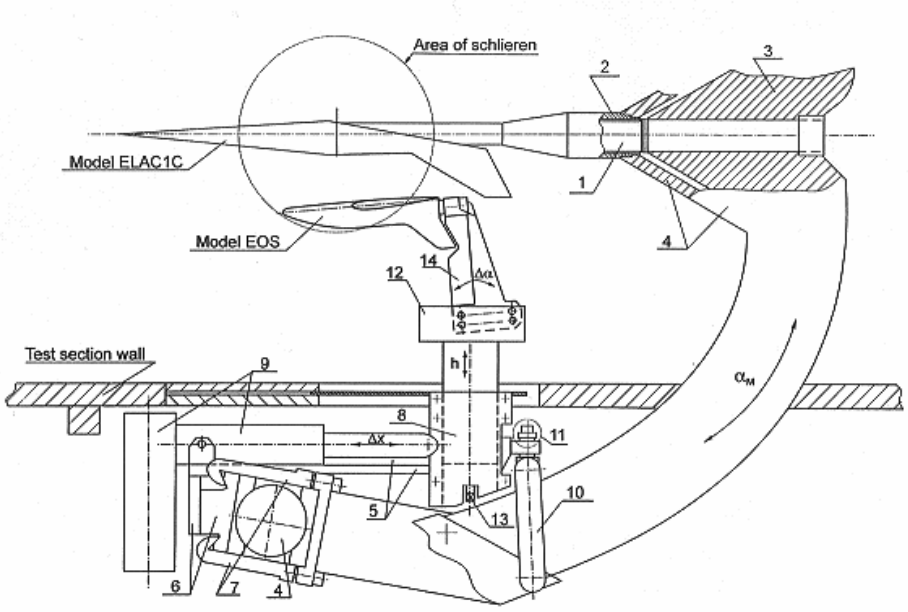

Figure V.2: The test model of the EOS - ELAC1C [Ref. 79]

The two-stage separation is simulated in a quasy-steady manner by mounting the upper stage at different vertical positions h/l_{EOS} as well as at different orbital stage angles of attack $\Delta\alpha$ relative to the lower stage. In addition, the experiment tests were carried out for different angles of attack α of the lower stage.

The measurements at the wind tunnel T-313 of the ITAM include aerodynamic loads, a visualization of flow pattern, and pressure distribution. An automatic four-component mechanical balance is employed to measure the loads acting on the carrier stage model ELAC1C. This balance is fitted with an arm system to decompose the total force and moments into the aerodynamic components lift and drag forces as well as pitching and rolling moments. The instrumental error of the mechanical balance is less than 0.1% of the highest load. An internal six-component strain-gauge balance is used to acquire the loads acting on the orbital stage model EOS. The construction of this balance is made in the form of a tail sting measuring all components of aerodynamic forces and moments. The instrumental error of the strain-gauge balance is less than 0.05% of the highest load [11]. The flow patterns around the separating models are visualized using a standard interfering shadowgraph to observe and register the density gradients of the air flow in the plane of the velocity vector. A specific device connects a CCD camera to the shadowgraph instrument through which digitized images of the Schlieren pictures are sampled by using frame grapplers installed in a PC. In addition, the measurement of pressure distribution at the flat plate was performed using pressure orifices made along on the line on which the EOS symmetry plane and flat plate intersect as shown in Fig. V.1.

The test conditions in the T-313 wind tunnel are as follows: The free-stream Mach number is kept constant at a value of M_∞ = 4.04. The corresponding Reynolds number per 1 m is Re_m = 50.0 x 10^6 and the related dynamic pressure is q_∞= 73.5kPa. The static flow at the plenum chamber is a free-stream temperature, T_∞ = 294 ° K and free-stream air pressure, p_∞ = 6.4 kPa.

The angles of attack of the entire configuration are adjusted for the load measurements at α= 0°, 1°, 2°, 3°, 4°, 5° and 5.7°. For the tests of the quasy-steady stage separation, the orbital stage EOS is placed at two vertical positions relative to the flat plate, namely at h/l_{EOS} = 0.150 and 0.225, and at three vertical positions relative to the carrier stage ELAC1C, namely at h/l_{EOS} = 0.225, 0.325 and 0.450. At each vertical station the angles of attack of the EOS are varied with values of $\Delta\alpha$ = 0° and 3° relative to flat plate and with values of $\Delta\alpha$ = 0°, 2° and 5° relative to the ELAC1C [11].

While, in the Shock Tunnel TH2-D the test model of 1/100-scale of the EOS vehicle is used. Based on the scale, a total length of the EOS is 288 mm with a maximum body height of 100.6 mm, a middle height of 48.6 mm and a span width is of 162 mm. The size and experimental equipment for the EOS model are shown in Fig. V.3. The moment reference point is on the middle point of the body length [12].

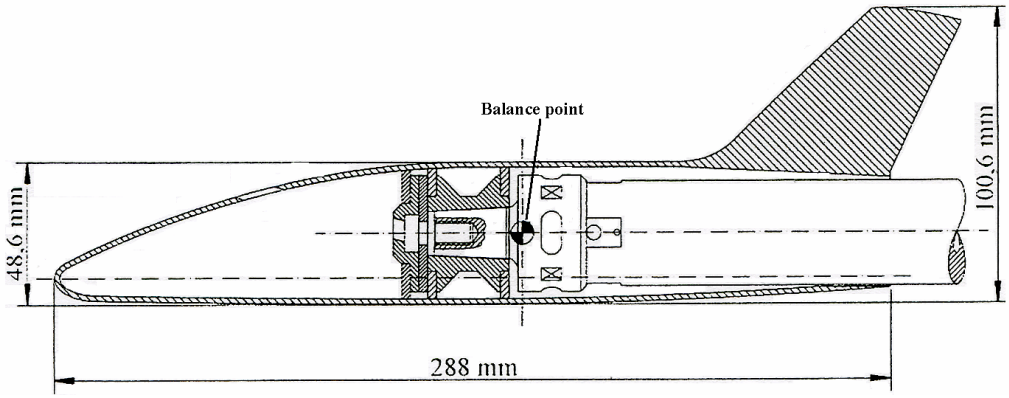

Figure V.3: The test model of the EOS - flat plate at
the Shock Tunnel TH2-D [Ref. 12]

Similarly, the measurements using the Shock Tunnel TH2-D include the visualization of flow pattern around the model, aerodynamic loads and pressure distributions. As shown in Fig. V.4, the pressure orifices are located on the lower surface of the EOS at the interception line between the

underside surface of the EOS and the plane with x = 0.6 L_{EOS}; x= 0.75 L_{EOS} and y = 0 (symmetry line).

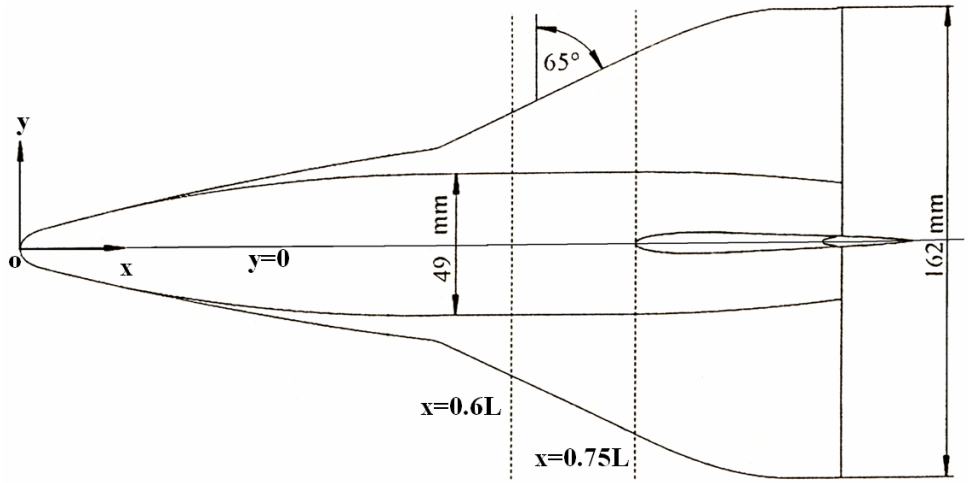

Figure V.4: Pressure measurement sections at x = 0.6 l; 0.75 l, and y = 0 [Ref. 12].

In this experiment, the test condition was set as follows: the free-stream Mach number is M_∞ = 7.9. The corresponding Reynolds number based on one meter long is Re_m = 7.6 x 10^6 free-stream temperature. The other related parameters include a free-stream temperature of T_∞ = 180 ° K, free-steam velocity of V_∞ = 2120 [m/s], free-stream air pressure, p_∞ = 2.27 [kPa] and free-stream density, ρ_∞ = 0.0436 [Kg/ m^3].

2 Computational Test : Facilities, Procedures and Test Cases

2.1 Computational Facilities

The computations of the two stage space vehicle model are performed in Institute of Fluid Mechanics at Technical university of Munich using the computational facilities including computer hardwares, such as HP Visualize J282 workstation and Parallel-vector computing Fujitsu VPP700. The workstation is used for computing the grids. The latter computer used for flow computations has 52 processors and the maximum memory for each processor is 2048 MB, and softwares of the DDN ICEM, HEXA ICEM, the

house developed codes based on the Euler solutions, and TECPLOT post processor.

2.2 Computational Procedures

2.2.1 Topology and Mesh Generation

The generation of the block topology is initiated by defining all boundaries of the computational domain including the definition of the body boundary (geometry surface) as well as farfield and symmetry boundaries. Concerning the geometry surface of the TSTO space vehicle, the original surface is as a computer-aided design (CAD) surface, where the CAD system represents it with a set of structured points or patches. The CAD surface is imported and then converted into a non-uniform rational B-Splines (NURBS) surface representation using the ICEM DDN [80]. The identification of the names of surface for the multiblock grids is also accomplished to distinguish every surface of interest and to avoid a missing projected surface.

The block topology model can be then generated on the underlying CAD geometry surface using a special tool called O-grid available in the ICEM HEXA to obtain five LIVE blocks and one DEAD block. The DEAD region is used to locate the computational model with no grid inside. In addition, the complex geometry which contains the wings, vertical stabilizer, winglets, etc, requires additional dead blocks to cover the detail geometry. This is done through the splitting of the existing LIVE blocks using the O-grid tool. As the result, the complete O-O block topology for the flat plate and EOS model consists of 22 LIVE blocks describing the half configuration as shown in Fig. V.5. While, the computational domain of the half configuration of the detailed ELAC1C and EOS requires 45 LIVE blocks arranged in the O-O topology as shown in Fig. V.6.

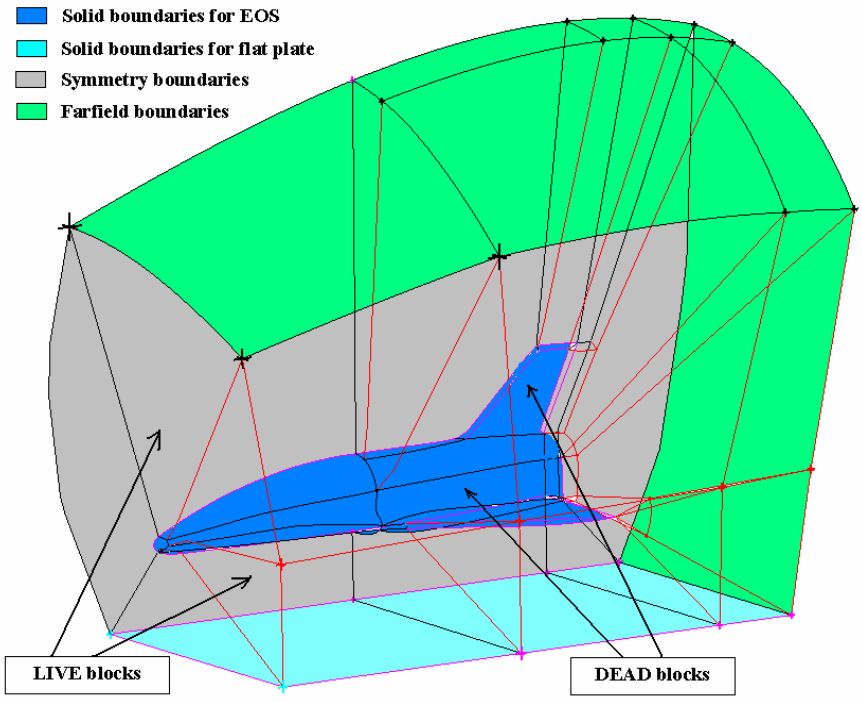

FigureV.5: Topology and blocks for the EOS – Flat Plate configuration.

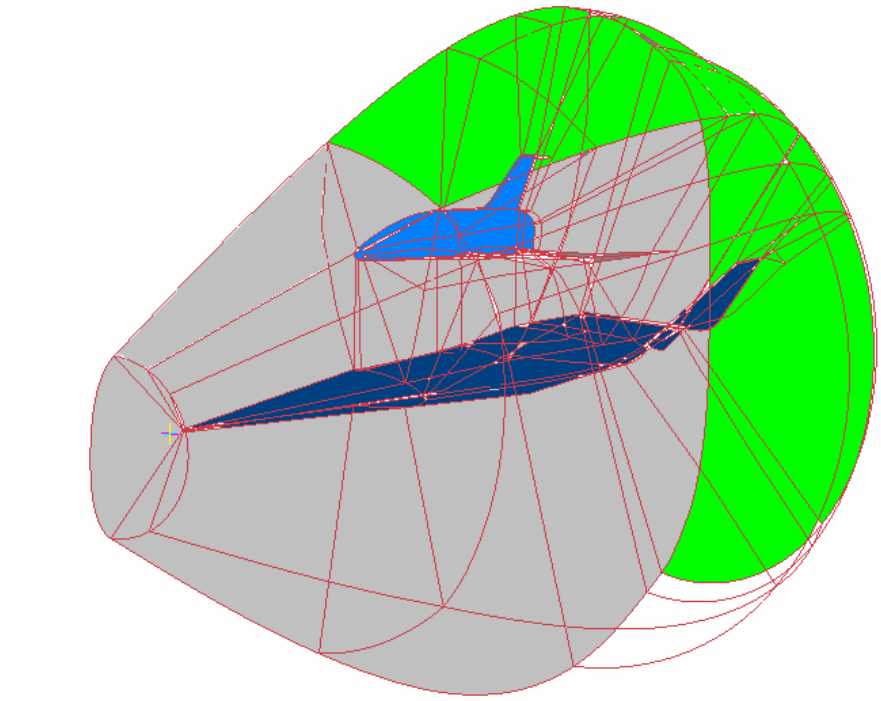

Figure V.6: Topology and blocks for the EOS – ELAC1C configuration.

Once the overall blocks are prepared, points for each block are distributed along the edges of the blocks. The distribution of the mesh points is performed to represent adequately the geometrical shape of the body and it is necessary to concentrate them in the regions with high gradients of the body contour and flow variables, such as on the leading- and trailing-edge sections of the main wing and the vertical tail of the EOS and fixed winglets of the ELAC1C, and in the wake region behind the base of both the vehicles as shown in Fig.V.7. In addition, the point distribution becomes denser when the points approaching the body surface. The generation of the grids is started from all the internal points on the faces by interpolating them and then continued to the points inside the block volumes.

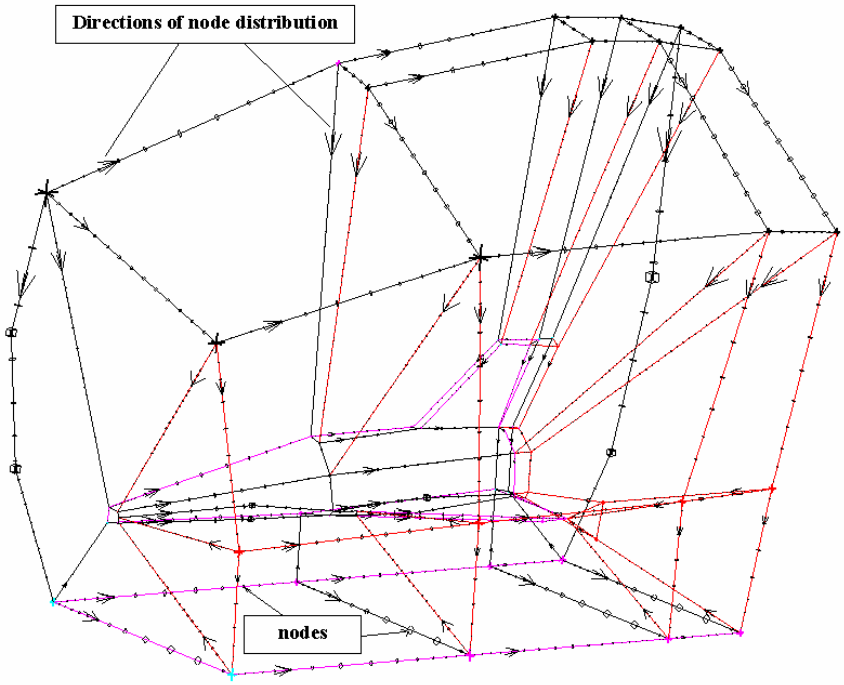

Figure V.7: Points distributions along the edge of the block.

To study the influences of grid quality on the accuracy and computational time of the numerical simulation, several grid cases with differences in grid number and smoothness are generated on the orbital stage EOS and flat plate. As the result, three different grid numbers are generated for the

calculations, namely the first grid has 113.355 cells and 144.650 nodes referred to as the coarse grid, the second one referred to as the standard grid has 251.931 cells and 295.395 nodes, and the third one with 493.215 cells and 565.610 nodes referred to as the finer grid. The off-body distance of each grid model is about $1x\ 10^{-5}$. Concerning the point distribution, the first grid has a nearly uniform grid distribution along the middle part of the fuselage and the others have denser grid distributions in the same location. The basic grid result for the standard grid is shown in Fig. V.8.

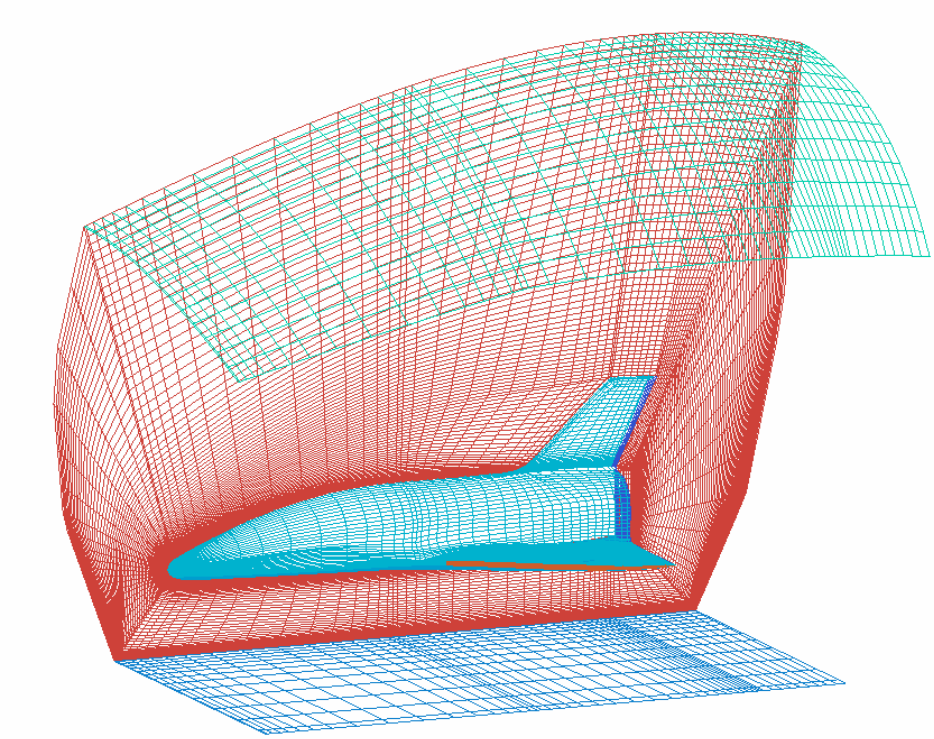

Figure V.8: The initial standard grids.

Related to the grid smoothness, the grid smoothing process is performed by the use of the Poisson algorithm (in chapter III) with the basic grid as the initial input. The convergence solution with a sufficient smoothness is fulfilled if the change in the source strength of the Poisson equation is below 10^{-4}. The smoothed grids of the EOS – flat plate model is shown in Figs. V.9. The improvement of the orthogonal grid presents in the whole domain around the vehicle.

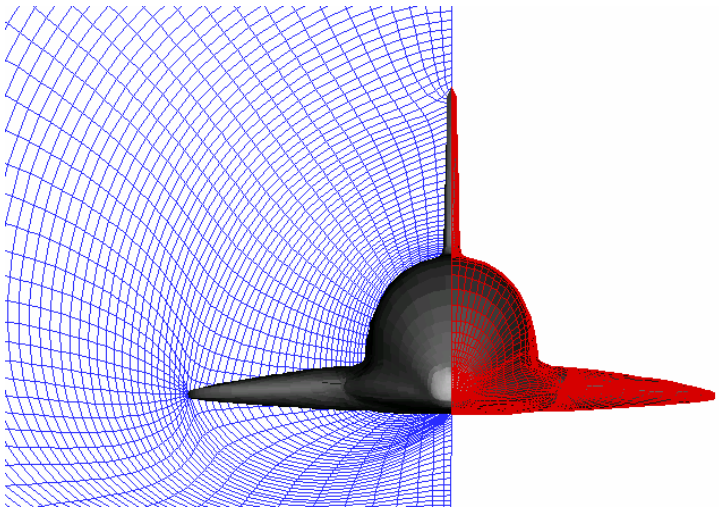

Figure V.9: The smoothed grids of the EOS – flat plate configuration

Furthermore, the basic and smoothed grids for the EOS and ELAC1C configuration are shown in Figs.V 10 and 11, respectively. The grids consist of 1.177.630 volumes and 1.308.400 nodes.

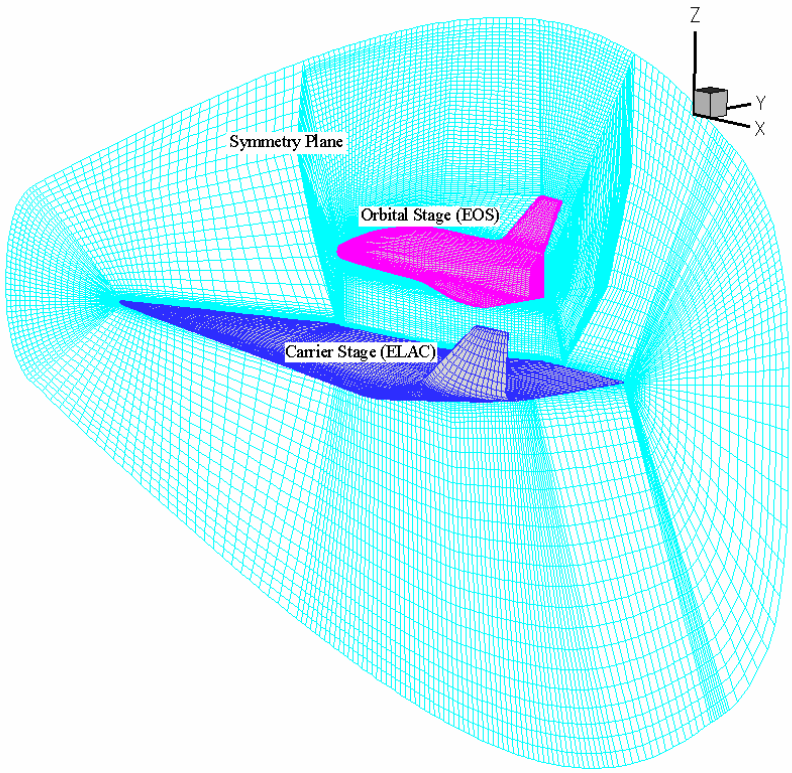

Figure V.10: Initial grids of the EOS and ELAC1C configuration.

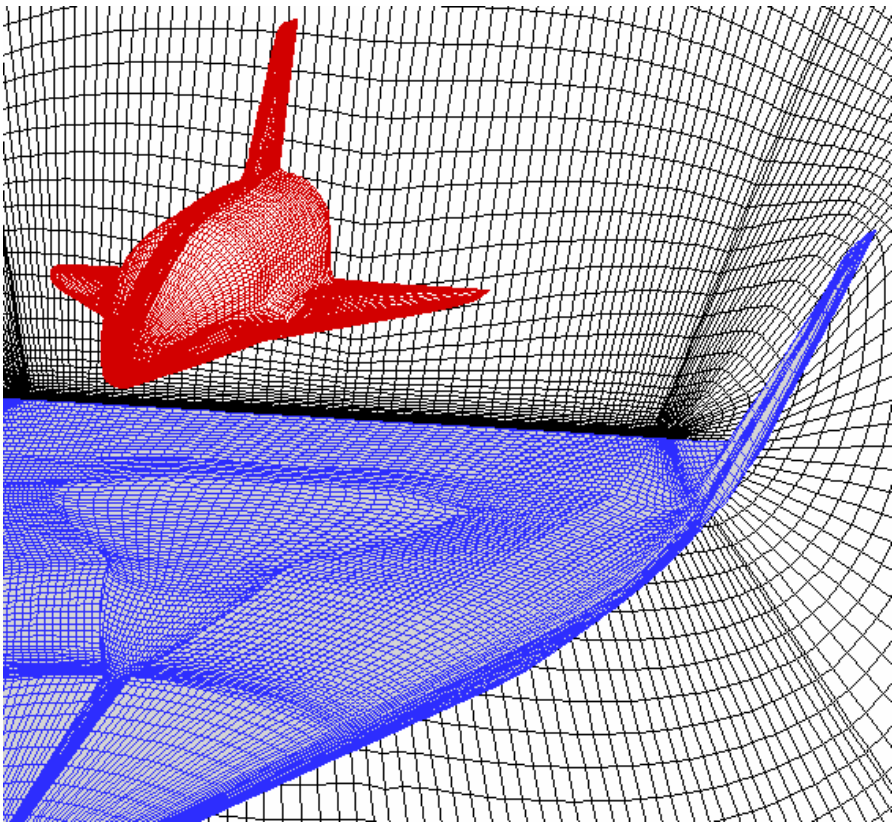

.

Figure V.11: The smoothed grids of the EOS and ELAC1C configuration.

2.2.2 Obtaining Numerical Flow Solutions

Steady flow computations are obtained by iteratively solving the Euler equations. The numerical method used for solving the Euler equation is explained in chapter IV. The computations require inputs of the physical and numerical parameters as well as the generated grids in the whole computational domain and the associated logic file containing the information of the block connectivity. The physical parameters include geometry reference, Mach number, angle of attack, side-slip angle and free-stream flow condition. Moreover, the numerical parameters consist of CFL number, convergence limit and artificial viscosity. The final steady state solution can be obtained if the residual of the density is below 10^{-5}. Then, the numerical results can be interpreted using the post-processing tools (TECPLOT software) as flow contours, plots of pressure distribution and aerodynamic force and moment coefficients, geometry and mesh pictures.

2.3 Computational Test Cases

For the flat plate and EOS configuration, totally nine test cases are computed for studying the effects of grid quality including grid orthogonality and grid distribution on the accuracy and efficiency of the simulation method and for investigating the effects of the separation parameters on flow field and aerodynamic characteristics of the space vehicle. All computational test cases for the flat plate and EOS configuration are named with small character "a" followed by a number given in Table V.1.

Case	Mach number	h/l_{EOS}	$\Delta\alpha / \alpha$ (in deg.)	Smooth Accuracy	Number of Grid (10^3)
a1	4.04	0.150	0 / 0	10^{-2}	113
a2				10^{-3}	113
a3				$3x10^{-4}$	113
a4				10^{-3}	252
a5				10^{-3}	493
a6	4.04	0.225	0 / 0	10^{-3}	493
a7		0.225	3 / 0	10^{-3}	493
a8	6.80	0.150	0 / 0	10^{-3}	493
a9	7.90	0.150	0 / 0	10^{-3}	493

Table V.1: Computational test cases for the flat plate and EOS configuration.

Furthermore, for the EOS - ELAC1C configuration, the test conditions focus on the variations of angles of attack (α), orbital stage angles of attack ($\Delta\alpha$) and relative distances between the orbital stage and the carrier stage (h/l_{EOS}). The free stream Mach number during the separation is determined based on the setting of Mach number at the experimental test. Five different test cases taken from the wind tunnel experiment tests at the ITAM [11] are chosen as

references for the computational tests. Similarly, the name of the computational cases for the ELAC1C and EOS configuration is initiated with a character "b" followed with a number. The details of the test conditions for the steady flow calculations of the EOS and ELAC1C space vehicles are given in Table V.2.

Case	Mach number	Relative distance (h/L_{EOS})	Relative angle of EOS ($\Delta\alpha$) in deg.	Angle of attack (α) in deg.
b1	4.04	0.225	0.0	0.0
b2				3.0
b3			2.0	0.0
b4			5.0	0.0
b5		0.325	0.0	0.0

Table V.2: Computational test cases for the ELAC1C and EOS configuration.

The results of the computed aerodynamic characteristics of the steady stage separation of the EOS – flap plate and EOS –ELAC1C configurations are given in Appendices F and G, respectively.

3 Effects of Numerical Grids

3.1 Effects of Grid Smoothing

Three cases related to the grid smoothing effects namely cases a1, a2 and a3 are compared. The smoothed grids with iteration numbers of 1, 50 and 500 are shown in Figs V.12 (a, b and c), respectively. With increasing the number of iteration, the grid quality over the computational domain increases indicated by the decreasing grid error that is 10^{-2}, 10^{-3} and $3x10^{-4}$ for the cases a1, a2 and a3, respectively. The particular improvement on the grids behind the EOS is shown in Fig. 12.

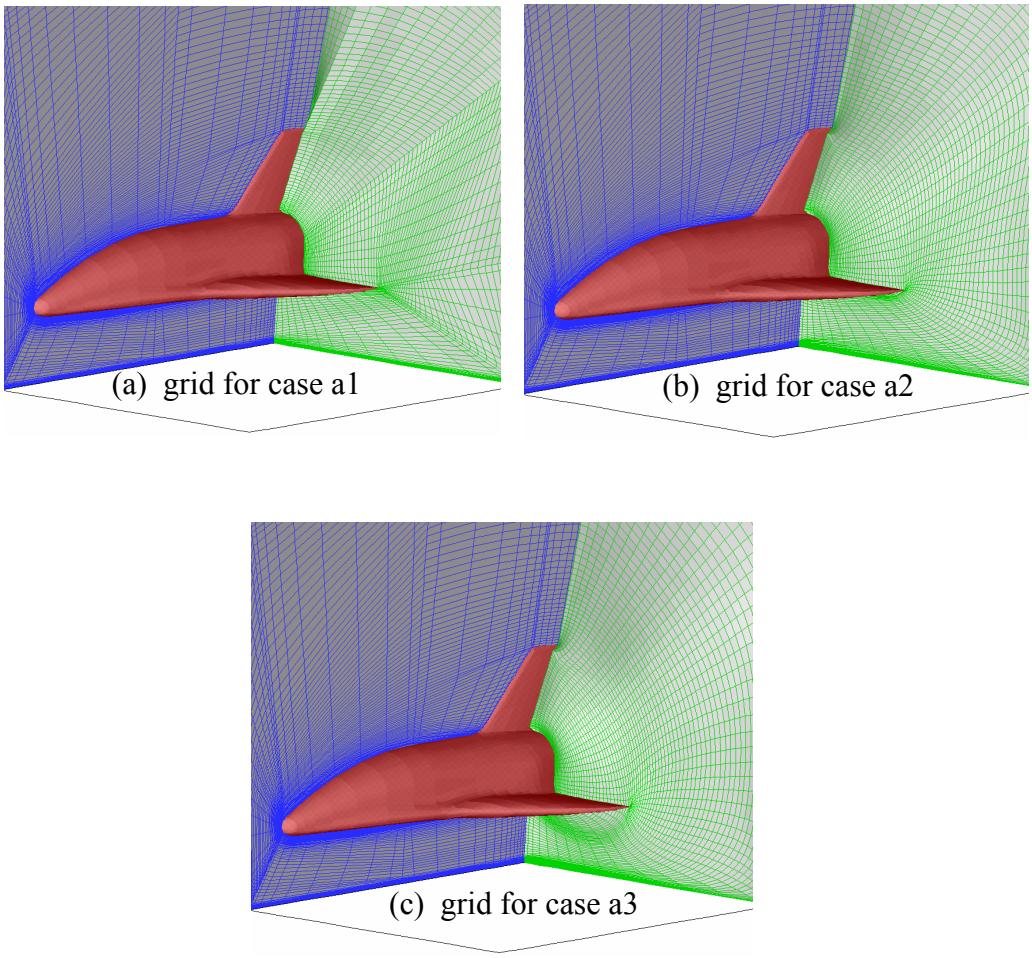

Figure V.12: The effect of grid smoothing on the grid quality.

The effect of the grid smoothing on the efficiency of the calculations is shown in the convergence history in Fig. V.13. Increasing the grid quality due to the smoothing process causes the decreased computational time that required reaching at the same convergence value. The higher grid quality means the grids becoming orthogonal or continuous cell growth. At the boundary blocks, the continuous cells will decrease the computation error during the exchange data of the flow properties between two blocks. This gives a faster reduction of the residual every iteration over the whole computational cells where as the time per iterations and memories used for every time iteration as almost same for all cases as given in Table V.3.

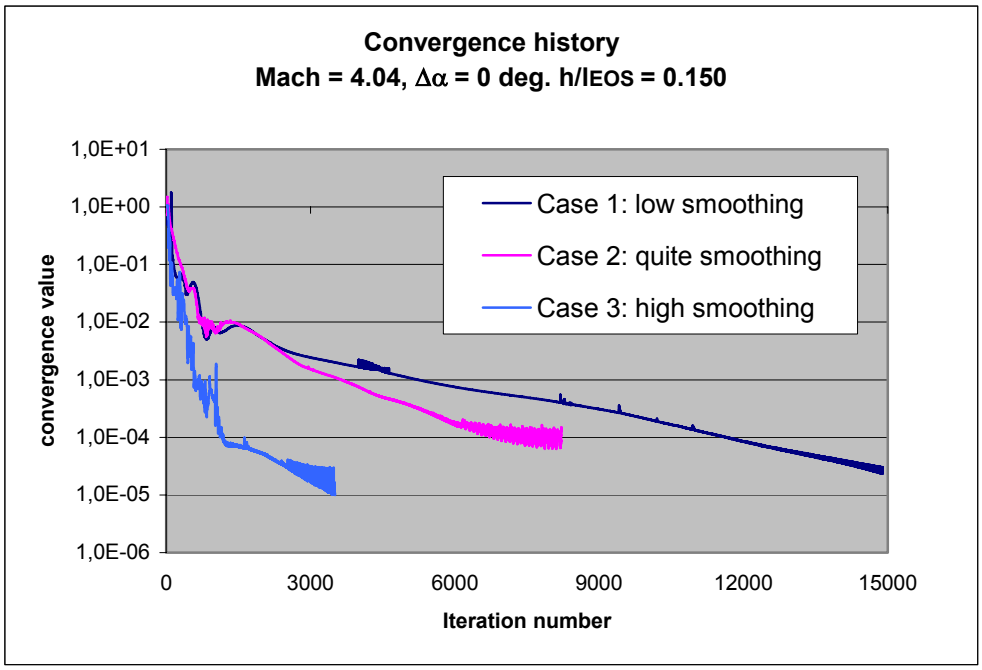

Figure V.13: Convergence History of the smoothing grid effects.

Case	Time per iteration (seconds)	Iteration number for convergence	Total time (seconds)	Memory used
a1	10.33	14900	153917	208
a2	10.30	8200	84706	208
a3	10.31	3500	36085	208

Table V.3: Computational time and memory used of various smoothing grids

Apart of the computation efficiency, the effect of the smoothing grid also improves the accuracy of the flow solution as shown by the Mach number contours in Fig. 14. The flow field features around the cross section of the EOS body at the stations x/l_{EOS} = 0.25; 0.45; 0.65 and 0.90 and around the wing section of the EOS vehicle at y/s = 0.1 show strong shockwaves generated by the EOS nose and wing. Increasing the grid quality gives

sharper shock wave lines at the above and lower the EOS wing and around the EOS body.

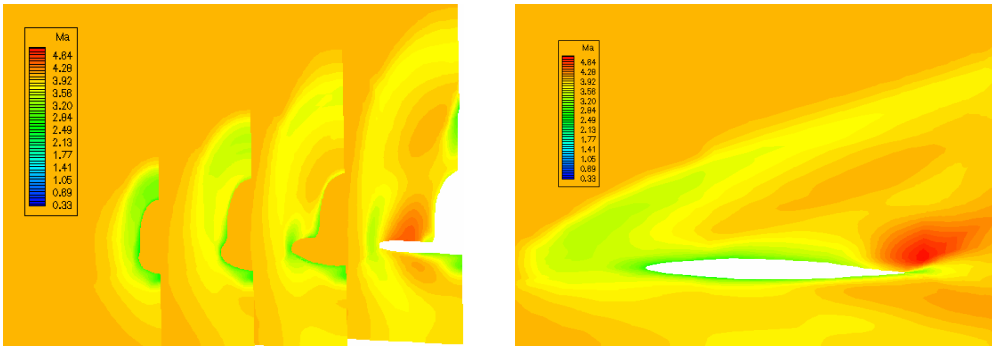

(a). Mach contours around EOS wing and EOS body for case a1

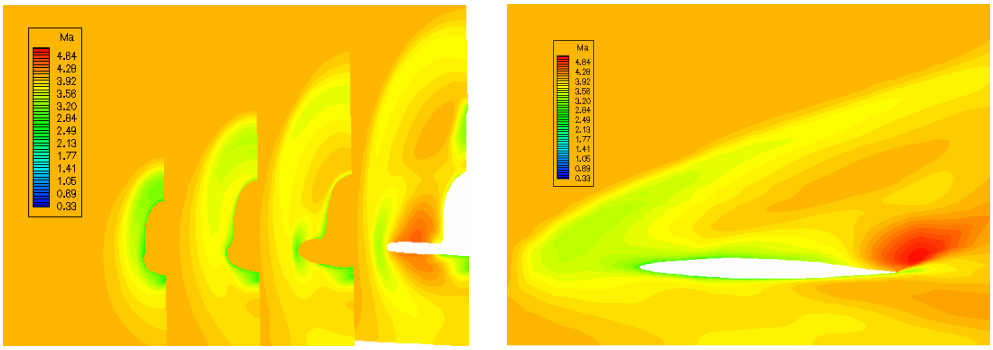

(b). Mach contours around EOS wing and EOS body for case a2

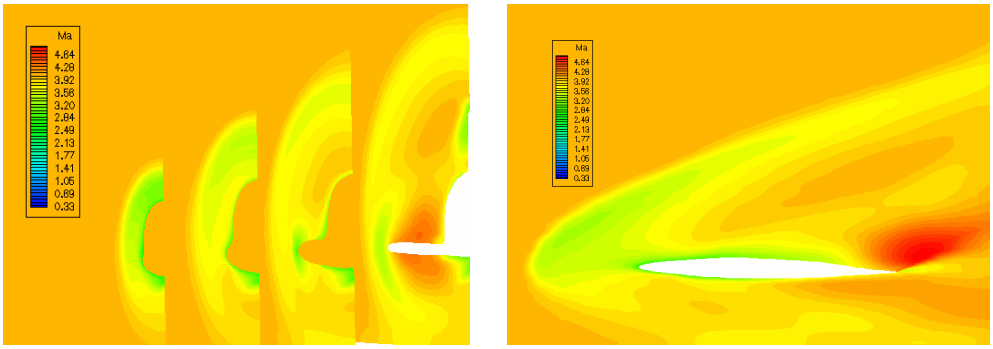

(c). Mach contours around EOS wing and EOS body for case a3

Figure V.14: Mach contours with $\Delta M/M_{\infty} =$ 0.6 for the different smoothed grids at $M_{\infty} = 4.04$, $\Delta\alpha = 0.0°$, $h/l_{EOS} = 0.150$.

Consequently, the higher grid quality provides a more accurate lift coefficient compared to the corresponding experimental data as given in Table V.4. However, the drag coefficients are almost not affected by the grid smoothing. Compared to the experimental data, the computed drag gives about 10% error. This is caused by the strength of the shock wave which is not yet simulated properly due to inadequate grid number and the viscous effects not considered in the flow equation as exhibited by the pressure distribution on the symmetry line of the flat plate in Fig. V.15.

Case	C_L	C_D	C_M
a1 (low smoothing)	-0.00939	0.0269	-0.0107
a2 (quite smoothing)	-0.01070	0.0262	-0.0109
a3 (high smoothing)	-0.01148	0.0264	-0.0110
Experiment	-0.01150	0.0294	-0.0041

Table V.4: The effect of smoothed grids on aerodynamic characteristics.

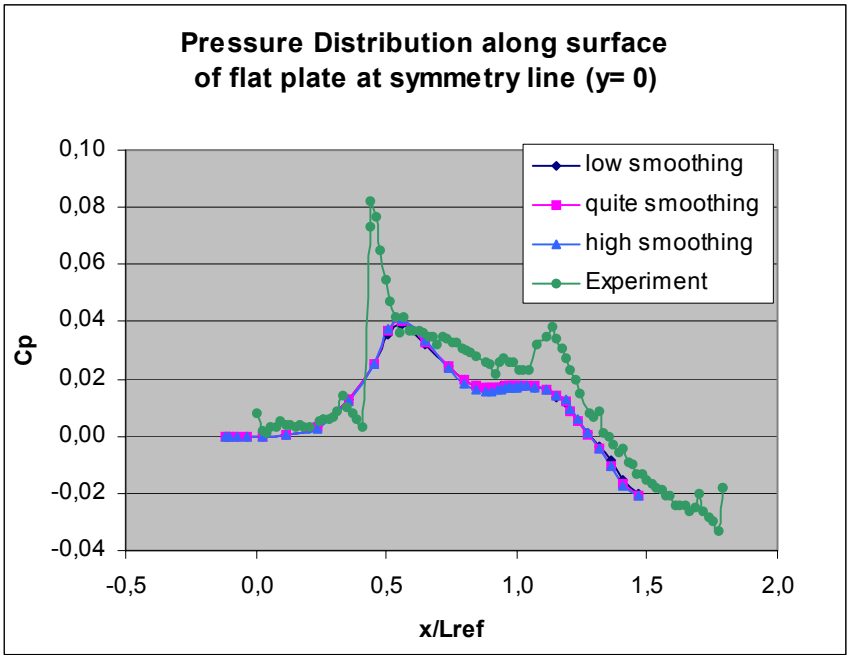

Figure V.15: Pressure coefficient distribution on the symmetry line of the flat plate.

3.2 Effects of Grid Density

As mentioned in the previous section, the gradient of shock waves has not yet be captured properly in the previous simulations due to inadequate grid number along streamwise, particularly in the region where the shock waves occurred. The effects of the grid distribution/density are accomplished by increasing the number of the grids along the EOS body surface. Three computational cases with different grid numbers, namely 113000, 252000, and 493000 for the cases of a2, a4 and a5, respectively are described in detail in Table V.1. The grid results for three different grid number cases are shown in Fig. V.16. Increasing the grid number the distance between two adjacent grids increases, and hence the grid density in the region of interest increases. Figures 17 (a, b, and c) show the density contours at the symmetry line (y/s = 0) and around the cross section of the EOS body at the stations x/l_{EOS} = 0.25; 0.45; 0.65 and 0.90 for the three different grid numbers. Increasing the grid density improves the quality of the bow shock, reflected shock wave, impingement point that they become sharper.

The higher required memory space and the elapse time per iteration due to the increased grid numbers are described in table V.5 for the solution convergence reaching about 1 - 2.0 x 10^{-4}

Case	Time per iteration (seconds)	Memory used	Convergence Limit
a2	10.30	208	$1x10^{-4}$
a4	12.15	256	$2x10^{-4}$
a5	15.06	384	$1x10^{-4}$

Table V.5: Computational time and memory for the different grid densities.

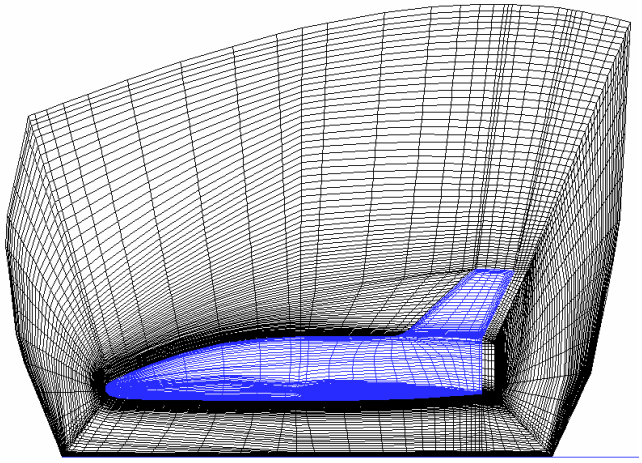

(a). Grid distribution for case a2

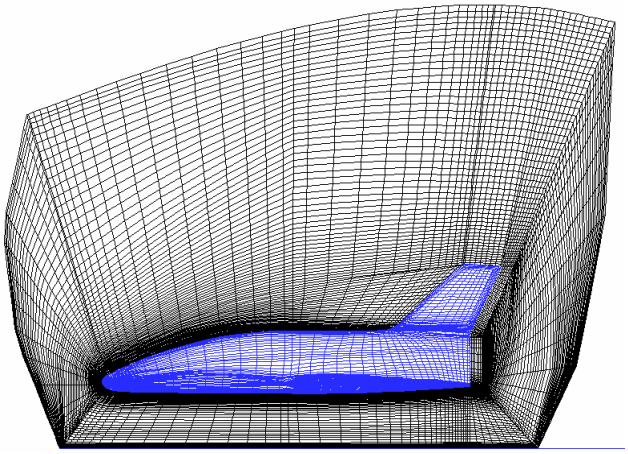

(b). Grid distribution for case a4

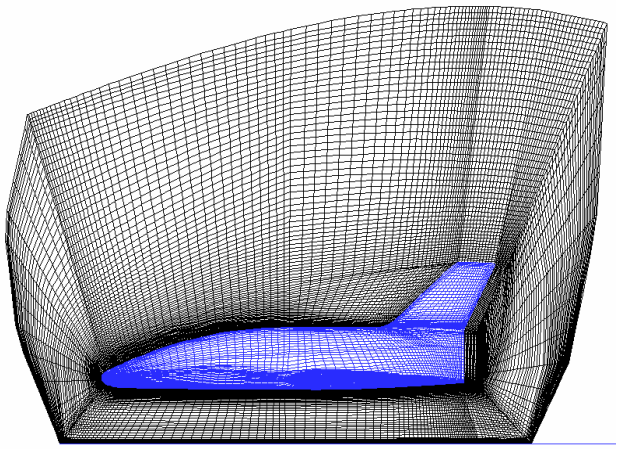

(c). Grid distribution for case a5

Figure V.16: The layouts of three different grid densities.

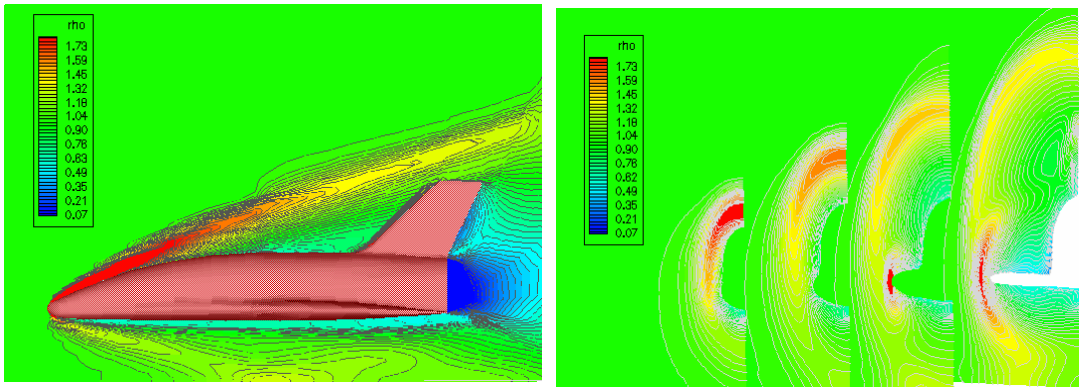

(a). Density contour at symmetry line and EOS body for case a2

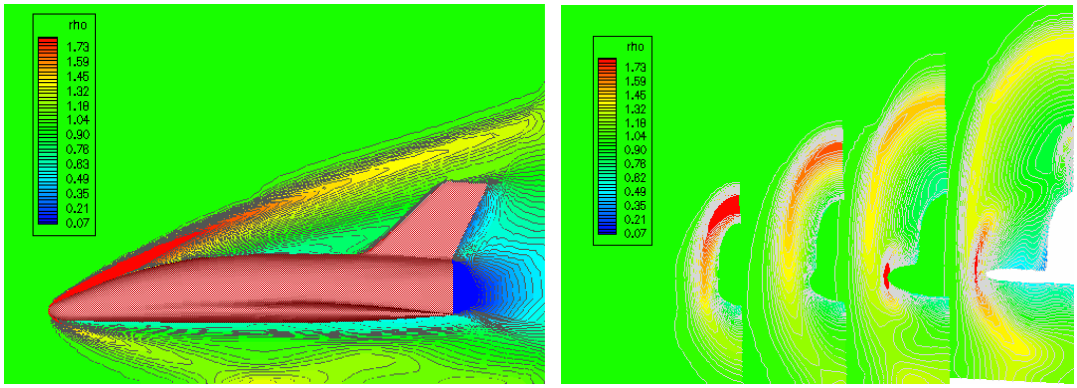

(b). Density contour at symmetry line and EOS body for case a4

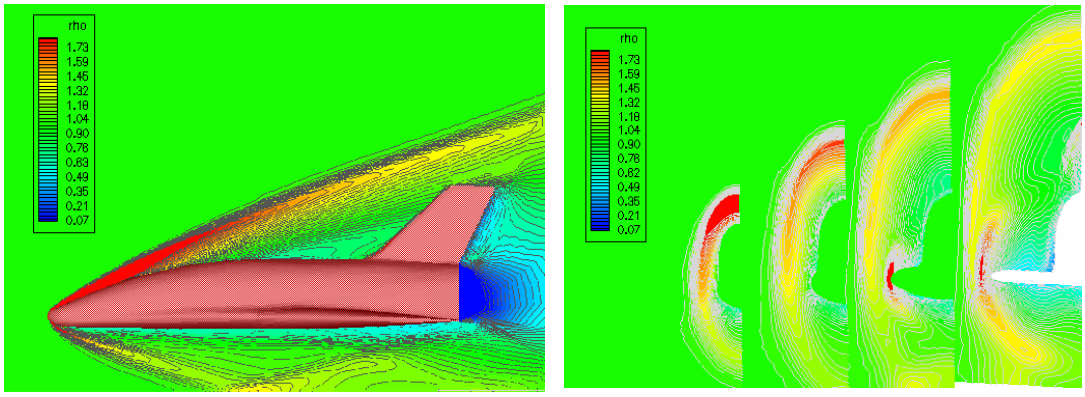

(c). Density contour at symmetry line and EOS body for case a5

Figure V.17: Density contours for the different grid densities at $M_\infty = 4.04$, $\Delta\alpha = 0.0°$, $h/l_{EOS} = 0.150$.

The effects of the higher grid density provides better capturing in the shock waves indicated clearly by the graph of pressure distributions along the symmetry line of the flat plate shown in Fig. V.18. Two peak pressures generated by the shock waves on the flap plate for the case a5 (finer grid) is the closest to the corresponding experiment result, but the second peak pressure behind the base of the experiment can not be captured well for all computational cases.

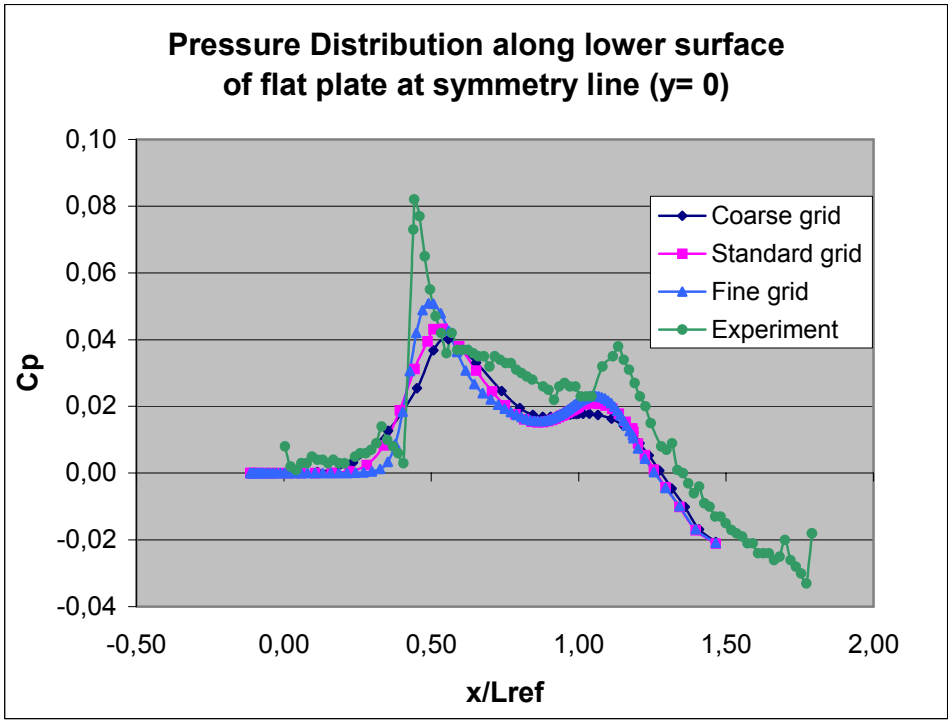

Figure V.18: Pressure coefficient distribution on the symmetry line of the flat plate for three different grid densities.

Table V.6 gives the aerodynamic forces and moment for the three different grid numbers and the corresponding experiment data for reference. The error of lift coefficient of the orbital stage decreases from 7 % to 3 % and the error of the drag coefficient reduces from 11% to 6 % compared to the corresponding experimental data.

Case	C_L	C_D	C_M
a2 (Coarse grid)	-0.01070	0.0262	-0.0109
a4 (Standard grid)	-0.01138	0.0273	-0.0104
a5 (Fine grid)	-0.01180	0.0277	-0.0106
Experiment	-0.01150	0.0294	-0.0041

Table V.6: The effect of grid density on aerodynamic characteristics.

4. Validations

Comparison between the computational results and the corresponding experimental data has been a little bit discussed in the previous section. To perform a more detail validation of the simulation method, comparisons between the numerical results and experimental data are carried out for various conditions of stage separations and the two different model geometries. The validations are performed first using the flat plate and orbital stage EOS for simplifying the effects of aerodynamic interferences between the stages. Then, for the final validation, the flat plate is exchanged with the detailed geometry of the Elliptical Aerodynamic configuration ELAC1C.

4.1 Simplified Configuration

Figure V.19 shows a Schlieren picture and contours of relative density for the EOS angle of attack, $\Delta\alpha$ = 0.0 deg. and the distance between EOS and flat plate, h/l_{EOS} = 0.150 at a free stream Mach number of 4.04, named as the test case of a5. The density contours are recorded in the symmetry plane and plane at the station y/s = 0.1. The relative density is stated as a ratio of the density at a certain point of the flow field to free stream density, ρ/ρ_∞.

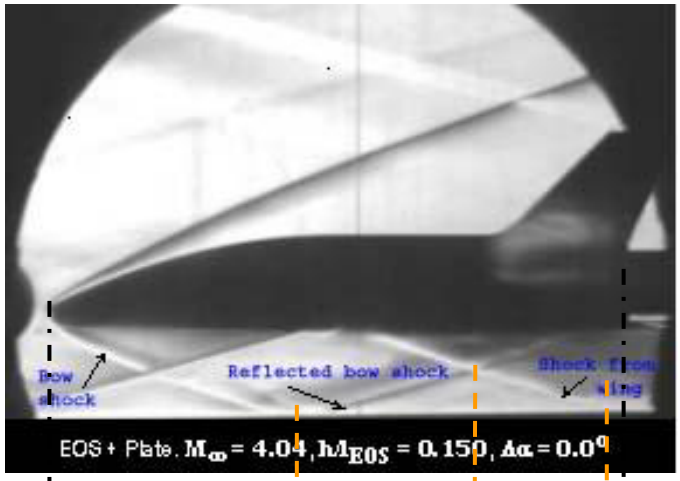

(a). Schlieren Picture

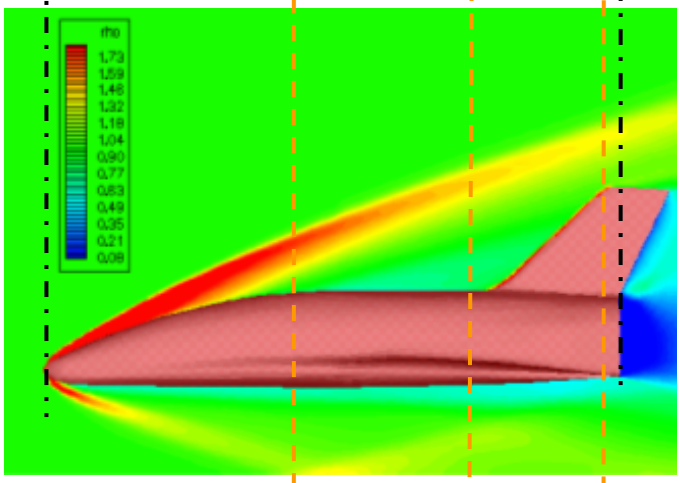

(b). Density contours at symmetry plane

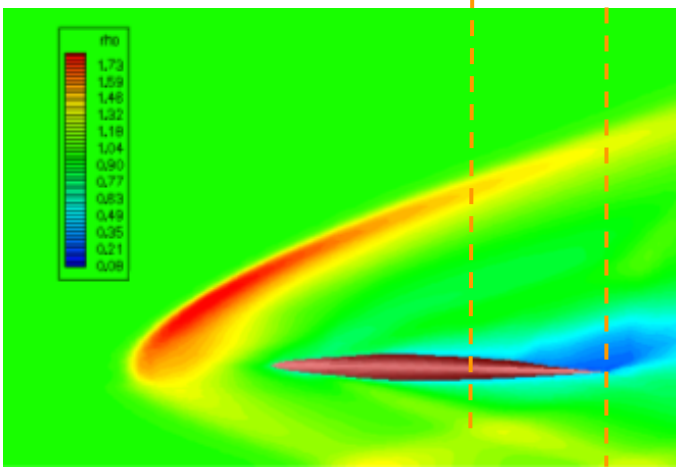

(c). Density contours on plane at station y/s = 0.1

Figure V.19: Comparison between experimental result and numerical computation at $M_\infty = 4.04$, $Re_m = 50.0 \times 10^6$ (experiment), $\Delta\alpha = \Delta\alpha = 0.0°$, $h/l_{EOS} = 0.150$.

It is seen from the Schlieren picture in Fig. 19.a that the bow shock ahead of the blunt nose of the orbital stage is formed. The lower part of the bow shock hits the surface of the flat plate and immediately the shock wave are reflected interacting with the shock wave from the wing leading edge. Subsequently, the reflected shock wave hits the rear part of the EOS vehicle. These phenomena can be captured well in the simulation, namely the present of the EOS bow shock, and the reflected bow shock at symmetry plane shown in the Fig. 19.b and the interaction between the reflected shock wave and the shockwave from the wing shown clearly on the plane at the station of y/s = 0.1 in Fig. 19.c.

However, minor differences appear dealing with quantities of the shock waves such as the bow shock wave angle, locations of the reflected shock wave on the flat plate and the shock interaction. From the numerical computation, the upper bow shock angle above the EOS vehicle depicted on the symmetry plane gives the same value as the experimental result, namely 20.0 deg relative to the horizontal line, but the lower bow shock gives the difference of 1.0 deg. lesser than the experiment. As a result, the location of the computed reflected shock wave and interacted point shifts rearward compared to the experiment. This disparity is also indicated by the static pressure distribution in Fig. V.18. The peak of the computed pressure distribution slightly shifts back compared to the experiment. The calculated pressure peaks caused by the impinging bow shock emanating from the blunt nose of the orbital stage and the wing are weaker compared to the experimental reference data.

For the case at a Mach number of 7.9 with the relative distance h/l_{EOS} = 0.150 and a relative angle of attack of $\Delta\alpha$ = 0.0 deg, the comparison between a Schlieren picture and density contours is depicted in Fig. 20 which the density contours are in the symmetry plane and plane at the station y/s = 0.1

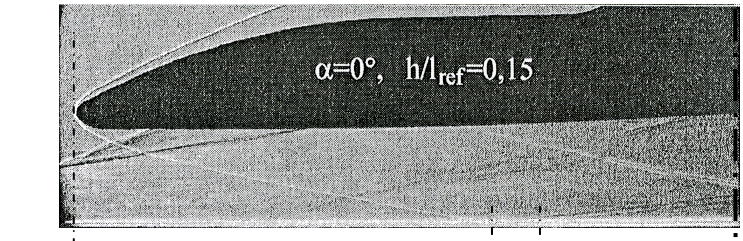

(a). Schlieren Picture

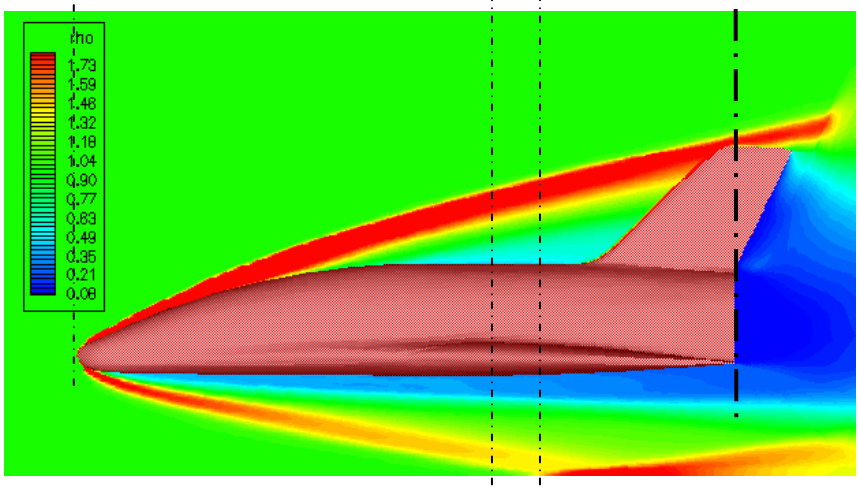

(b). Density contours at symmetry plane

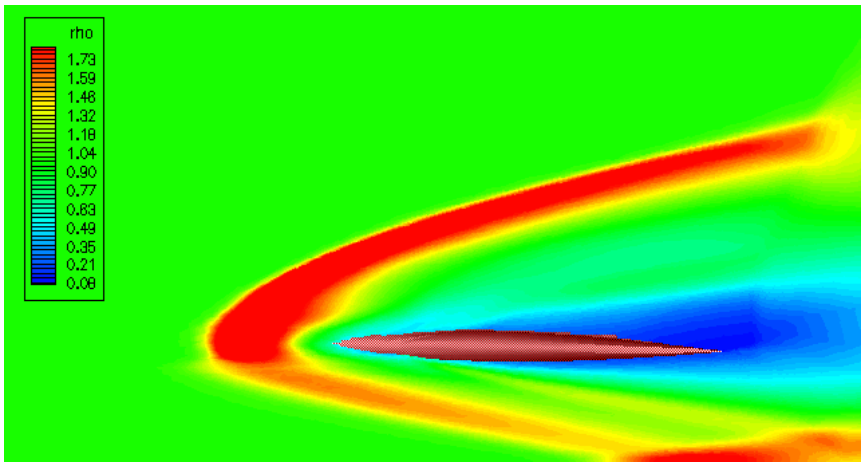

(c). Density contours on plane at station y/s = 0.1

Figure V.20: Comparison between experimental result and numerical computation at $M_\infty = 7.9$, $Re_m = 7.6 \times 10^6$ (experiment), $\Delta\alpha = 0.0°$, $h/l_{EOS} = 0.150$.

At a higher Mach number of $M_\infty = 7.9$, the numerical simulation remains capturing the main flow phenomena such as the EOS bow shock, the reflected bow shock and the shock wave from the wing leading edge with reasonable agreement compared to the experimental results. However, qualitatively, the computed shock wave slightly shifts backward compared to the experiment.

Furthermore, the calculated pressure distribution on the symmetry line provides good agreement compared to the measured pressure distribution as shown in Fig. 21, but approaching the EOS nose, the discrepancy of static pressure coefficient between the experiment and numerical results tend to increase.

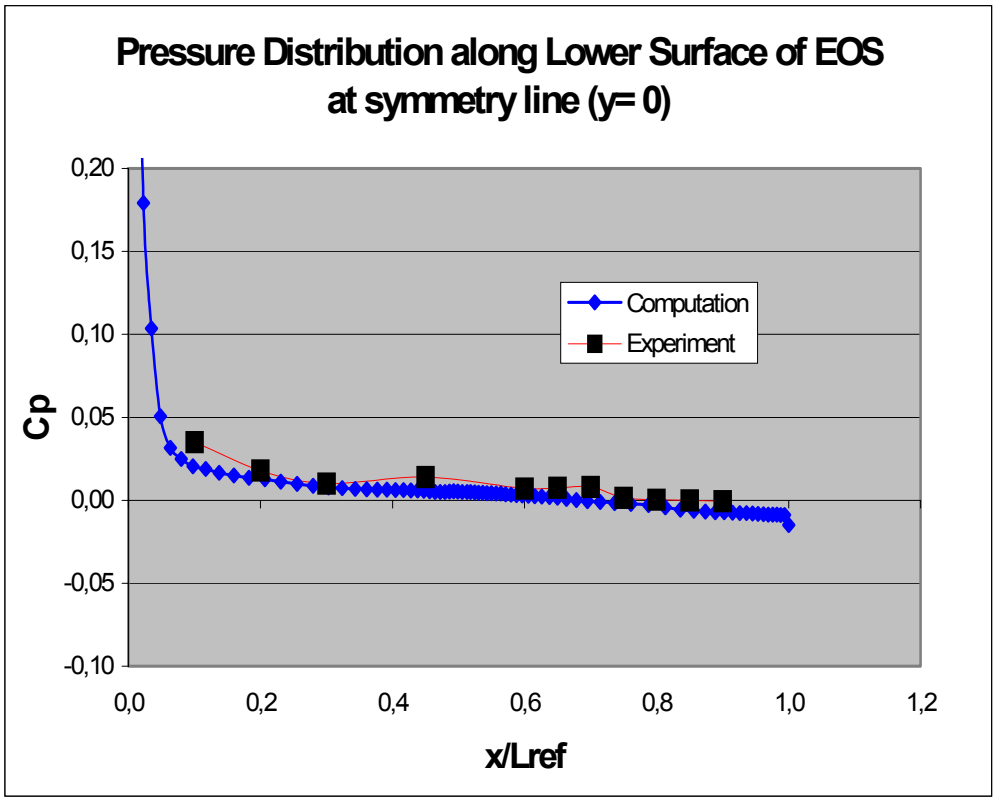

Figure V.21: Pressure coefficient distribution on the symmetry line of the lower surface of the EOS, at $M_\infty = 7.9$, $\Delta\alpha = 0.0°$, $h/l_{EOS} = 0.150$.

The comparison between the measured and computed pressure distributions are also carried out for the stations of x/l_{EOS} = 0.6 and 0.75 of the cross section of the EOS body as shown in Figs V.22 and V.23, respectively (sketched in Fig. V.4). At the cross sections of x/l_{EOS} = 0.6 and x/l_{EOS} = 0.75, the static pressure coefficient on the lower surface of the EOS body at the inboard region does not show a significant change. This pressure then increases gradually from the root to the tip of the EOS lower surface. At the region closer to the outer edge of the EOS swept wing, the flow from the leading edge induces to increase the pressure coefficient abruptly. The computed pressure coefficients give good agreement to the experiment results.

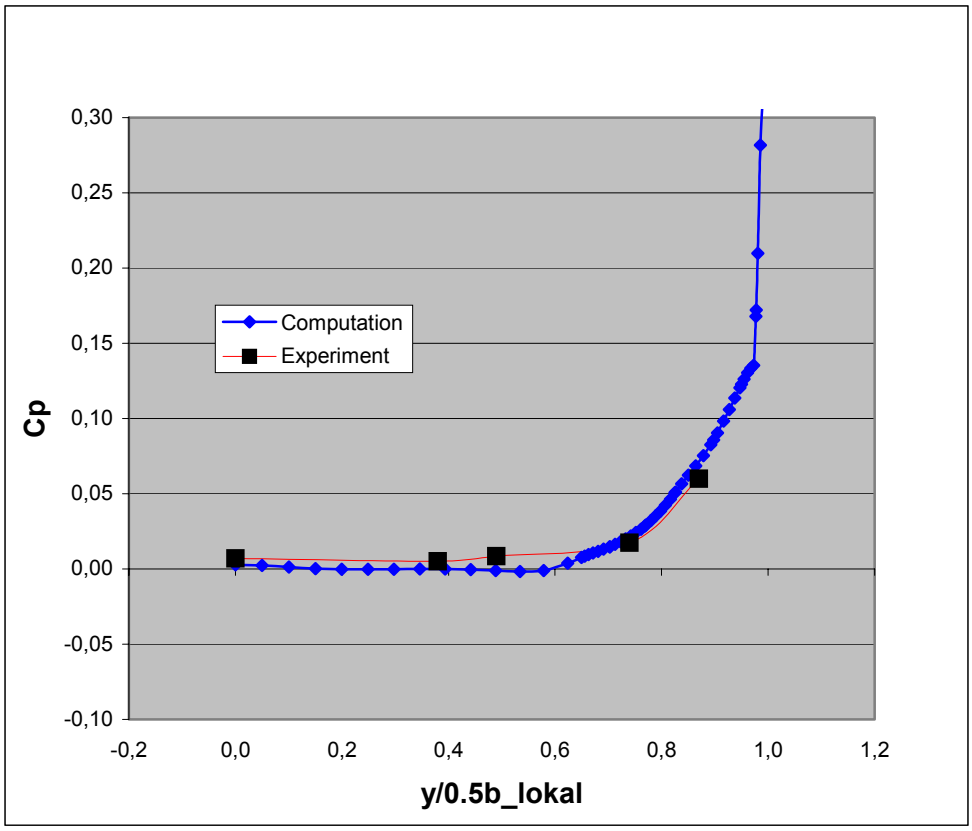

Figure V.22: Pressure coefficient distribution on the cross section of the lower surface at x/l_{EOS} = 0.6, for M_∞ = 7.9, $\Delta\alpha$ = 0.0°, h/l_{EOS} = 0.150.

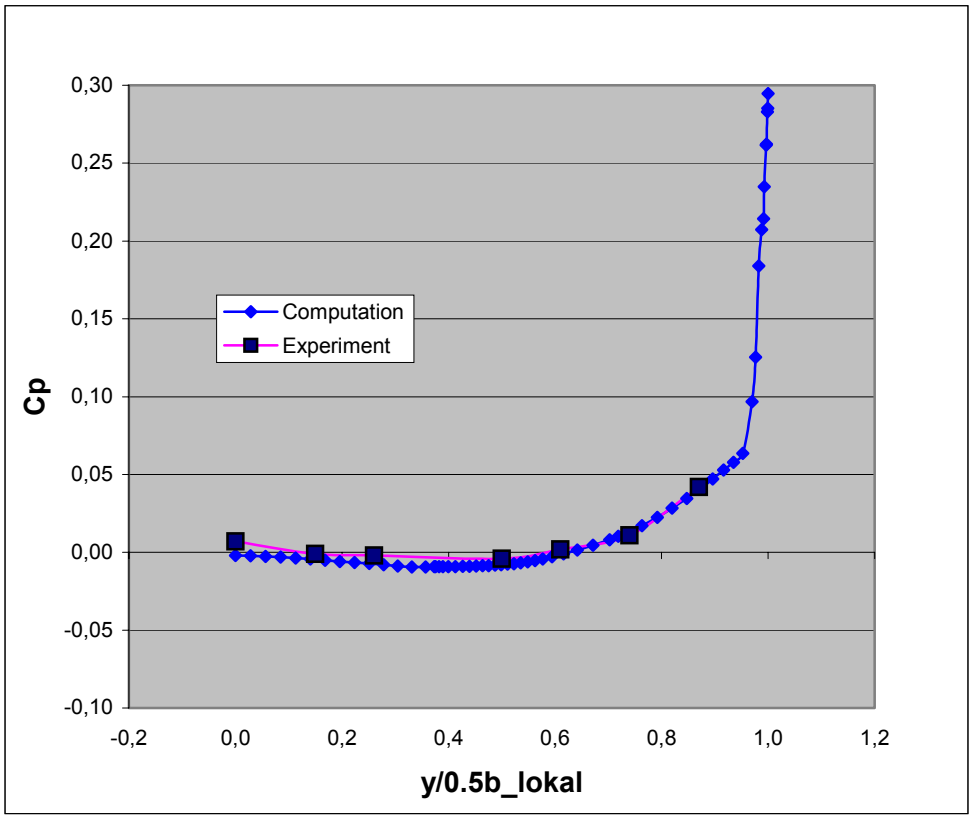

Figure V.23: Pressure coefficient distribution on the cross section of the lower surface at $x/l_{EOS} = 0.75$, for $M_\infty = 7.9$, $\Delta\alpha = 0.0°$, $h/l_{EOS} = 0.150$.

4.2 Fully Two-Stage –to-Orbit Configuration

The presence of the detailed configuration of the carrier stage vehicle ELAC1C provides the increased aerodynamic interferences of the two-stage-to-orbit space transportation system. The flow features occurring typically at strong stage interference are visualized by a Schlieren picture of Fig. V.24. Main effects are marked and numbered from 1 to 8 [11]. Primary factor of the stage interference influencing the orbital stage aerodynamic characteristics are as follows: (i) the carrier bow shock interacting with the orbital stage (1), (ii) the expansion flow and shock wave caused by flow turning at the front of the cavity for the EOS (2, 3), (iii) the orbital shock wave interacting with the expansion and shock waves (6), and it is reflected by the cavity surface and striking again on the orbital stage tail part, (iv) the expansion fan at the inflection of the surface in the lower stage cross section

of maximum thickness affecting the orbital stage tail part at small vertical distance (4).

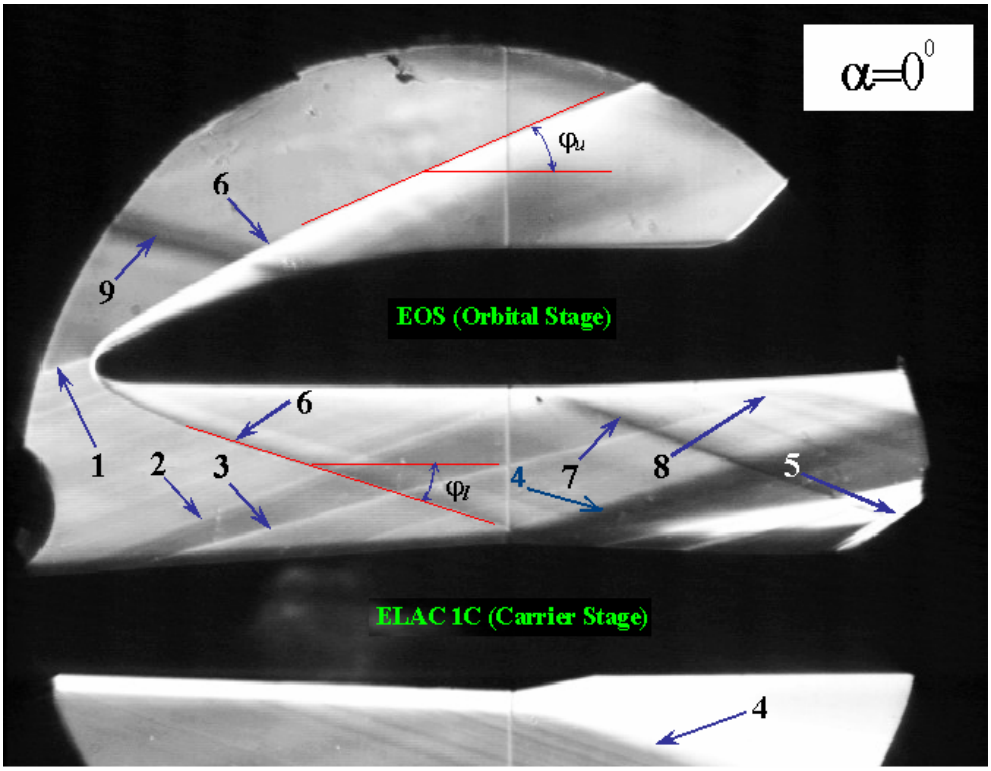

Figure V.24: Schlieren picture of flow features observed in wind tunnel test for the ELAC1C/EOS configuration at $M_\infty = 4.04$, $Re_m = 50.0 \times 10^6$, $\alpha = 0.0°$, $\Delta\alpha = 0.0°$, $h/l_{EOS} = 0.225$;

1. Bow shock wave of ELAC1C.

2. Expansion waves caused by flow turning to the cavity for EOS.

3. Shock wave caused by flow turning along the cavity for EOS.

4. Expansion fan caused by flow turning in the cross section of the maximum thickness of ELAC1C.

5. Shock wave from the fin of EOS.

6. Bow shock wave of EOS.

7. Shock wave from the inflection of the leading edges of EOS wings.

8. Reflected shock waves on lower surface of EOS

9. Weak characteristic from the nozzle/test section joining (it has no effect on interaction of the models).

While, φ_u and φ_l are notations for upper and lower bow shock wave angle of EOS, respectively.

The computational test results corresponding to the above experiment test, namely a free stream Mach number of 4.04 with $\alpha = 0.0\ °$, $\Delta\alpha = 0.0\ °$, and $h/l_{EOS} = 0.150$ are plotted in the relative density contour at the symmetry plane shown in Fig. V.25. The relative density is stated as a ratio of the density at a certain point of the flow field to free stream density, ρ/ρ_∞.

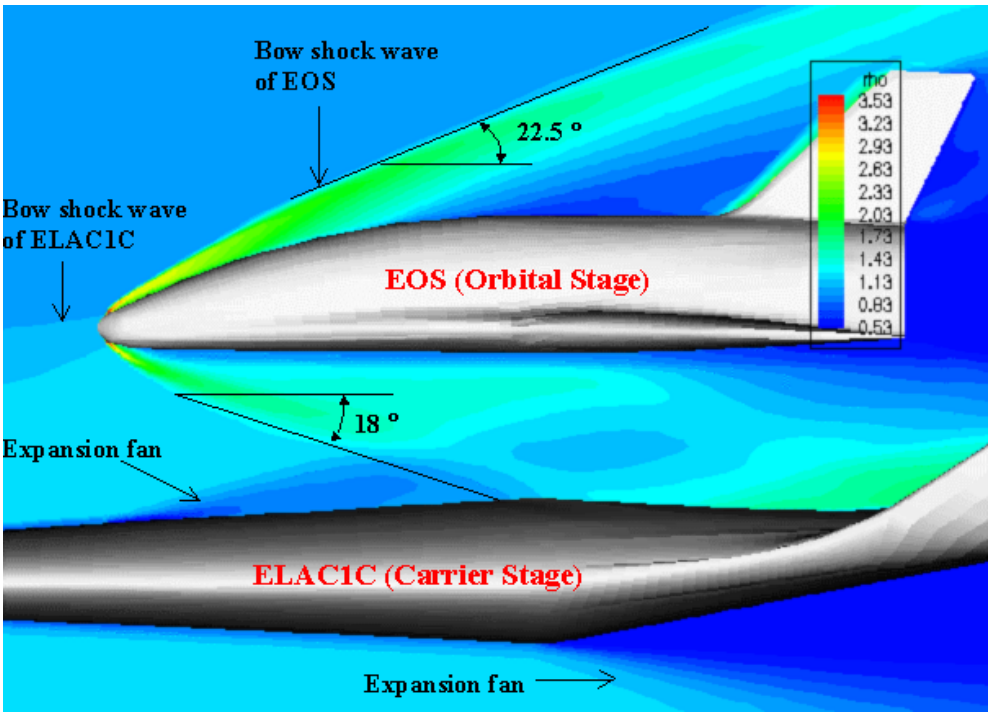

Figure V.25: Density contour for the EOS - ELAC1C configuration at $M_\infty = 4.04$, $\alpha = 0.0°$, $\Delta\alpha = 0.0°$, $h/l_{EOS} = 0.225$ (case b1).

Qualitatively, almost all flow features of the experimental result (Fig. V.24) can be captured in the simulation with reasonable accuracy (Fig.V.25) such as bow shock waves of both the stages, expansion waves, and reflected shock wave. The computation provides a small disparity in the bow shock angle prediction compared to the corresponding experimental results as given in Table V.7.

Concerning the aerodynamic characteristics, Table V.8 provides the results of lift coefficient (C_L), drag coefficient (C_D) and pitch moment coefficient (C_M) for the EOS and ELAC1C vehicles as well as the corresponding

experimental aerodynamic data as the references. The calculated lift coefficient of the carrier stage give more satisfactory agreement to the experiment results than that of the orbital stage. The less prediction of the EOS lift coefficient is caused that the simulation of the bow shock wave of the EOS does not yet capture properly indicated by the error of the bow shock angle about 1.0 deg. With such errors given in Table V.7, the EOS lower surface experiences lower pressure flow and the EOS upper surface subjecting to higher pressure flow, hence the lift coefficient of EOS is less predicted. This may be also caused by the lack of grid number in the gap region where the complex aerodynamic interferences occurred.

Angle of bow shock wave	Experimental (deg.)	Computational (deg.)	Error (deg.)
For test case b1 • upper bow shock angle, φ_u • lower bow shock angle, φ_l	 23.0 17.0	 22.5 18.0	 (-) 0.5 (+) 1.0

Table V.7: Comparison of the bow shock wave angle between numerical computation and the corresponding experimental result for the test case b1.

Aero Char.	Orbital Stage (EOS)		Carrier Stage (ELAC1C)	
	Comp	Exp	Comp	Exp
C_L	0.0292	0.0366	-0.0504	-0.0491
C_D	0.0293	0.0337	0.0133	0.0164
C_M	-0.0073	-0.0072	0.0077	0.0089

Table V.8 Aerodynamic characteristics of the EOS and ELAC1C at M_∞ =4.04, Re_m = 50.0 x 10^6 (experiment), α= 0.0 °, $\Delta\alpha$ = 0.0 °, h/l_{EOS} = 0.225 (case b1).

The second validation of the numerical simulation of the two stage EOS - ELAC1C vehicle system are also performed by considering different orbital stage angles of attack. Figure V.26 depicts the flow pattern obtained for a free stream Mach number of M_∞ = 4.04, an orbital stage angle of attack of

$\Delta\alpha$ = 2.0 °, and the distance between the orbital stage and the carrier stage of h/l_{EOS} = 0.225. In addition, the experimental data are obtained at a Reynolds number of Re_m = 50.0 x 10^6, and the numerical results assume that flow is inviscid.

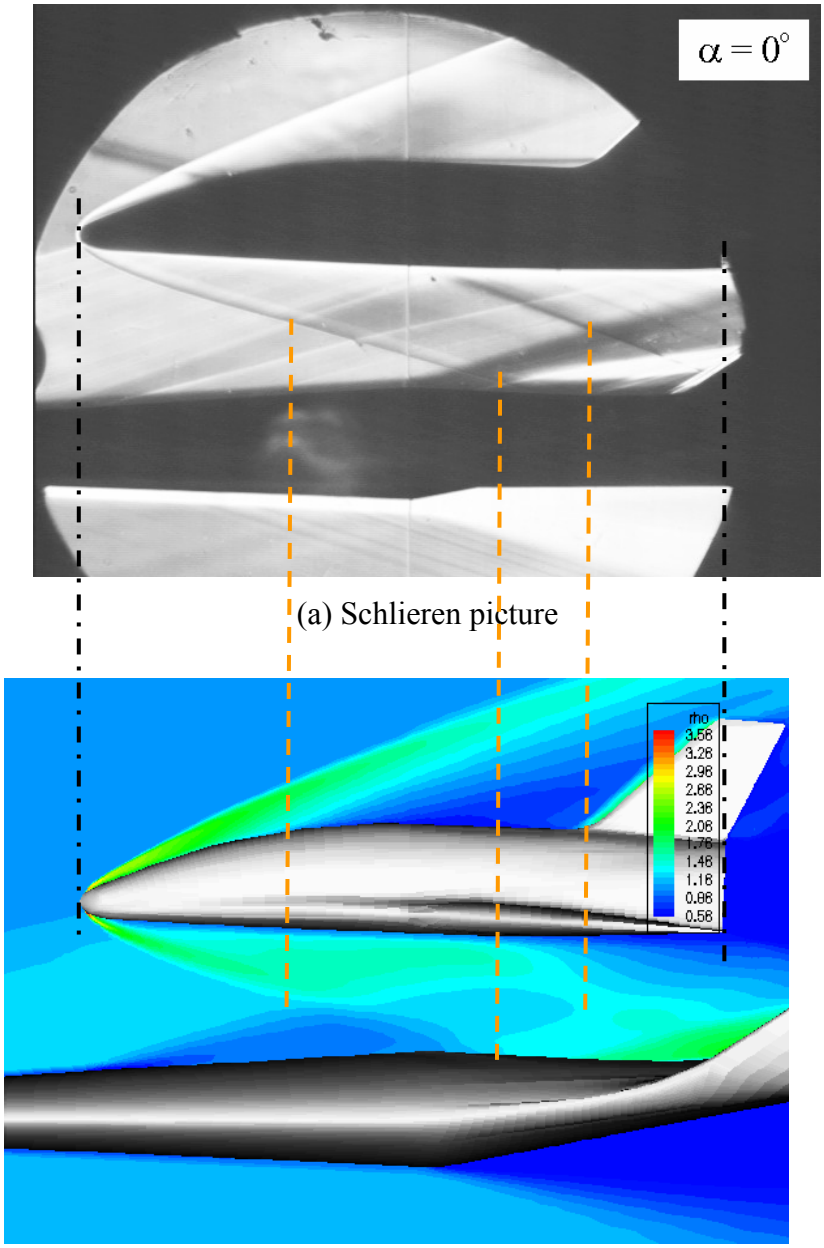

(a) Schlieren picture

(b) Relative density contours

Figure V.26: Density contour for the EOS - ELAC1C configuration at M_∞ = 4.04, Re_m = 50.0 x 10^6 (experiment), α = 0.0°, $\Delta\alpha$ = 2.0°, h/l_{EOS} = 0.225 (case b3).

From Fig. V.26 the comparison between the Schlieren picture of the experiment and the calculated density distribution of the symmetry plane shows a very good agreement for the bow shocks of the EOS and ELAC1C, the point interaction between the EOS bow shock and expansion fan as well as the point of shock reflection on the carrier stage cavity middle part. A good comparison between numerical and experimental result is also indicated by the maximum error of the bow shock angle about 0.5 deg as given in Table V.9.

angle of bow shock wave	Experimental (deg.)	Computational (deg.)	Error (deg.)
For test case b3			
• upper bow shock angle, φ_u	22.0	21.5	(-) 0.5
• lower bow shock angle, φ_l	16.0	16.5	(+) 0.5

Table V.9: Comparison of the bow shock wave angle between numerical computation and the corresponding experimental results for the test case b3.

Further, Table V.10 shows that the aerodynamic characteristics of the computation for the moderate orbital stage angle of attack are agreeably to the experimental results. Similar to the case b1, the lift coefficient of the carrier stage gives more satisfactory agreement to the experiment results than that of the orbital stage.

Aero Char.	Orbital Stage (EOS)		Carrier Stage (ELAC1C)	
	Comp	Exp	Comp	Exp
C_L	0.0626	0.0747	-0.0556	-0.0538
C_D	0.0322	0.0326	0.0131	0.0164
C_M	-0.0147	-0.0069	0.0086	0.0105

Table V.10 Aerodynamic characteristics of the EOS and ELAC1C at M_∞ =4.04, Re_m = 50.0 x 10^6 (experiment), $\alpha = 0.0°$, $\Delta\alpha = 2.0°$, $h/l_{EOS} = 0.225$ (case b3).

The last validation of numerical simulation for the fully two-stage configuration is performed at a larger separation distance, namely $h/l_{EOS} = 0.325$. Comparison of numerical and experimental results is exhibited with the Schlieren picture and density contour in Fig. 27.

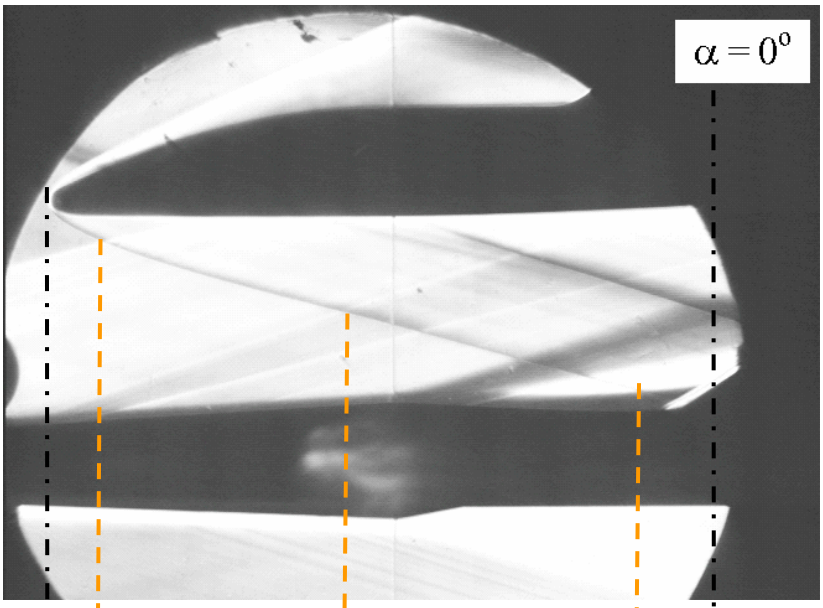

(a) Schlieren picture

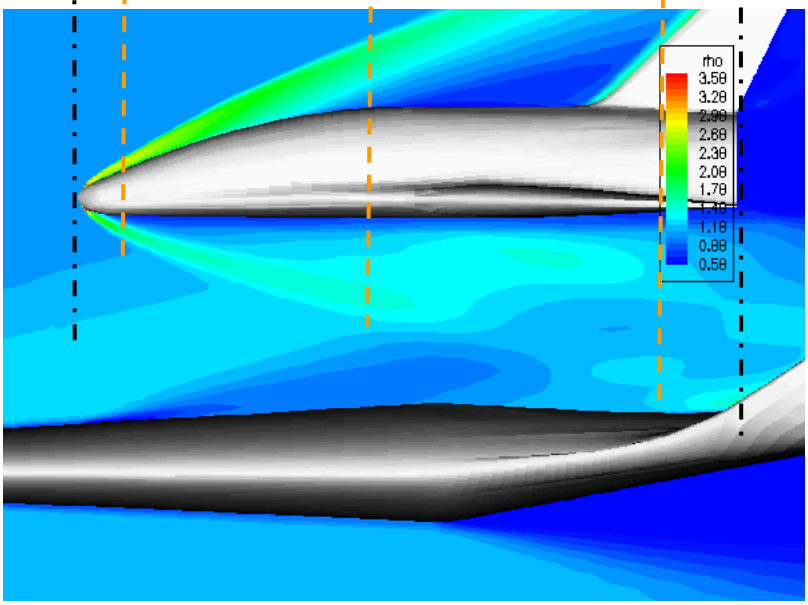

(b) Relative density contours

Figure V.27: Density contour for the EOS - ELAC1C configuration at $M_\infty = 4.04$, $Re_m = 50.0 \times 10^6$ (experiment), $\alpha = 0.0°$, $\Delta\alpha = 0.0°$, $h/l_{EOS} = 0.325$ (case b5).

Most flow features showing in the Schlieren picture can be captured well in the numerical simulation, except in the rear part of the gap region. With the larger gap area the bow shock wave of the ELAC1C interacts with a lower part of the EOS bow shock wave. The EOS bow shock wave itself interacts with the expansion fan and shockwave generated by the curvature of the ELAC1C cavity at the middle gap region. Then, it goes through flow field in the gap region and strikes on the rear part of the ELAC1C as depicted in the Schlieren picture, but it not clearly captured in the simulation.

The upper and lower bow shock angles for the test case b5 are given in Table V.11. The computational results of both the bow shock wave angles agree to the experimental data with an error of no more than 0.5 deg. Table V.12 gives a comparison between the computed and measured aerodynamic characteristics for the EOS and ELAC1C. For all aerodynamic characteristics the comparison between the computational and experimental results shows a good consistence.

angle of bow shock wave	Experimental (deg.)	Computational (deg.)	Error (deg.)
For test case b5			
• upper bow shock angle, φ_u	22.5	23.0	(+) 0.5
• lower bow shock angle, φ_l	15.0	15.5	(+) 0.5

Table V.11: Comparison of the bow shock wave angle between numerical computation and the corresponding experimental result for test case b5.

Aero Char.	Orbital Stage (EOS)		Carrier Stage (ELAC1C)	
	Comp	Exp	Comp	Exp
C_L	0.0225	0.0332	-0.0439	-0.0394
C_D	0.0287	0.0317	0.0130	0.0164
C_M	-0.0161	-0.0137	0.0057	0.0062

Table V.12 Aerodynamic characteristics of EOS and ELAC1C at $M_\infty = 4.04$, $Re_m = 50.0 \times 10^6$ (experiment), $\alpha = 0.0\ °$, $\Delta\alpha = 0.0\ °$, $h/l_{EOS} = 0.325$.

5. Detailed analysis of Quasy Steady Stage Separation of TSTO vehicle system

The simulation of the quasy-steady stage separation of the TSTO space transportation system is performed by placing the orbital stage at different vertical positions, h/l_{EOS} as well as at different angles of attack $\Delta\alpha$ relative to the carrier stage.

The effects of "separation" parameters, including the separation distance between the stages, orbital stage angle of attack as well as Mach number, on flow behaviour and aerodynamic characteristics of the TSTO space transportation system are investigated on the configurations of the EOS - flat plate and EOS - ELAC1C.

5.1 Flat Plate/ EOS Configuration

5.1.1 Effects of Orbital Stage Position

The effects of the orbital position relative to the flat plate on flow field and aerodynamic performance are studied by choosing three different positions with varying in relative distance (h/l_{EOS}) and relative angle of attack ($\Delta\alpha$) called as cases a2, a6 and a7 with their details shown in Table V.1.

Figure V.28 shows three density contours of the symmetry plane for two different separation distances and two orbital angles of attack at a free stream Mach number of 4.04. With increasing separation distance showing in Figs V.28 (a) and (b) the bow shock wave hits the flat plate at further downstream. This also causes the interaction between the reflected shockwave and shock wave of the inflection point of the leading edge of EOS wings occurs at a further rear in the gap region. At the larger separation distance, both the shock waves moves through the rear gap region, one then hits a more rear part of the flat plate and the other subjects to the wake zone of the orbital stage.

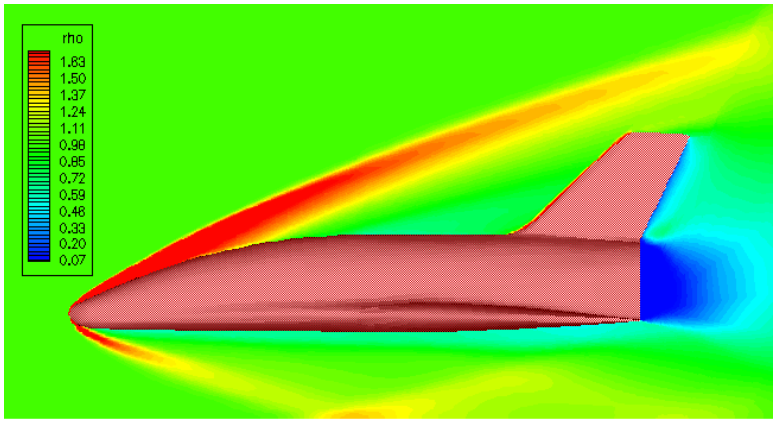

(a). Density contour at symmetry plane for case a2

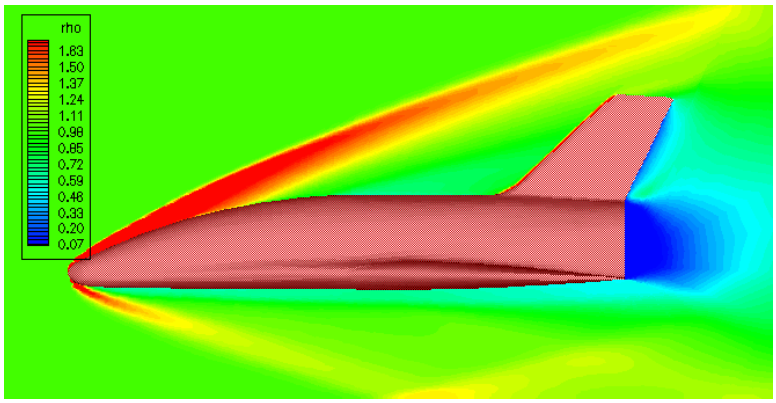

(b). Density contour at symmetry plane for case a6

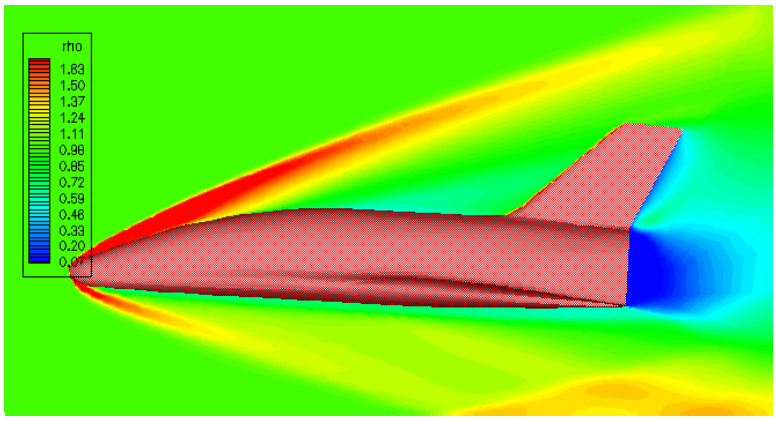

(c). Density contour at symmetry plane for case a7

Figure V.28: Comparison of density contours for three different EOS positions: (a) $M_\infty = 4.04$, $\Delta\alpha = 0.0°$, $h/l_{EOS} = 0.150$; (b) $M_\infty = 4.04$, $\Delta\alpha=0.0°$, $h/l_{EOS} = 0.225$; (c) $M_\infty = 4.04$, $\Delta\alpha = 3.0°$, $h/l_{EOS} = 0.225$.

Concerning the orbital angle of attack change as exhibited in Figs. V.28 (b) and (c), the reflected shock point on the flat plate shifts downstream. A decrease in the area of the rear gap region causes the stronger interaction between the reflected shockwave and shock wave from the EOS wings. The second inflection point on the flat plate gives the stronger hit by the shock wave from the wings at higher orbital angle of attack.

On the flat plate, discontinuous pressures due to the shock waves occur in two locations. Figure V.29 shows the static pressure distribution on the flat plate for the three different cases, i.e. cases a2, a6 and a7.

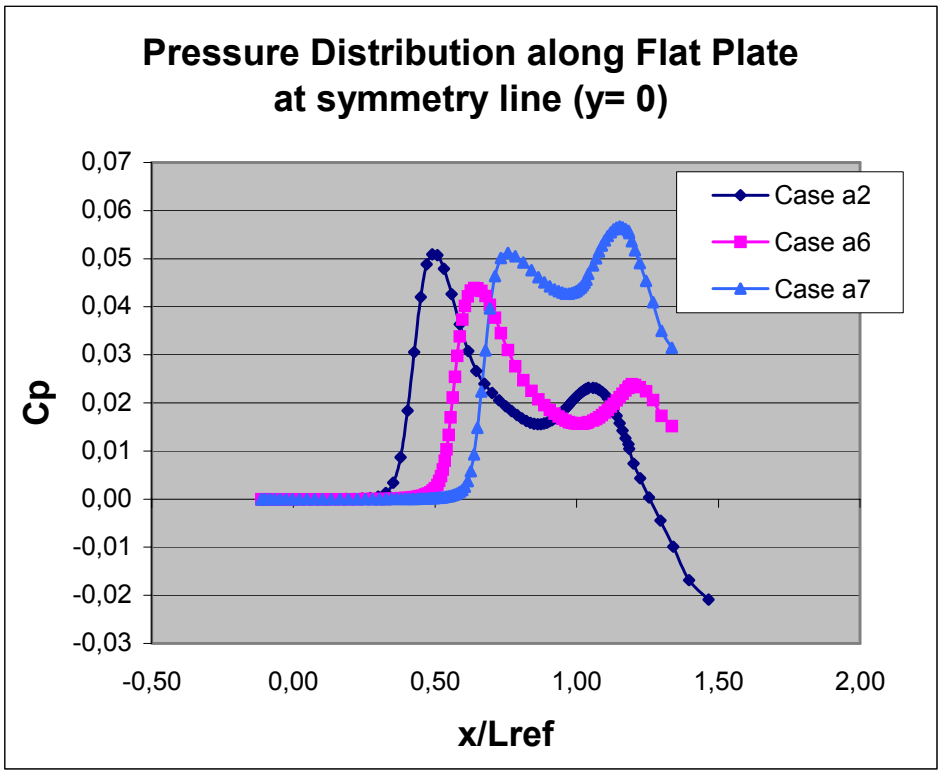

Figure V.29: Pressure coefficient distribution on the symmetry line of the flat plate for three different EOS positions: $M_\infty = 4.04$, $\Delta\alpha = 0.0°$, $h/l_{EOS} = 0.150$ (case a2); $M_\infty = 4.04$, $\Delta\alpha = 0.0°$, $h/l_{EOS} = 0.225$ (case a6); $M_\infty = 4.04$, $\Delta\alpha = 3.0°$, $h/l_{EOS} = 0.225$ (case a7).

Increasing the separation distance shown by cases a2 and a6, the level of the pressure peaks indicates that the bow shock subjecting to the first inflection point on the flat plate with its shock strength decreases, but that at the second inflection point due to the shock from the wing slightly increases. While, increasing the orbital angle of attack shown by cases a6 and a7 does not give a significant change in the peak pressure at the first inflection point, but the strength of shock waves generated by the nose and wing of EOS at the second inflection point increases.

Figure V.30 shows three contours of Mach number in 3-D view for two different separation distances and two angles of attack of the orbital EOS. The spreading of the shock waves occurs in the flat plate and symmetry plane as well as in the plane located behind the orbital. In the region where the shock wave occurred and in the base, a Mach number of the flow decreases. With increasing the separation distance as shown in Fig. 30 (a and b) the gap area increase, hence flow velocity in the gap region slightly increases. This gives a suction effect on the orbital stage and flat plate influencing on aerodynamic performance of the orbital stage. Contrarily, an increase of the orbital stage angle of attack as shown in Fig. 30, the gap area decreases along downstream and the flow in the rear region of the gap subjects to a contraction. For a supersonic flow, the reduction of the gap area results a decrease in flow velocity, hence pressures in the rear part of the gap area increases.

Shown in Table V.13 the effects of the increased separation distance provides a decrease in the EOS lift coefficient and pitching moment coefficient and a slightly increase in the drag coefficient. While, increasing the orbital stage angle of attack results a higher increase in the EOS lift coefficient and drag coefficient, also the pitching moment coefficient becomes more negative. From the result in Table V.13, the separation of the orbital stage will gain a positive lift coefficient when the initial position of the orbital stage has a positive angle of attack.

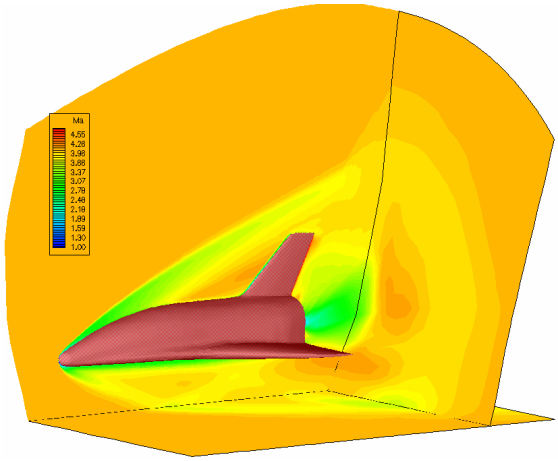

(a). Mach contour in 3D view for case a2

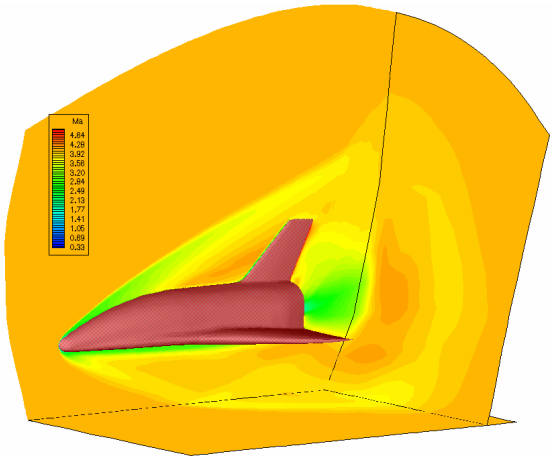

(b). Mach contour in 3D view for case a6

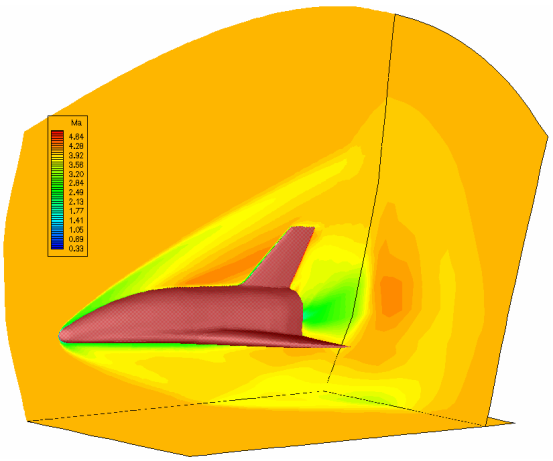

(c). Mach contour in 3D view for case a7

Figure V.30: Comparison of Mach number contours for three different EOS positions: (a) $M_\infty = 4.04$, $\Delta\alpha = 0.0°$, $h/l_{EOS} = 0.150$; (b) $M_\infty = 4.04$, $\Delta\alpha = 0.0°$, $h/l_{EOS} = 0.225$; (c) $M_\infty = 4.04$, $\Delta\alpha = 3.0°$, $h/l_{EOS} = 0.225$.

The experimental data as the references are also given in Table V.13. Comparing to the experimental results, the computed lift coefficient gives a very good agreement for the cases with the zero relative angle of attack with the error varying from 3 to 5 %, but for the case with a positive orbital angle of attack the error of the computed lift coefficient increases to become about 10 %. The computed drag coefficient results does not signicantly change due to the alterations of the separation distance and angle of attack of the orbital stage. The computed drag coefficients agree with the experimental results with the error in the range of 5 to 7 %.

Case	C_L		C_D		C_M	
	comp	Exp	Comp	Exp	comp	Exp
a2	-0.0118	-0.0115	0.0277	0.0294	-0.0106	-0.0041
a6	-0.0127	-0.0120	0.0277	0.0299	-0.0084	-0.0059
a7	0.0263	0.0293	0.0283	0.0304	-0.0071	-0.0062

Table V.13: Comparison of aerodynamic characteristics for three different EOS positions between the computation and corresponding experimental results.

5.1.2 Effects of Mach number

The two-stage space transportation system was designed to separate with Mach number of 6.8. No available experiment data is produced at this Mach number. However, there are experimental data tested at Mach numbers of 4.04 and 7.9 that have been used to validate this simulation method as already discussed at section 4 in this chapter. The numerical computation at a free stream Mach number of 6.8 is carried out and it will be compared to the numerical results at Mach numbers of 4.04 and 7.9. From this, the effects of the Mach number variation on the flow field and aerodynamic characteristics can be studied. These computations are stated as the computational cases a2, a8 and a9 that described detail in Table V.1.

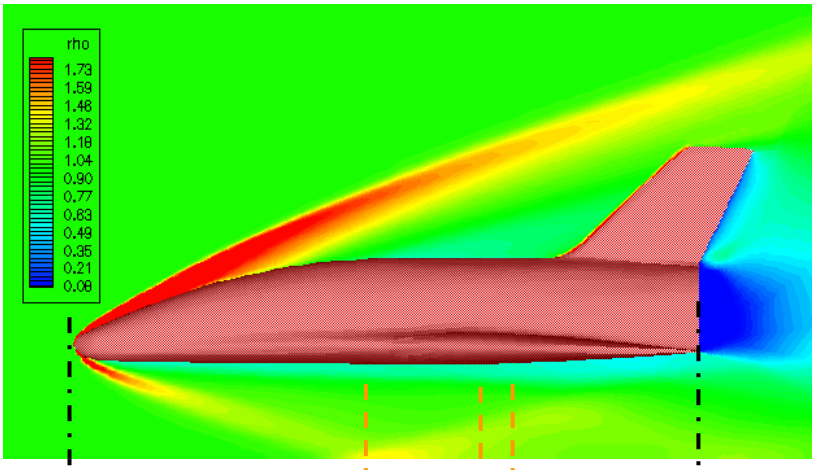

(a). Density contour at symmetry plane for case a2

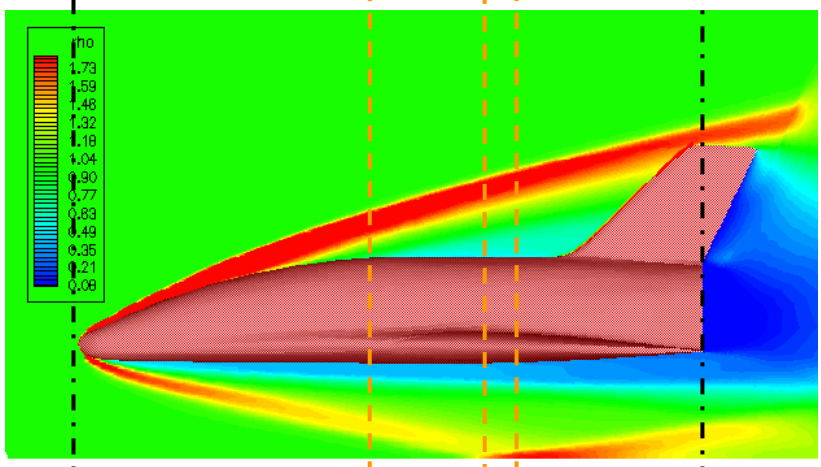

(b). Density contour at symmetry plane for case a8

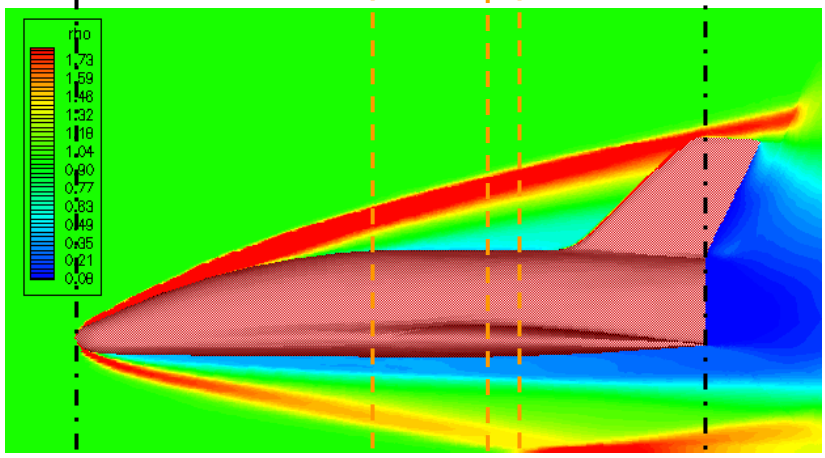

(c). Density contour at symmetry plane for case a9

Figure V.31: Comparison of density contours for three different EOS positions: (a) $M_\infty = 4.04$, $\Delta\alpha = 0.0°$, $h/l_{EOS} = 0.150$; (b) $M_\infty = 6.8$, $\Delta\alpha = 0.0$ °, $h/l_{EOS} = 0.150$; (c) $M_\infty = 7.9$, $\Delta\alpha = 0.0°$, $h/l_{EOS} = 0.150$.

Figure V.31 shows the density distributions on the symmetry plane for the three different Mach numbers with the same orbital stage position relative to the flat plate. To be able make the comparison of the three different cases the density distribution are set in the same values of the upper and lower limits. Increasing Mach number the bow shock angle occurred on above and below of the EOS body surface decreases. The lower part of the bow shock hits the flat plate with the inflection point shifting downward with increasing Mach number. Also, the strength of the shock wave decrease with increasing Mach number. This is indicated by a decrease of pressure peak at symmetry plane of the flat plate with the Mach number increase as shown in Fig. 32.

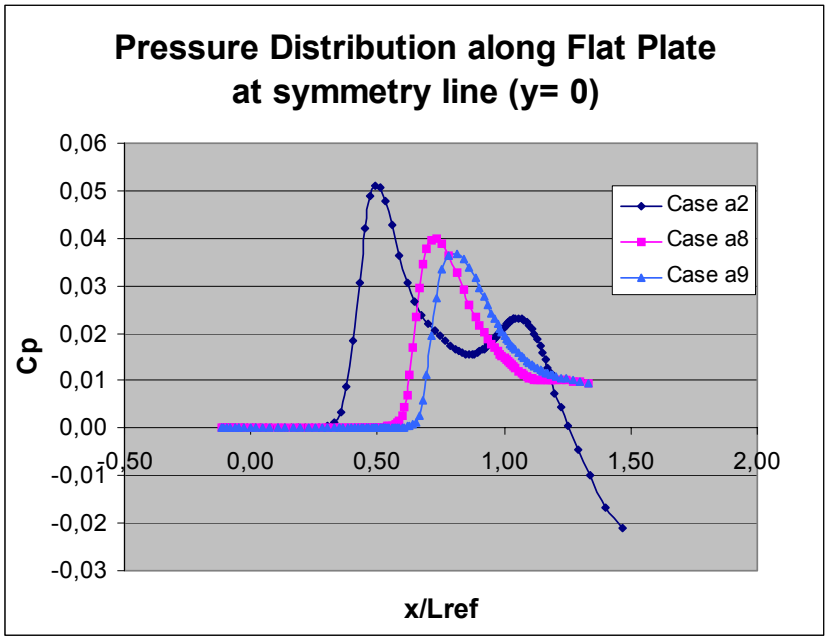

Figure V.32: Pressure coefficient distribution on the symmetry line of the flat plate for three different Mach numbers with the orbital position, $\Delta\alpha = 0.0°$, $h/l_{EOS} = 0.150$: $M_\infty = 4.04$ (case a2), $M_\infty = 6.8$ (case a8) and $M_\infty = 7.9$ (case a9).

Furthermore, the density distributions in the z-plane for the three different Mach numbers are depicted in Fig. V.33. At the Mach number of 4.04, the bow shock wave interacts with the shock wave from the wing in the rear location. With increasing Mach number, interaction points of the bow shock wave and the shock wave generated by the EOS swept wing shifting forward at the leading edge of the EOS swept wing.

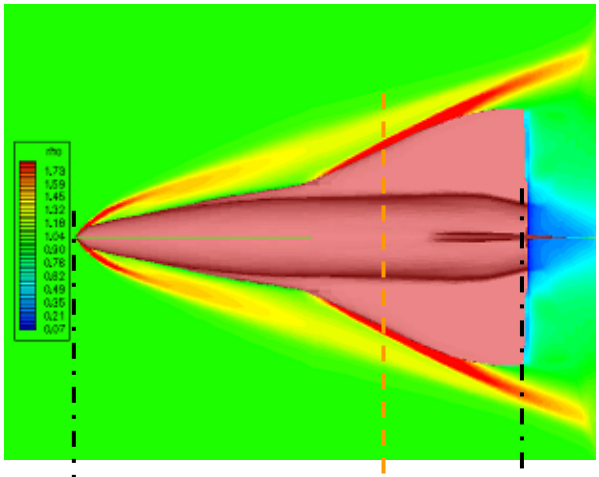

(a). Density contour at z-plane for case a2

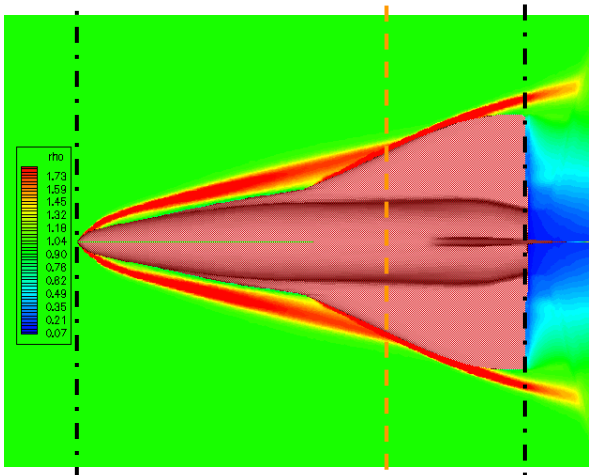

(b). Density contour at z-plane for case a8

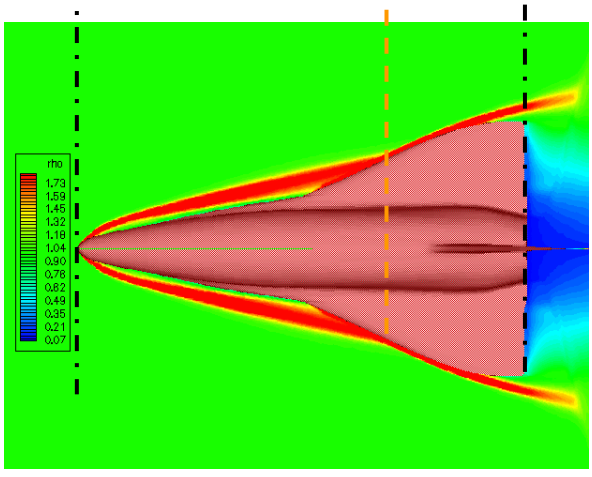

(c). Density contour at z-plane for case a9

Figure V.33: Comparison of density contours at z-plane for three different Mach numbers: (a) $M_\infty = 4.04$, $\Delta\alpha = 0.0°$, $h/l_{EOS} = 0.150$; (b) $M_\infty = 6.8$, $\Delta\alpha = 0.0°$, $h/l_{EOS} = 0.150$; (c) $M_\infty = 7.9$, $\Delta\alpha = 0.0°$, $h/l_{EOS} = 0.150$.

Table V.14 shows lift, drag and pitching moment coefficients of the EOS for the three different Mach numbers. With increasing Mach number, the lift coefficient becomes more negative. This indicates the separation at higher Mach number requires more pay attention because the interaction between the orbital stage and flat plate gives more dangerous. The drag coefficient decreases with increasing Mach number. The Mach line angle generated by the bow shock decreses with increasing Mach number, hence the strength of the shock wave and wave drag decreases. Concerning the pitching moment, the magnitude of the pitching moment coefficient decreases with increasing Mach number.

Case	C_L	C_D	C_M
a2 (Mach = 4.04)	-0.01180	0.0277	-0.0106
a8 (Mach = 6.80)	-0.01540	0.0222	-0.0093
a9 (Mach = 7.90)	-0.01541	0.0213	-0.0091

Table V.14 Comparison of aerodynamic characteristics for three cases with difference in Mach number at the orbital position $\Delta\alpha = 0.0°$, $h/l_{EOS} = 0.150$.

5.2 ELAC1C/ EOS Configuration

5.2.1 Effects of Angle of Attack of Carrier Stage

The separation may occur at a certain angle of attack of the carrier stage instead of zero angle of attack. Related to this, the effect of angle of attack of the carrier stage on aerodynamic interferences and aerodynamic performance of the carrier and orbital stage are studied.

Two 3-D Mach Contours for two different carrier stage angles of attack, namely $\alpha = 0.0$ ° (case b1) and $\alpha = 3.0$ ° (case b1) are depicted in Fig. 34.

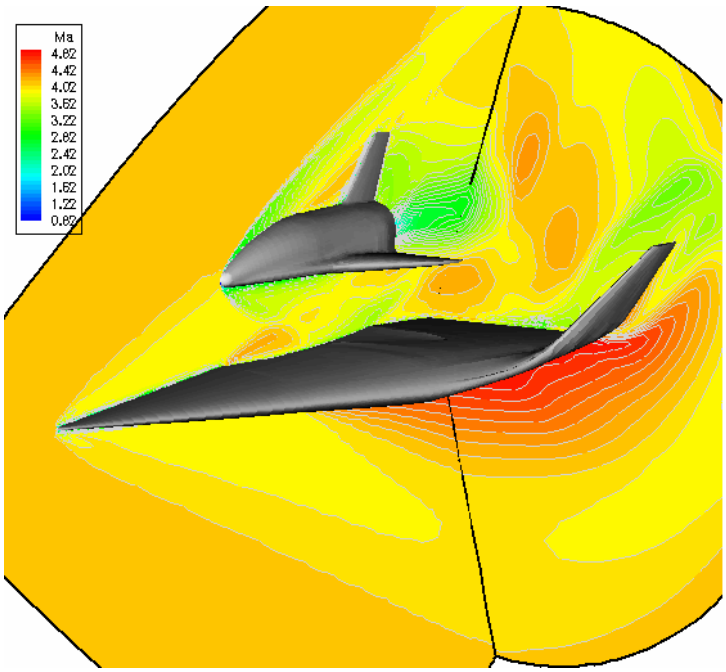

(a). Mach contour for test case b1

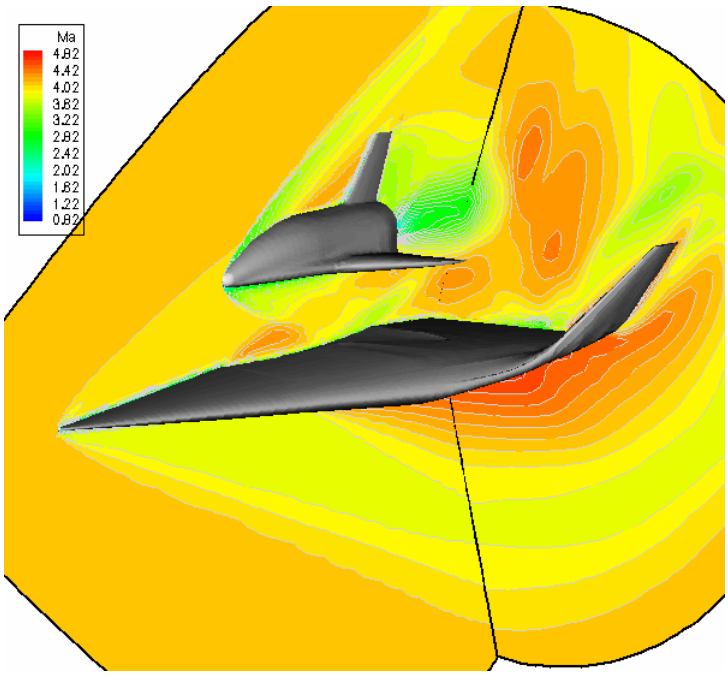

(b). Mach contour for test case b2

Figure V.34: Comparison of Mach contours for two different ELAC1C angles of attack: (a) $M_\infty = 4.04$, $\alpha = 0.0°$, $\Delta\alpha = 0.0°$, $h/l_{EOS} = 0.225$; (b) $M_\infty = 4.04$, $\alpha = 3.0°$, $\Delta\alpha = 0.0°$, $h/l_{EOS} = 0.225$.

An increase of the carrier stage angle of attack results the change of the ELAC1C bow shock line. Consequently, the supersonic flows behind the lower part of the ELAC1C bow shock decelerates producing an increase in pressure on the lower surface of the ELAC1C, while the flow on the front of the gap region undergo an acceleration or the surface pressure of the upper part of the ELAC1C decreases. The upper part of the ELAC1C bow shock moves up and interacts with the upper part of the EOS bow shock. As the consequence of the increase of flow velocity in front of the gap region, the supersonic velocity in the gap region increases, hence both the orbital and carrier stages feel a suction flow. Thus, this affects on aerodynamic characteristics of the EOS and ELAC1C vehicles.

- **Lift coefficient versus angle of attack (C_L .vs. α)**

  Figure V.35 shows the graphs of lift coefficient versus angle of attack for the computations of the ELAC1C and EOS vehicles and a set of corresponding experimental data. With increasing angle of attack of the carrier stage, an additional lift for the carrier stage is greater than that of the EOS. This is caused the pressure changes due to the alteration of the bow shock at higher angle of attack of the ELAC1C as discussed before. Comparing the computational results to the experimental data, both the computational results of the test cases b1 and b2 for the EOS show a good tendency with a reasonable error, while for the ELAC1C the calculations give a good agreement.

- **Drag coefficient versus angle of attack (C_D .vs. α)**

  Concerning the effect of the carrier stage angle of attack on drag coefficient, the configurations of the EOS and ELAC1C give a slight decrease in drag coefficient with the increased angle of attack as shown the graph of drag coefficient versus angle of attack in Fig. V.36. Comparing to the experimental results, the computed drag coefficient results give a reasonable agreement for the EOS vehicle and excellent agreement for the ELAC1C. From these results, it can be concluded that the drags of the vehicles are

mainly contributed by the shock waves rather than the drag due to the flow friction.

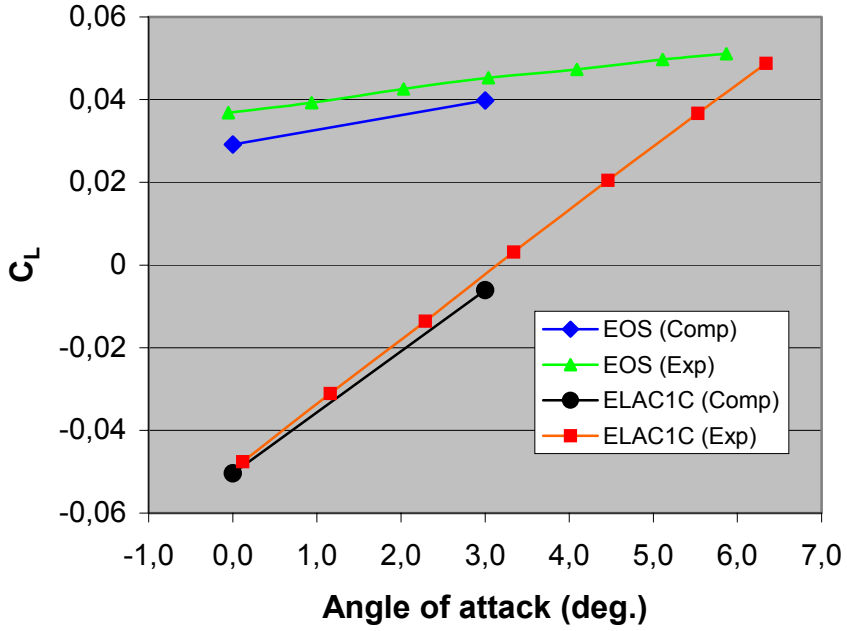

Figure V.35: Graphs of computed and measured lift coefficient versus angle of attack at $M_\infty = 4.04$, $Re_m = 50.0 \times 10^6$ (experiment), $\Delta\alpha = 0.0°$, $h/l_{EOS} = 0.225$.

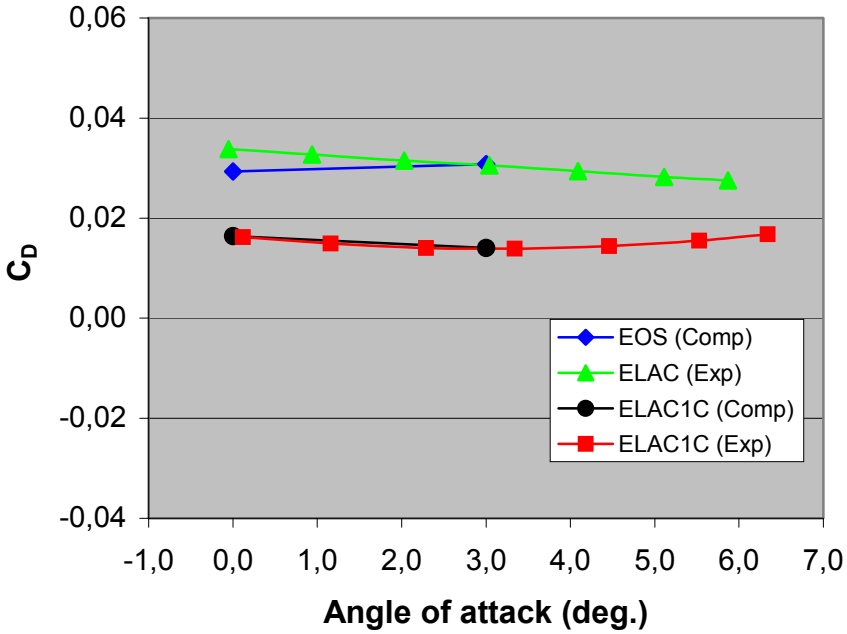

Figure V.36: Graphs of computed and measured drag coefficient versus angle of attack at $M_\infty = 4.04$, $Re_m = 50.0 \times 10^6$ (experiment), $\Delta\alpha = 0.0°$, $h/l_{EOS} = 0.225$.

- **Pitching moment coefficient versus angle of attack (C_M .vs. α)**

  The effect of the carrier stage angle of attack on pitching moment of the ELAC1C and EOS vehicles are shown by the graphs of pitching moment coefficient versus angle of attack in Fig. V.37. The increase of angle of attack of the carrier stage gives a higher pitching moment increment for the carrier stage and a smaller pitching moment increment for the orbital stage. In Fig. V.37, the calculation for zero angle of attack (case b1) indicates a good agreement with the experimental data, while a poorer agreement between the computed and measured pitching moment accounted for the higher angle attack (case b2).

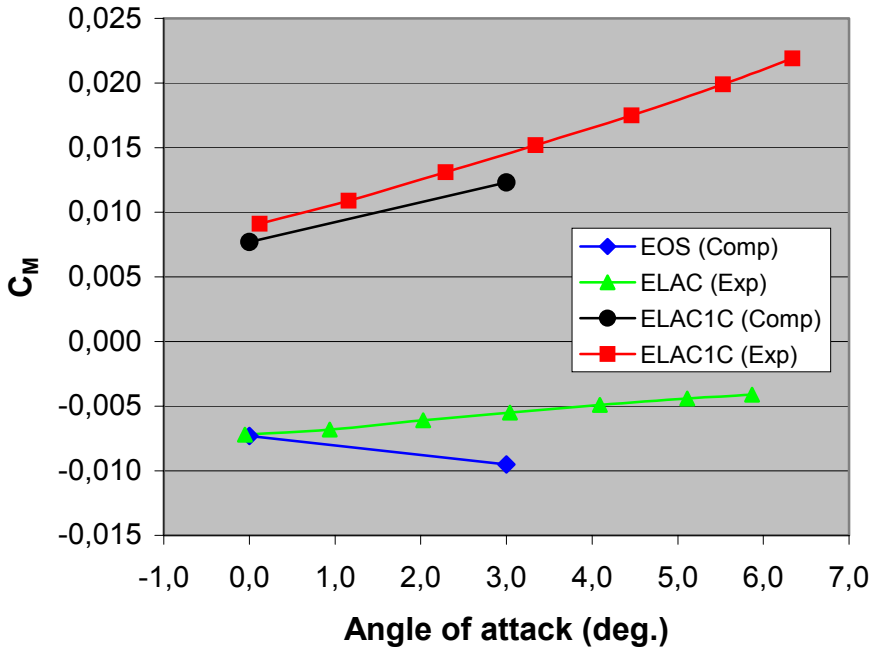

Figure V.37: Graphs of computed and measured pitching moment coefficient versus angle of attack at $M_\infty = 4.04$, $Re_m = 50.0 \times 10^6$ (experiment), $\Delta\alpha = 0.0°$, $h/l_{EOS} = 0.225$.

- **Drag Polar (C_L .vs. C_D)**

  The drag polar graphs for the experiment and computation of the ELAC1C and EOS configurations are given in Fig. V.38. At the same lift coefficient, the carrier stage has a lower drag coefficient than the orbital stage.

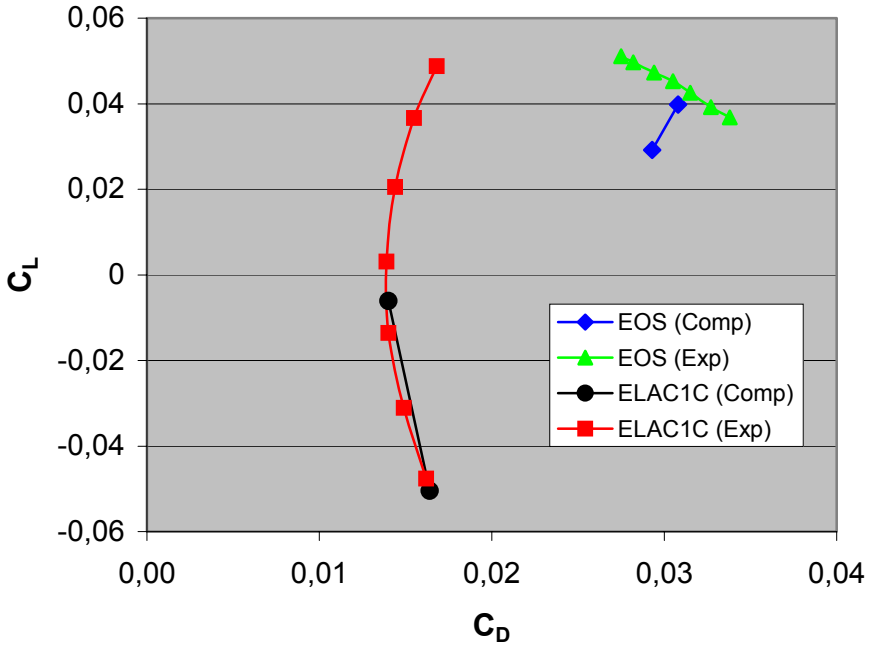

Figure V.38: Graphs of computed and measured drag polars at $M_\infty = 4.04$, $Re_m = 50.0 \times 10^6$ (experiment), $\Delta\alpha = 0.0°$, $h/l_{EOS} = 0.225$.

5.2.2 Effects of Separation Distance between the Stages

The simulations of the separation process of the two-stage ELAC1C – EOS vehicle system for steady flow conditions are also performed by considering separation distance change. The effect of the vertical distance change between the stages is depicted by Mach number contours in 3-D view of Fig. V.39 (a) and (b) for two different relative distances, namely 0.225 and 0.325, respectively.

The increase of the separation distance (h/l_{EOS}) results the larger gap region, as consequence flow velocity increases giving a suction effect on both the stages, and the Mach contours in the wake presents changes. This causes that the lift coefficient for the EOS slightly decreases and, contrarily the ELAC1C lift coefficient increases as described in the graphs of lift coefficient versus angle of attack in Fig. 40.

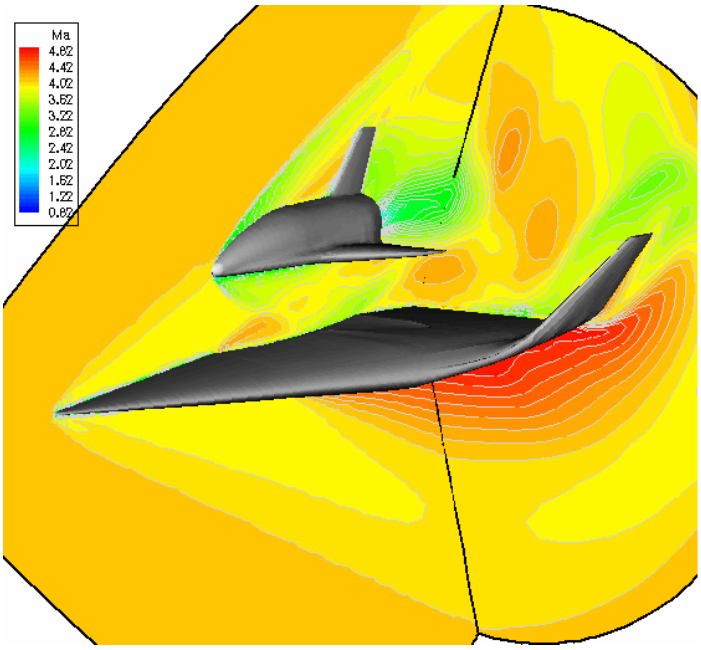

(a). Mach contour for test case b1

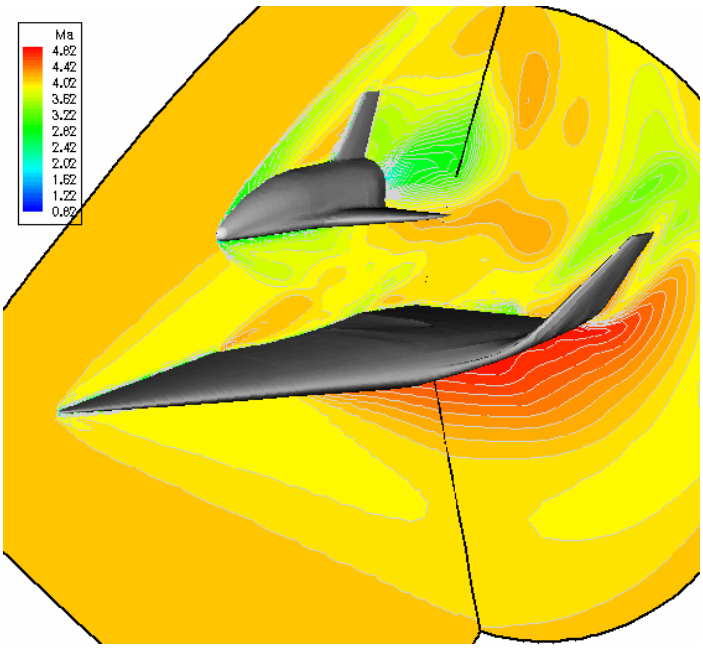

(b). Mach contour for test case b5

Figure V.39: Comparison of Mach contours for two different ELAC1C vertical distances: (a) $M_\infty = 4.04$, $\alpha = 0.0°$, $\Delta\alpha = 0.0°$, $h/l_{EOS} = 0.225$; (b) $M_\infty = 4.04$, $\alpha = 0.0°$, $\Delta\alpha = 0.0°$, $h/l_{EOS} = 0.325$.

In addition, increasing the separation distance also causes the reduction of the strength of aerodynamic interferences between the stages. This is indicated by a decrease in drag coefficient for the EOS as shown in the graphs of drag coefficient versus angle of attack of Fig. 41, but it does not give a significant influence for the ELAC1C. In Figs. 40 and 41, the comparison of the numerical and experimental results for the lift and drag coefficients of the ELAC1C and EOS show a good agreement.

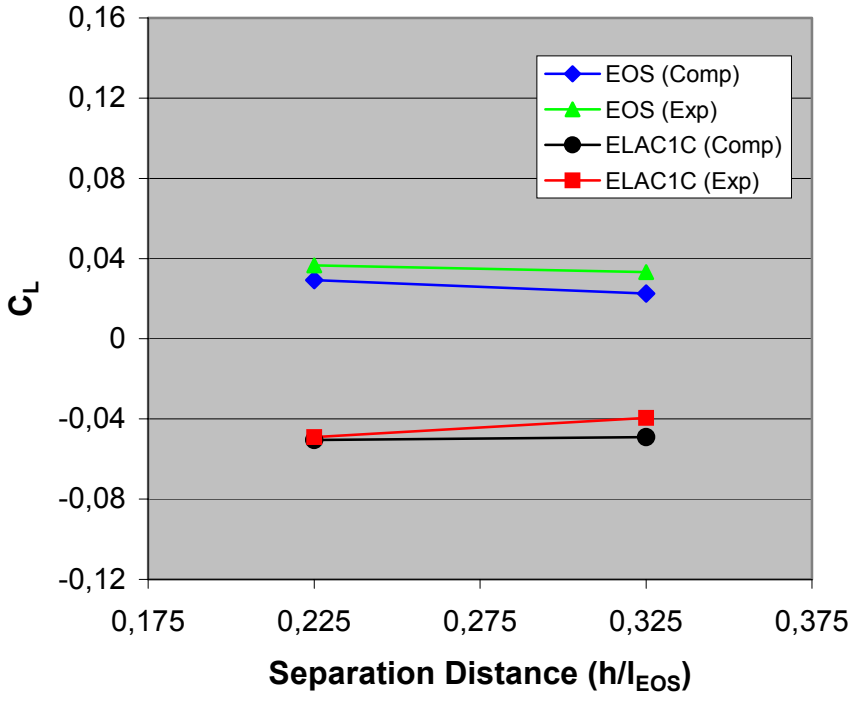

Figure V.40: Graphs of computed and measured lift coefficient versus separation distance at $M_\infty = 4.04$, $Re_m = 50.0 \times 10^6$ (experiment), $\alpha = 0.0°$, and $\Delta\alpha = 0.0°$.

Furthermore, the value of pitching moment of the orbital stage becomes a positive with the increase of the separation distance between the stages as shown by the graphs of pitching moment coefficient versus angle of attack in Fig. 42. This indicates that the longitudinal stability of the orbital stage becomes unstable condition with increasing the separation distance. The pitching moment of the ELAC1C just slightly change with increasing the separation distance. The computed pitching moment show a very good agreement compared to the corresponding experimental data.

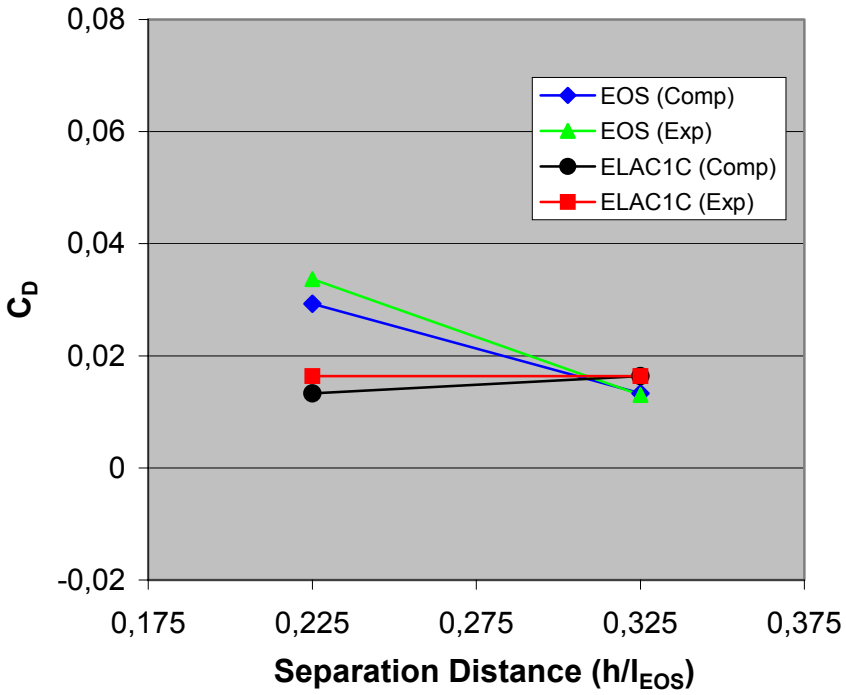

Figure V.41: Graphs of computed and measured drag coefficient versus separation distance at $M_\infty = 4.04$, $Re_m = 50.0 \times 10^6$ (experiment), $\alpha = 0.0°$, and $\Delta\alpha = 0.0°$.

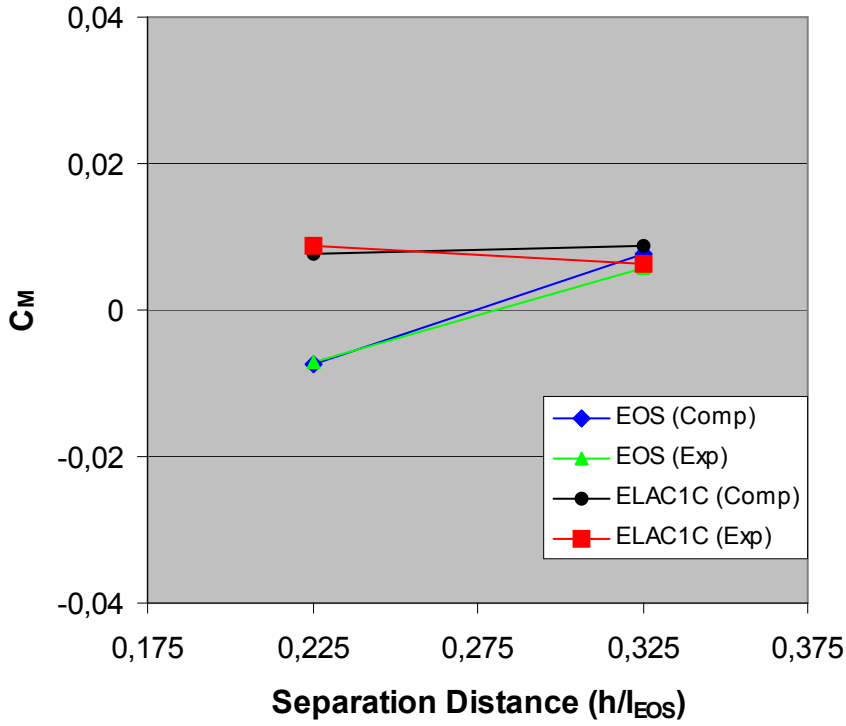

Figure V.42: Graphs of computed and measured pitching moment coefficient versus separation distance at $M_\infty = 4.04$, $Re_m = 50 \times 10^6$, $\alpha = 0.0°$, and $\Delta\alpha = 0.0°$.

Figure V.43 shows aerodynamic efficiency (C_L/C_D) of the EOS and ELAC1C vehicles. With increasing the separation distance the aerodynamic efficiency of the EOS vehicle slightly decreases, but the ELAC1C aerodynamic efficiency increases.

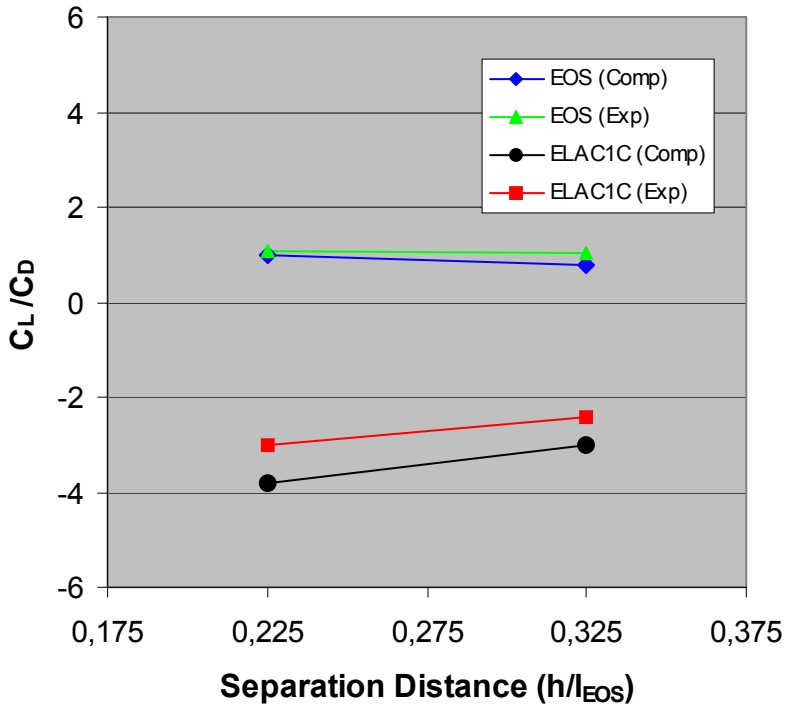

Figure V.43: Graphs of computed and measured lift over drag versus separation distance at $M_\infty = 4.04$, $Re_m = 50.0 \times 10^6$ (experiment), $\alpha = 0.0°$, and $\Delta\alpha = 0.0°$.

5.2.3 Effects of Orbital Stage Angle of Attack

During the separation manoeuvre, apart of the change of the distance between the stages, the orbital stage also perform the angle of attack change based on the moment reference point located at 0.65 of the fuselage length of the EOS from its nose, while the ELAC1C stage is in a stationery. The change of the orbital stage angle of attack results the change in the gap region, hence it affects flow field pattern and aerodynamic characteristics of the vehicles. Figure 44 shows Mach contours of the vehicles system in 3D view for three different orbital stage angles of attack, namely $\Delta\alpha = 0.0$, 2.0 and 5.0 degrees.

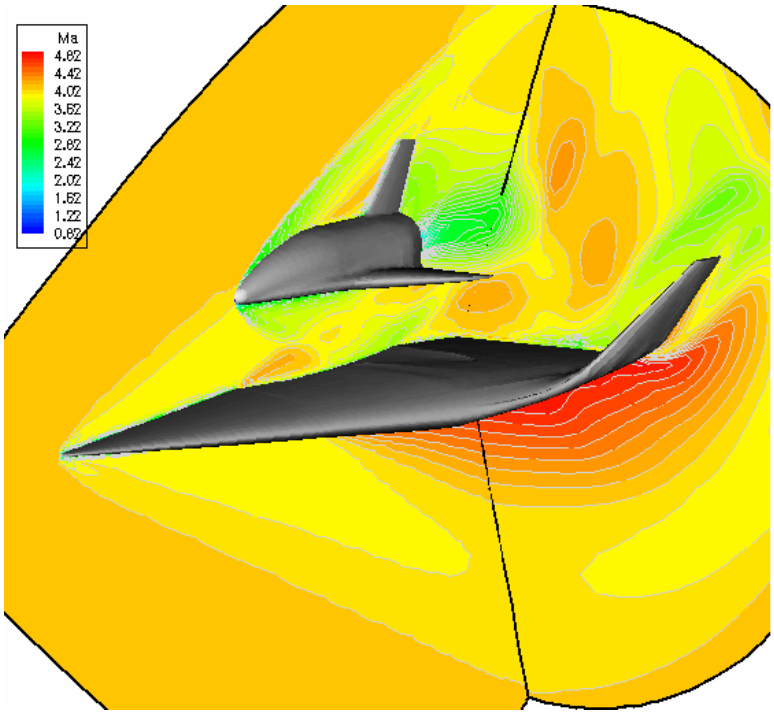

(a) Mach contour for test case b1

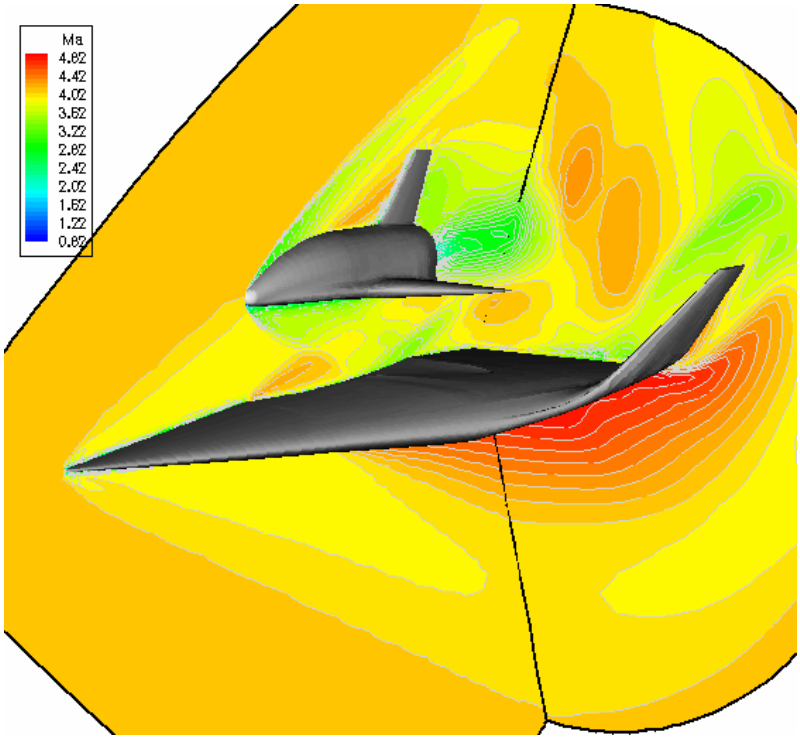

(b) Mach contour for test case b3

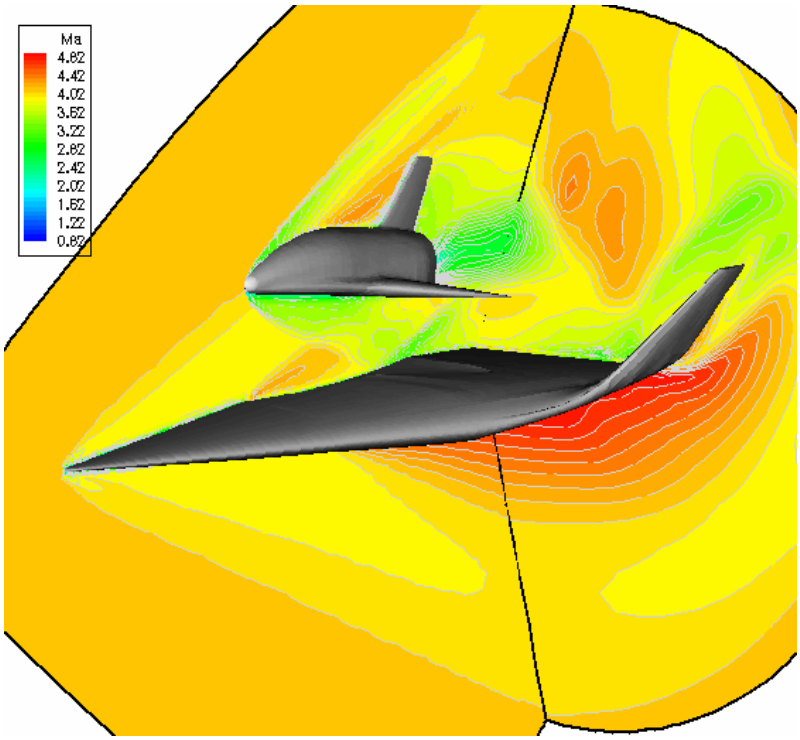

(c) Mach contour for test case b4

Figure V.44: Comparison of Mach contours for three different EOS angles of attack: (a) $M_\infty = 4.04$, $\alpha = 0.0°$, $\Delta\alpha = 0.0°$, $h/l_{EOS} = 0.225$; (b) $M_\infty = 4.04$, $\alpha = 0.0°$, $\Delta\alpha = 2.0°$, $h/l_{EOS} = 0.225$; (c) $M_\infty = 4.04$, $\alpha = 0.0°$, $\Delta\alpha = 5.0°$, $h/l_{EOS} = 0.225$

As shown in Fig. V.44, increasing the orbital stage angle of attack, a point generated by the interaction of the ELAC1C bow shock wave and EOS bow shock wave moves from the upper part to lower part of the EOS shock wave line. The increased orbital stage angle of attack obtains the EOS nose moving up and its tail moving down, consequently the flow in the gaps is subjected to a contraction. When supersonic flow experiences a contraction the flow velocity will decrease as shown in Figs. V.44 (b) and (c). While, in the region above the EOS surface the area of suction flow increases with the increased orbital stage angle of attack. The Mach contour in the wake region presents a change. In addition, the lower part of the EOS shock wave strikes the upper surface of the ELAC1C at a further downstream with increasing

angle of attack. While, the variation of the orbital stage angle of attack does not give a significant change in the regions of the bottom of the ELAC1C and in the wake.

The effects of the orbital stage angle of attack on aerodynamic characteristics of the EOS and ELAC1C vehicles are shown in Figs. V.45 – V.47. In Fig. V.45 the graphs of lift coefficient versus the orbital stage angle of attack shows that an increase of the orbital stage angle of attack provides an increment of the EOS lift coefficient and a decrement of the ELAC1C lift coefficient. This is caused a flow deceleration in the gap region due to the increased orbital angle of attack that results a pressure increase subjecting on both the stages. Concerning the comparison between the computational results and the experimental data, the calculated lift coefficient for the EOS vehicle presents an under estimation, while the calculated lift coefficient of the ELAC1C provides a good agreement with the experimental data.

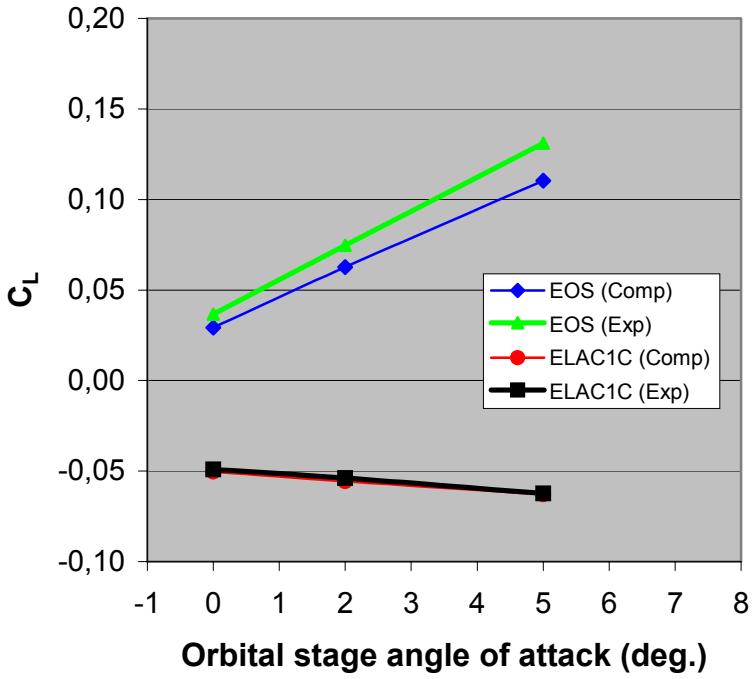

Figure V.45: Graphs of computed and measured lift coefficient versus orbital stage angle of attack at $M_\infty = 4.04$, $Re_m = 50.0 \times 10^6$ (experiment), $\alpha = 0.0°$, $h/l_{EOS} = 0.225$.

The graphs of drag coefficient versus orbital angle of angle of attack of the experimental and computational results for the EOS and ELAC1C are depicted in Fig. V.46. There is contradiction results between the computed and measured EOS drag related to the effect of the orbital angle of attack. The computed drag coefficient increases, but the measured drag coefficient decreases with increasing orbital angle of attack. This may due to the computation result is very sensitive to the location of interaction between the upper part of the ELAC bow shock wave and EOS bow shock wave. When the upper part of the ELAC bow shock wave hits the EOS bow shock wave just in the front of the EOS nose (as shown in Fig. V.44.b for test case b3), the calculated EOS drag coefficient provides a good agreement with the experimental data, but when the upper part of the ELAC1C bow shock strikes on the upper EOS bow shock wave (as shown in Fig. V.44.a for the test case b1) the calculated EOS drag coefficient presents an under estimation, and contrarily, when it hits the lower EOS bow shock wave (as shown in Fig. V.44.c for the test case b4) the computed drag coefficient shows an over estimation. In addition, the calculated lift coefficient for ELAC1C shows a good agreement with the experimental data for various orbital stage angles of attack.

Figure V.47. shows the graph of calculated and measured pitching moment coefficient versus orbital stage angle of attack for the EOS and ELAC1C. For all orbital stage angles of attack ($\Delta\alpha$), the orbital stage (EOS) provides a negative pitching moment coefficient, while the carrier stage (ELAC1C) presents positive pitching moment. With the increase of orbital stage angle of attack the carrier stage obtains an additional pitching moment coefficient, while, the EOS pitching moment coefficient decreases. The prediction of the pitching moment coefficient of the ELAC1C gives a good agreement with the experimental data for all orbital stage angles of attack, but the pitching moment prediction of the EOS only produces a good agreement with the experimental data when the relative angle of attack is 0.0 deg.

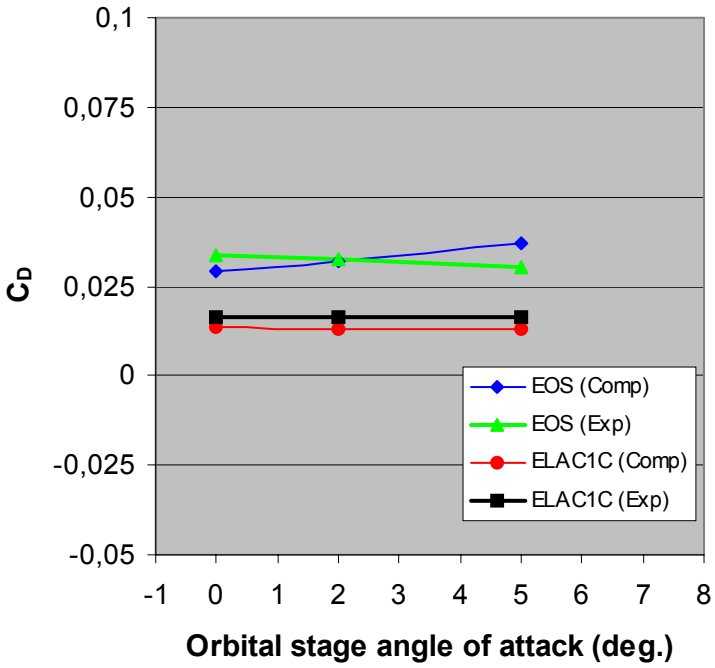

Figure V.46: Graphs of computed and measured drag coefficient versus orbital stage angle of attack at $M_\infty = 4.04$, $Re_m = 50.0 \times 10^6$ (experiment), $\alpha = 0°$, and $h/l_{EOS} = 0.225$.

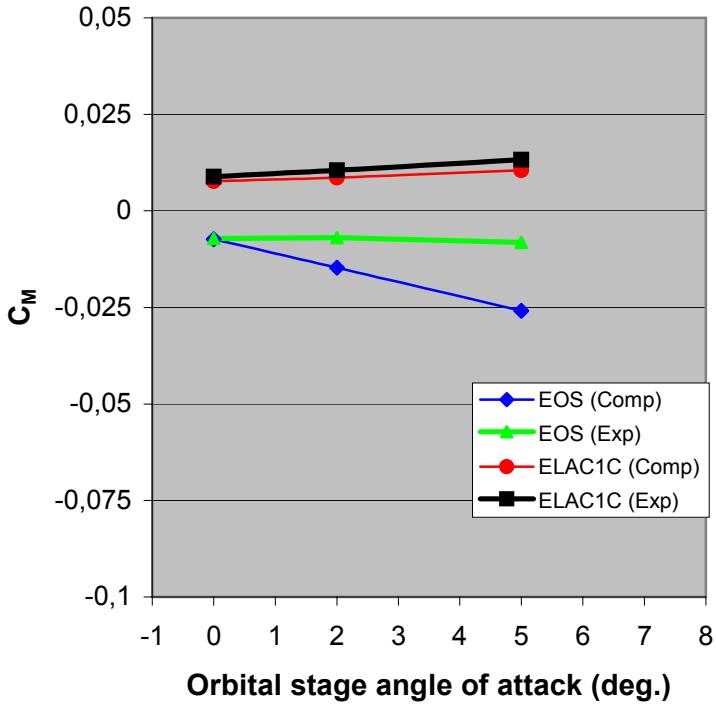

Figure V.47: Graphs of computed and measured pitching moment coefficient versus orbital stage angle of attack at $M_\infty = 4.04$, $Re_m = 50.0 \times 10^6$ (experiment), $\alpha = 0.0°$, and $h/l_{EOS} = 0.225$.

CHAPTER VI
ANALYSIS OF UNSTEADY AERODYNAMICS OF STAGE SEPARATION OF TSTO SPACE VEHICLE SYSTEM

In chapter V the simulations of stage separation of the TSTO space transportation system in the steady flow state have been discussed in detail including the effects of angle of attack, relative angle of attack and relative distance. Yet, these simulations have not included effects of a downwash due to the orbital stage motion during the separation manoeuvre. In order to simulate real flows during the separation manoeuvre, the downwash effects should be considered in the computation. The downwash is produced by the influence of the vehicle motion during the separation changing with time that influences on flow features and aerodynamic characteristics of the vehicle system.

1. Computational Test

The computations of the unsteady stage separation are performed on the fully two-stage-to-orbit configuration (EOS and ELAC1C). In the simulation of the unsteady stage separation, the orbital stage discards from a position closed to the orbital stage to a position that the interaction between the stages becoming vanish. Such a simulation requires the determination of the initial and end conditions as well as reduced frequency. For the initial condition the steady state solution is used as the input. For this study, the steady state solution is computed at a free stream Mach number of 4.0 with the orbital stage angle of attack, $\Delta\alpha$ = 2.0 deg. and the separation distance between the stages, $\mathbf{h/l}_{EOS}$ = 0.125. In addition, the end position of the orbital stage is $\Delta\alpha$ = 6.0 deg. and $\mathbf{h/l}_{EOS}$ = 0.325. The separation motion uses a rotation center of 0.65 from the nose of the EOS stage. In order to describe a speed of the vertical motion of the orbital stage or a downwash, the reduced frequency value has to be specified. This is non dimensional number expressing a ratio of the angular velocity to the free-stream velocity.

The simulations of the unsteady stage separation are carried out for three reduced frequencies with the detail computation tests given in Table VI.1.

Case	Mach number	Relative distance (h/l_{EOS})	Relative angle of EOS ($\Delta\alpha$) in deg.	Angle of attack (α) in deg.	Reduced frequency (k_{red})
b6	4.04	0.125 – 0.325	2.0 – 6.0	0.0	0.22
b7					0.5
b8					1.0

Table VI.1: Unsteady state test cases for the ELAC1C and EOS configuration.

In general, the alteration of distance between the stages, orbital angle of attack as well as pitch rate and separation occurs continuously during separation manoeuvre. However, in the numerical simulations the staging path of the orbital stage is approached with the number of steps. This is intended to reduce the computational cost while considering the accuracy of the solutions. In addition, the separation trajectory which takes place from the lower to upper positions is approached using a one-minus-cosines function is aimed at generating harmonically motion simultaneously in separation distance and angle of attack of the orbital stage as given in Eqs. (II.11) and (II.12).

The unsteady calculations start with the use of the input of the steady state solution. Then, the unsteady solution for each time step is obtained by solving the unsteady Euler equations using the dual time-stepping method. Every time step the orbital stage body changes its position inducing mesh deformation near the orbital stage surface. This requires a dynamic grid adaptation generated by locally grid smoothing using the Laplace algorithm. The unsteady transformation of the Euler equations takes into account the velocity of the mesh as well as the deformation of the cells. The result of the moving grids for the prescribed trajectory is shown in Fig. VI.1.

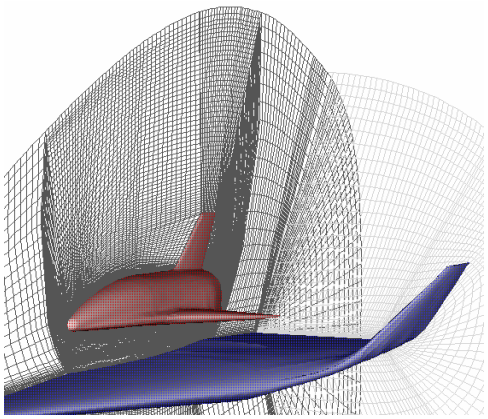

a) $\Delta\alpha = 2.0°$, $h/l_{EOS} = 0.125$

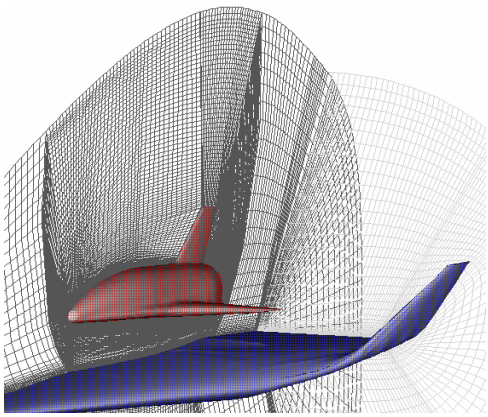

b) $\Delta\alpha = 2.4°$, $h/l_{EOS} = 0.144$

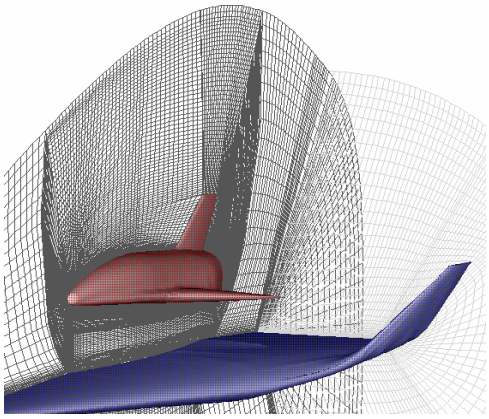

c) $\Delta\alpha = 3.4°$, $h/l_{EOS} = 0.194$

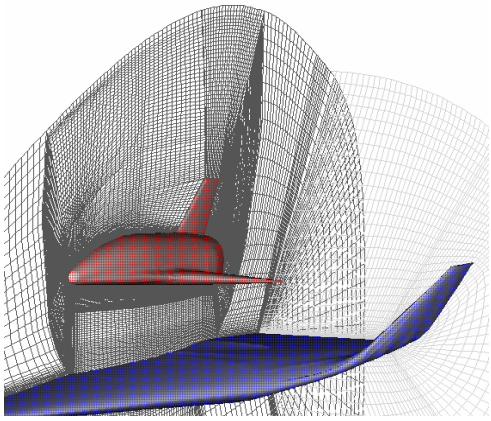

d) $\Delta\alpha = 4.6°$, $h/l_{EOS} = 0.256$

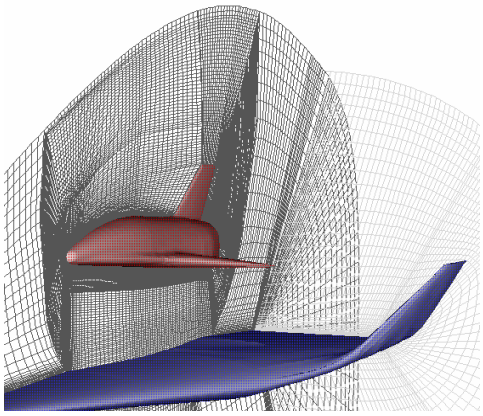

e) $\Delta\alpha = 5.6°$, $h/l_{EOS} = 0.306$

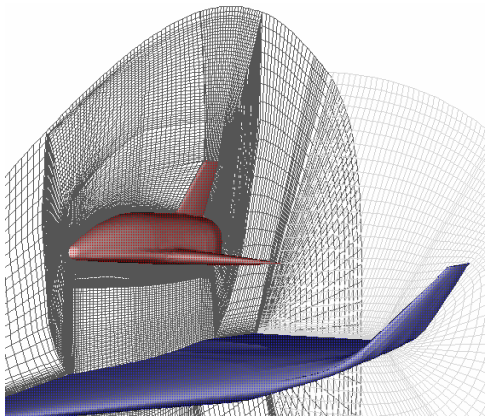

f) $\Delta\alpha = 6.0°$, $h/l_{EOS} = 0.325$

Figure VI.1: Dynamic grids of the EOS and ELAC 1C vehicle for several relative incidences $\Delta\alpha$ and vertical distances h/l_{EOS}.

The mesh deformation occurs only in limited regions around the EOS model that was generated with the O-grid topology. The mesh closed to the solid surface conforms to the motion of the EOS surface at all times. The remaining meshes outside the moving regions keep to be fixed.

2. Simulation Results of Unsteady Stage Separation of Fully Two-Stage-to-Orbit Configuration

The computation are carried out for one cycle consisting of 40 time steps, that is from the initial position and back to the initial position again. The convergence solution for each time step of the simulation is resulted if the residual of relative density does not exceed 5 x 10^{-4}. The accurate unsteady flow results are then obtained by calculating from the lower position to the upper position of the second cycle.

2.1 Aerodynamic Characteristics of Unsteady Stage Separation

Figures VI.2 - VI.4 show the complete cycle of unsteady aerodynamic characteristics of the stage separation including lift, drag and pitching moment coefficients for three different reduced frequencies, namely k_{red} = 0.22, 0.5 and 1.0, respectively. The results of the aerodynamic characteristics at the start points of the first cycle and the second cycle show discrepancy. The discrepancy increases with increasing the reduced frequency. This is caused the values of the aerodynamic coefficients at the start point of the first cycle are almost the same with the values of the aerodynamic coefficients at the steady state which does not take into account the downwash accurately. While, the solutions at the second cycle considering downwash gives more accurate that they are taken as the final results of the simulation.

Concerning unsteady aerodynamic coefficients as shown in Figs. VI.2 - VI.4, the computation at each reduced frequency obtains the different profiles of unsteady aerodynamic coefficient. At the lower reduced frequency, for example, the downwash contributes only small additional lift

of the orbital stage. Increasing the amplitude of the stage separation provides an increase of the EOS lift coefficient, except at beginning of the separation the lift coefficient slightly decreases. While, at the higher reduced frequency, the effect of downwash gives much influence on the orbital stage lift coefficient. The orbital stage experiences a large amount decrease in lift coefficient with increasing the amplitude until the minimum lift coefficient is reached. Further an increase of the amplitude gives a higher increase of the lift coefficient of the EOS. The drag coefficient profiles at various reduced frequencies have the similar characteristics to the lift coefficient profiles, but the magnitude of drag increment is only small values. However, the profiles of pitching moment coefficient of the EOS show an opposite characteristic compared to the lift coefficient profiles. The pitching moment coefficient becomes less negative with increasing the amplitude of the stage separation until at the further steps of the amplitude at which the gradient of pitching moment coefficient changes. The detail aerodynamic characteristics of unsteady stage separation of EOS vehicle are provides in Appendix H.

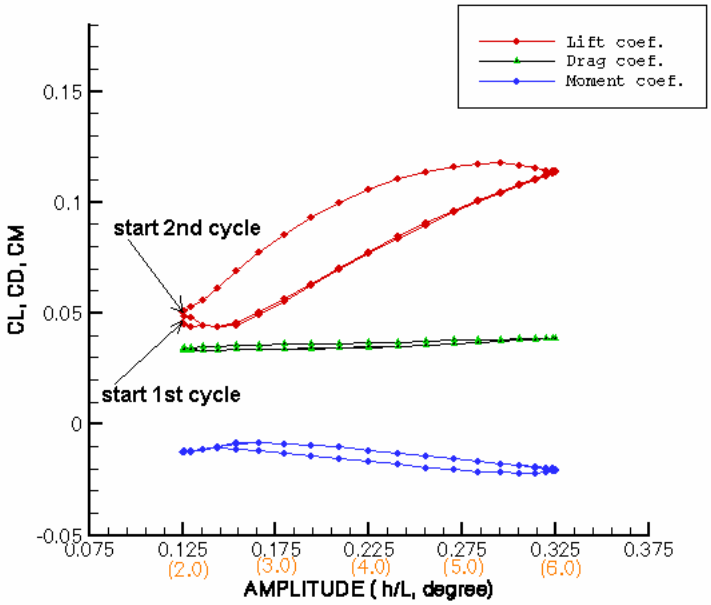

Fig. VI.2 Aerodynamic characteristics of unsteady stage separation for the reduced frequency, k_{red} = 0.22 at M_∞ = 4.04; α = 0.0°; $\Delta\alpha$ =2.0° - 6.0°; h/l_{EOS} = 0.125 - 0.325.

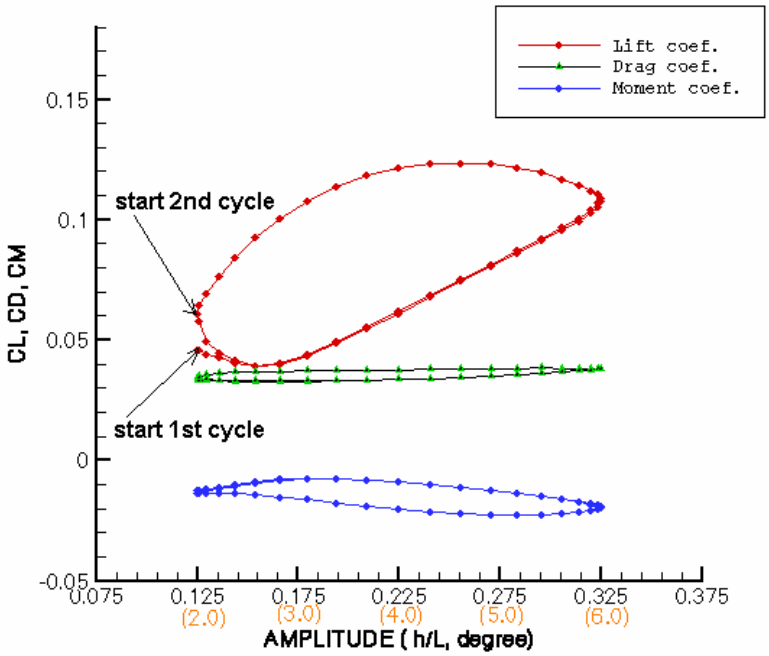

Fig. VI.3 Aerodynamic characteristics of unsteady stage separation for the reduced frequency, k_{red} = 0.5 at M_∞ = 4.04; α = 0.0°; Δα =2.0° - 6.0°; h/l_{EOS} = 0.125 - 0.325

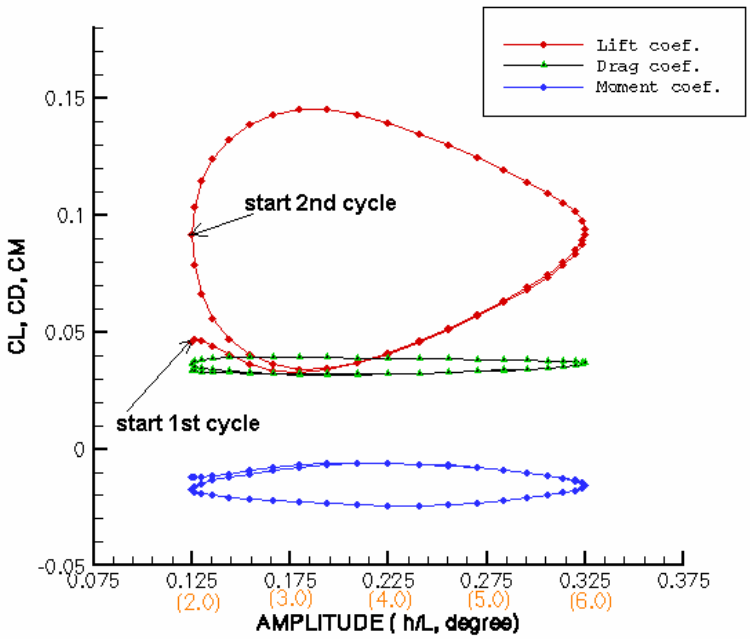

Fig. VI.4 Aerodynamic characteristics of unsteady stage separation for the reduced frequency, k_{red} = 1.0 at M_∞ = 4.04; α = 0.0°; Δα =2.0° - 6.0°; h/l_{EOS} = 0.125 - 0.325.

2.2 Instantaneous Flow Features of Stage Separation

Instantaneous flow features of the EOS and ELAC1C configuration during the separation manoeuvre presented in density contours and Mach number contours are analyzed. The results of the unsteady flow for three different reduced frequencies are given below.

2.2.1 Instantaneous Flow Features at reduced frequency of 0.22

Figures VI.5 and VI.6 show the pictures of instantaneous density and Mach number contours at the reduced frequency of 0.22, respectively. At this condition a required time for staging from the lower condition to the upper condition is 0.262 second. The speed of downwash is lower that only gives slightly effects on the flow features of the EOS and ELAC1C. At the time of 0.0 second where the separation distance of 0.125 and the orbital angle of attack of 2.0 deg. the density contours at the symmetry plane in Fig. VI.5 shows that the flow features including bow shock waves of ELAC1C and EOS, expansion wave, reflected shock waves as well as the interaction points is almost not affected by the downwash.

At a time of 0.052 sec which the relative distance is of 0.144 and the relative angle of attack of 2.4 deg. the bow shock wave of the ELAC1C slightly moves to the front of the EOS nose. The line of the bow shock wave of the ELAC1C before hitting the EOS bow shock wave subjects to a few bending due to an induced flow of downwash. The upper bow shock angle seems increase when closer to the upper condition. At the same time the location of interaction point of the bow shock wave of the EOS and the shock wave generated by the curvature of the ELAC1C cavity travels to downstream in the middle gap. The reflected shock wave on the rear of the lower surface of the EOS also shifts a further rear. In addition, the effect of the induced flow does not give a significant impact to the flow under the ELAC1C vehicle.

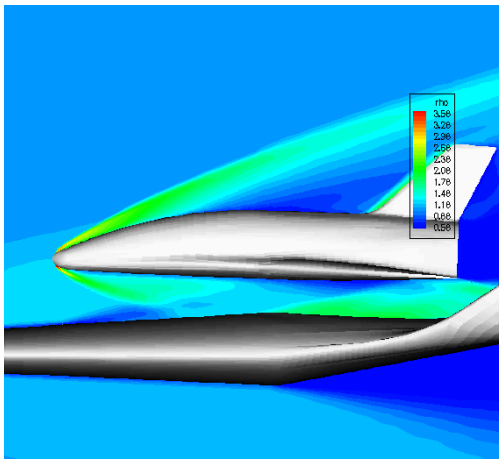

time = 0.000 sec.

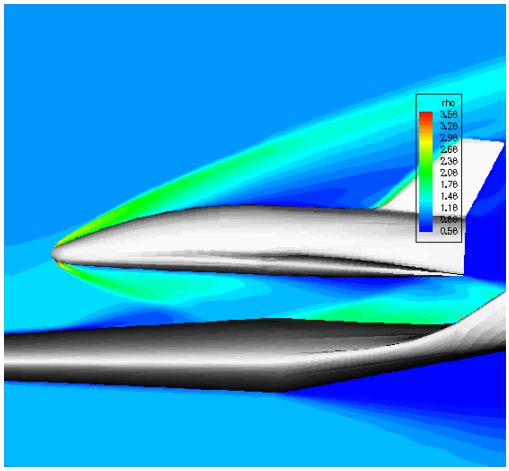

time = 0.052 sec.

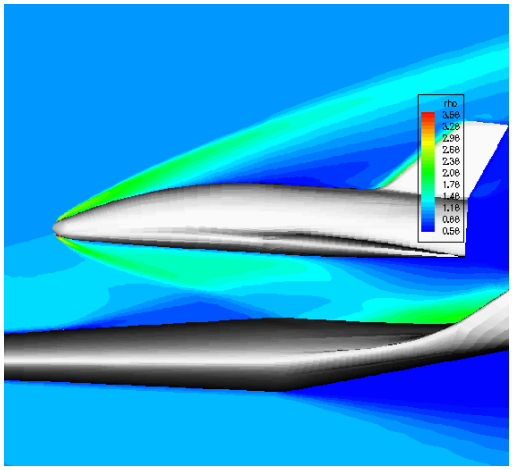

time = 0.105 sec.

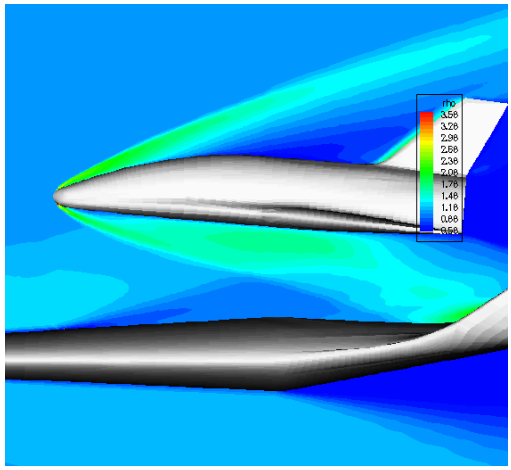

time = 0.157 sec.

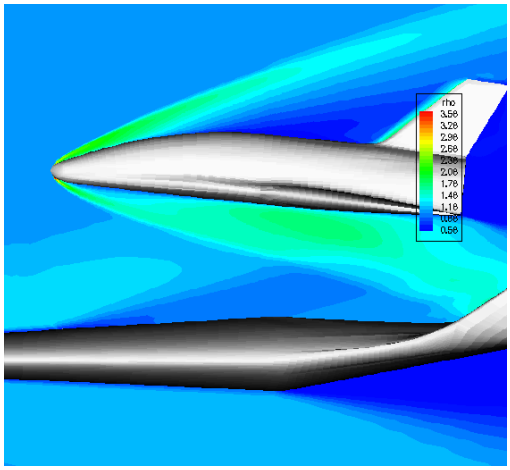

time = 0.209 sec.

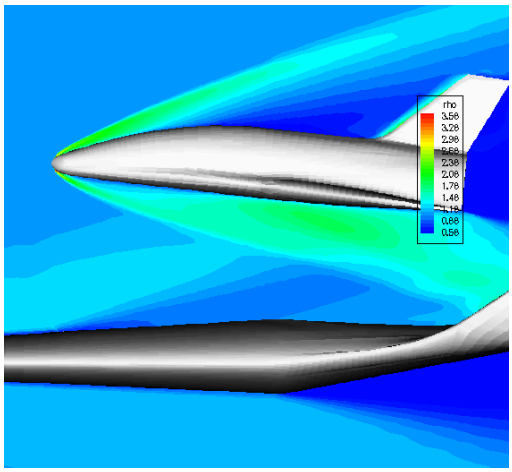

time = 0.262 sec.

Figure VI.5: Instantaneous density contours at six different time levels during separation at M_∞ = 4.04; α = 0.0°; Δα =2.0° - 6.0° deg.; h/l_{EOS} = 0.125-0.325; k_{red} = 0.22.

Subsequently at the time of 0.105 sec. which a relative distance is of 0.194 and a relative angle of attack of 3.4 deg. the bow shock wave of the ELAC1C slightly moves to the lower surface of the EOS. The line of the bow shock wave of the ELAC1C becomes a more bent before hitting the EOS bow shock wave due to the down wash effect. Also, the upper bow shock angle increases and the location of interaction point of the bow shock waves go a further rear. However, no reflected shock wave occurs on the rear of the lower surface of the EOS. Again, no change of flow occurs under the ELAC vehicle due to the induced flow.

Further the increase of separation times, namely 0.157 sec., 0.209 sec. and 0.262 sec. shown in Fig. VI.5 with which the corresponding relative distances of 0.256, 0.306 and 0.325., and the corresponding relative angles of attack of 4.6 deg. 5.6 deg. and 6.0 deg. the bow shock wave of the ELAC1C hits on the further rear of the lower bow shock wave of the EOS corresponding to the orbital stage motion. The upper bow shock angles gradually further increase and the locations of the interaction points of the bow shock wave of the EOS and the shock wave shift further downstream. In addition, at the trailing edge of the EOS lower surface expansion flow occurs.

The 3D flow views of the unsteady flow in Mach number contours are depicted in Fig. VI.6. At the separation time of 0.0 sec. the flow with lower Mach number or higher static pressure subjects to a front part of the upper surface of the EOS body. While, the rear part of the upper surface experiences the higher Mach number or lower static pressure flow. The upper surface condition only experiences a slightly change with increasing the separation time. On the other hand, a large change in Mach number distribution occurs on the lower surface of the EOS body and in the gap region between the stages.

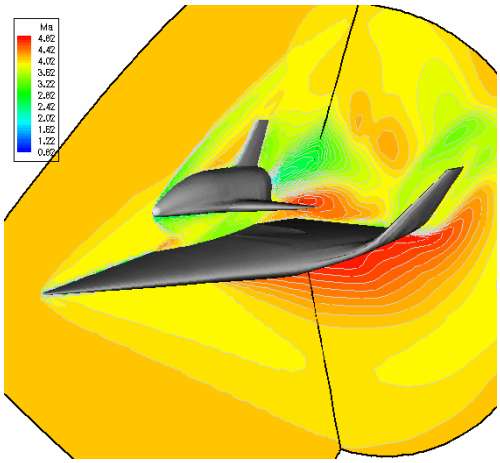

time = 0.000 sec.

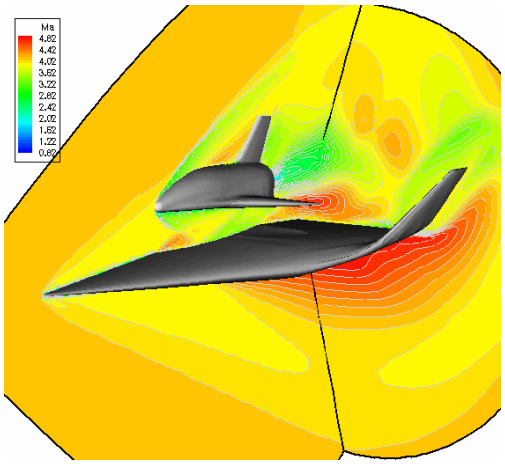

time = 0.052 sec.

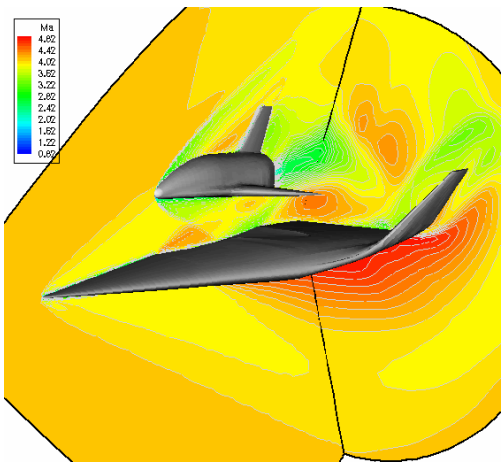

time = 0.105 sec.

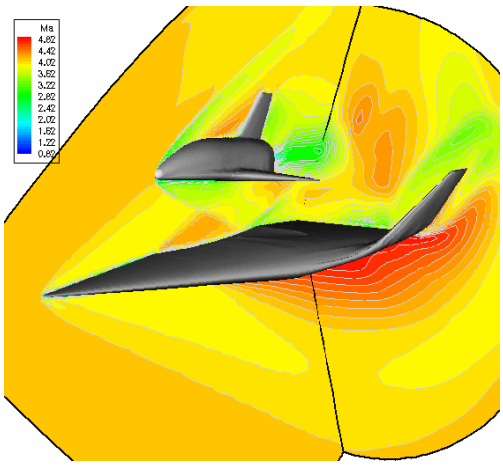

time = 0.157 sec.

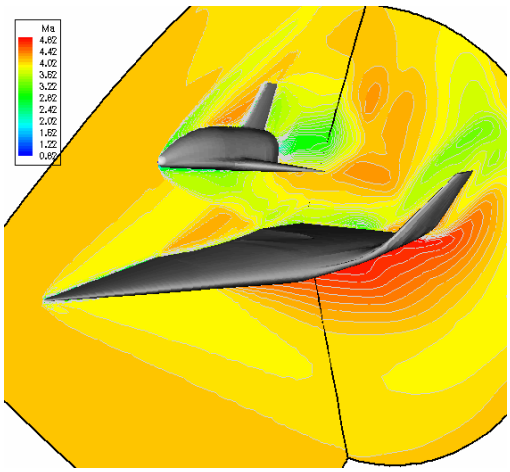

time = 0.209 sec.

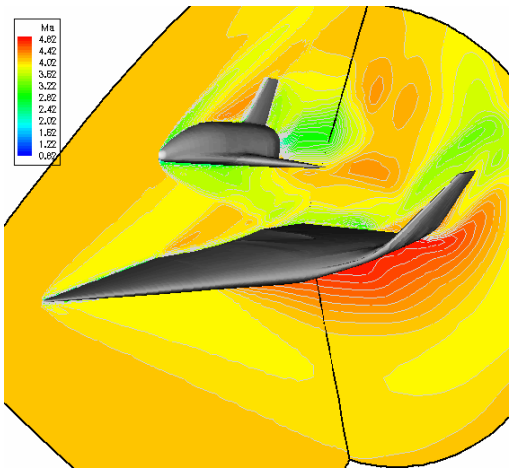

time = 0.262 sec.

Figure VI.6: Instantaneous Mach contours at six different time levels during separation at M_∞ = 4.04; α = 0.0°; Δα =2.0° - 6.0°; h/l_{EOS} = 0.125-0.325; k_{red} = 0.22.

At the separation time of 0.052 sec. the front and rear parts of the lower surface of the EOS body undergo the lower Mach number or higher static pressure flow, but on the middle part accommodates the higher Mach number flow due to the effects of expansion wave from the cavity of the ELAC1C as shown in Fig. VI.6. Increasing the separation time to be 0.105 sec. the bow shock of the ELAC1C slightly moves to down close to the EOS nose. Consequently, the expansion waves from the cavity still give more impact on the rear part of the lower surface of the EOS. Further increase of the separation time until reach the maximum separation process provides no longer impact on the lower surface of the EOS, but on the wake region. The lower surface is then wetted by the lower Mach number flow.

2.2.2 Instantaneous Flow Contours at reduced frequency of 0.50

The instantaneous density and Mach number contours for the reduced frequency of 0.50 are given in figure VI.7 and VI.8. The required time to reach the upper condition from the lower condition is 0.115 second standing for that the angular motion of the EOS for this reduced frequency is faster than that of the reduced frequency of 0.22. Consequently, the down wash corresponding to the EOS motion gives a higher impact on the flow around the EOS vehicle. Further, compared to the lower reduced frequency, the locations of shock waves, expansion waves, reflected shock waves and inflection points for the reduced frequency of 0.5 are nearly same as shown in Fig. VI.7. However, the change of flow density in the gap region decreases faster for the reduced frequency of 0.5 compared to that for the reduced frequency of 0.22. In addition, the bow shock wave of the ELAC1C for the reduced frequency of 0.5 is a bit more bent before hitting the EOS bow shock wave compared to that for the lower reduced frequency.

The downwash generated by the EOS motion at the reduced frequency of 0.50 shown in Fig. VI.8 affects flow in the gap region. At the separation time of 0.0 sec. the downwash gives an increase in Mach number compared to the case of reduced frequency of 0.22 in Fig. VI.6.

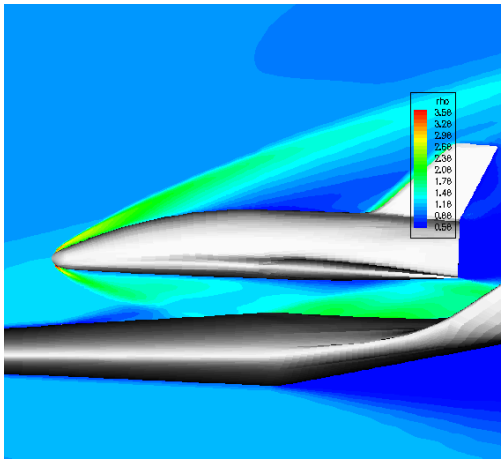

time = 0.000 sec.

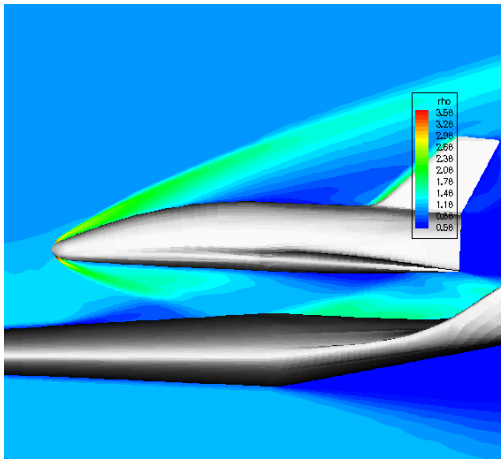

time = 0.023 sec.

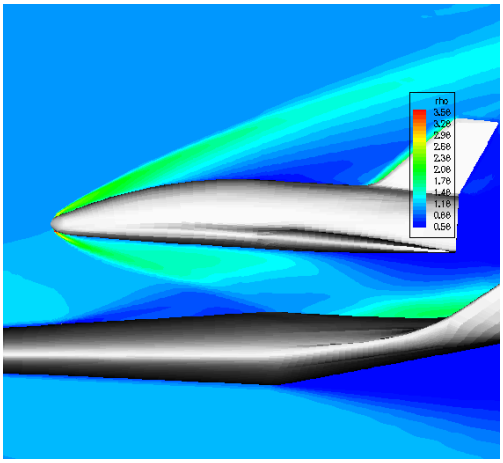

time = 0.046 sec.

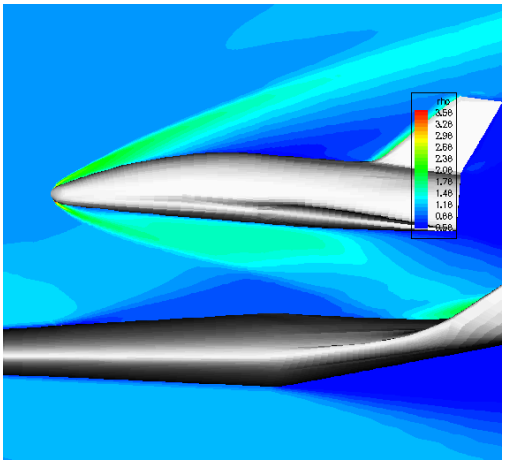

time = 0.069 sec.

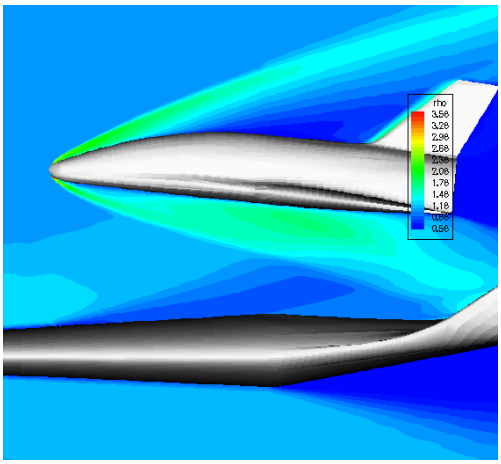

time = 0.092 sec.

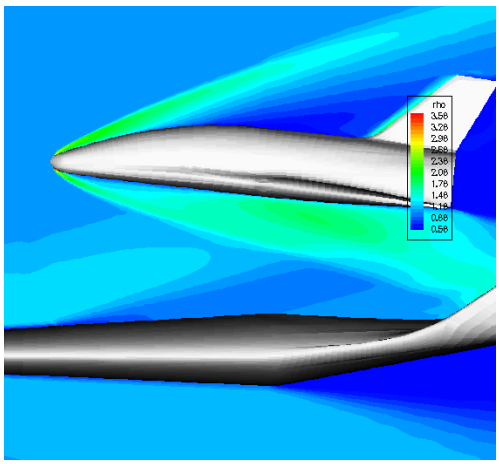

time = 0.115 sec.

Figure VI.7: Instantaneous density contours at six different time levels during separation at M_∞ = 4.04; α = 0.0°; Δα =2.0° - 6.0° deg.; h/l_{EOS} = 0.125-0.325; k_{red} = 0.50.

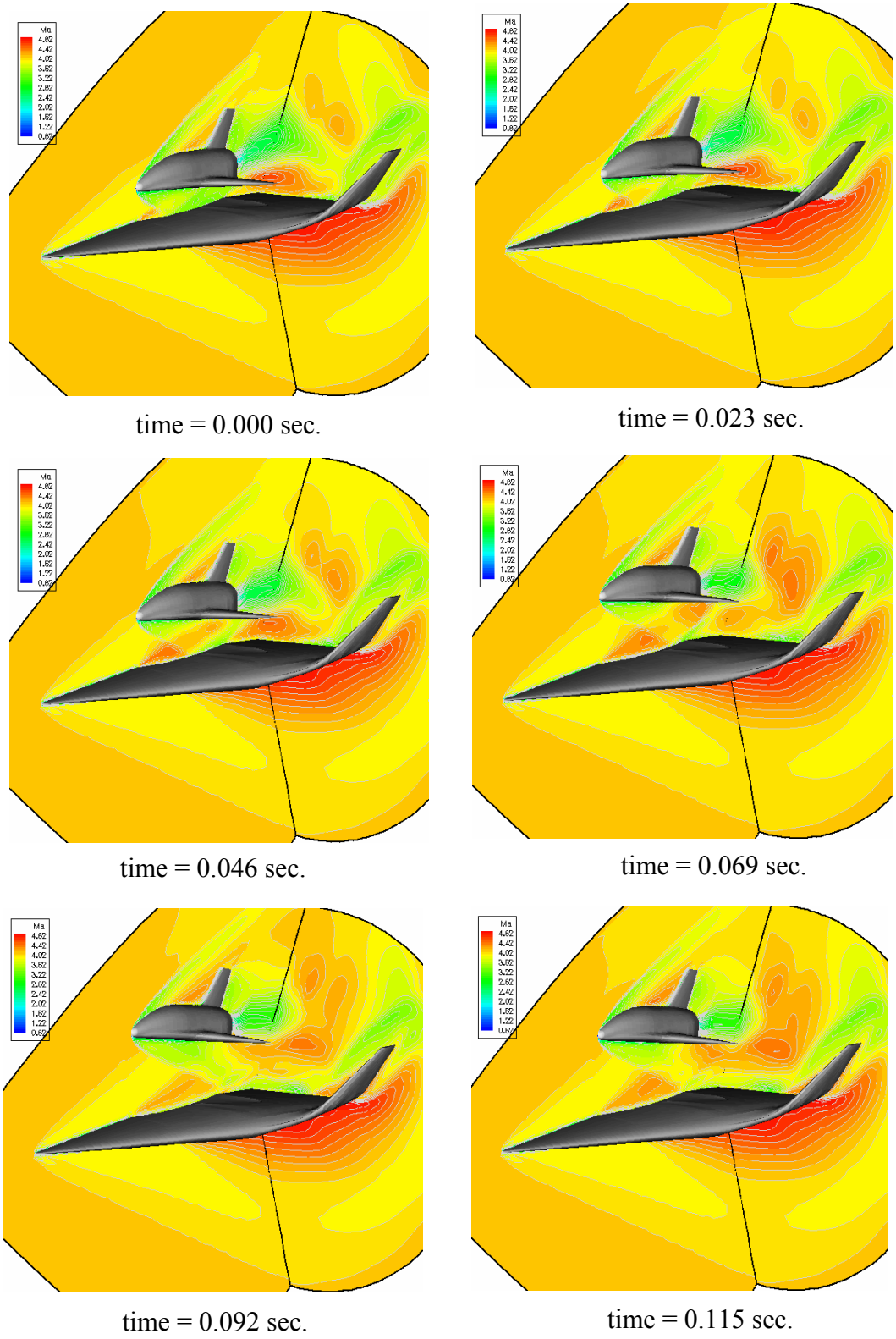

Figure VI.8: Instantaneous Mach contours at six different time levels during separation at M_∞ = 4.04; α = 0.0°; Δα =2.0° - 6.0° deg.; h/l_{EOS} = 0.125-0.325; k_{red} = 0.50.

At the separation times of 0.023 to 0.046, the vertical motion of the EOS for the reduced frequency of 0.5 produce higher downwash affecting the higher increase in Mach number compared to the lower reduced frequency. This gives a higher suction on both the stages causing a decrease in lift coefficient of the EOS and an increase in lift coefficient of the ELAC1C. However, at the higher amplitudes the Mach number in the gap region decreases, but it still higher compared to that of the reduced frequency of 0.22. As a results, the EOS lift coefficient for a reduced frequency of 0.5 at the end position of the separation shown in Fig. VI.3 is slightly higher than that for the lower reduced frequency shown in Fig VI. 2.

2.2.3 Instantaneous Flow Contours at reduced frequency of 1.0

The instantaneous density and Mach number contours for a reduced frequency of 1.00 are shown in Figs. VI.9 and VI.10, respectively. This is the fastest separation manoeuvre simulation with the required time is 0.057 second. Using the same upper and lower limits of the density contour as the previous simulations, the separation at a reduced frequency of 1.00 provides the highest decrease in density compared to the other studied reduced frequencies. The change of the flow density occurs in many regions including the region above the EOS vehicle, in the gap region and the wake region. Again, increasing the reduced frequency does not significantly alter the locations of shock waves, expansion waves, reflected shock waves and inflection points. The curvature of the bow shock wave of the ELAC1C before hitting the EOS bow shock wave highly bent due to an induced flow especially during the middle separation process as shown in Fig. VI.9.

The 3D Mach number contours at a reduced frequency of 1.0 as shown in Fig. VI.10 show increasingly effect of the downwash on the flow field. Such a downwash at the lower amplitudes obtains lower Mach number flow, hence the higher lift coefficient of the EOS is resulted. However, an increase in the amplitude of the separation provides the higher Mach number flow or higher suction flow in the gap region, so that the EOS vehicle subjects to a large amount decrease in the lift coefficient.

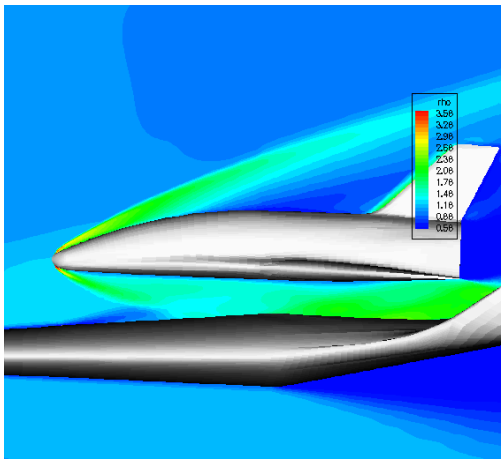

time = 0.000 sec.

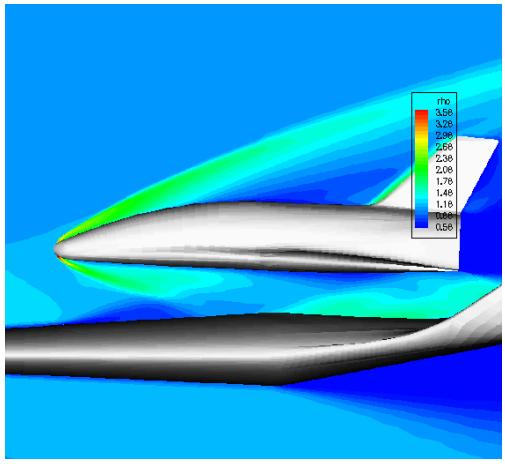

time = 0.013 sec.

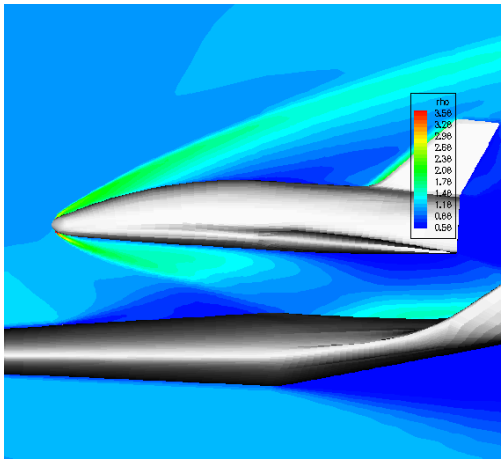

time = 0.026 sec.

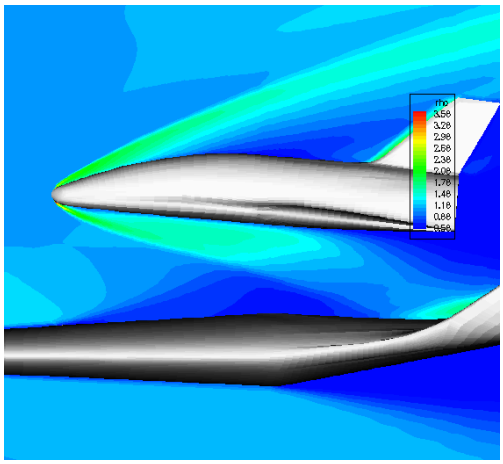

time = 0.039 sec.

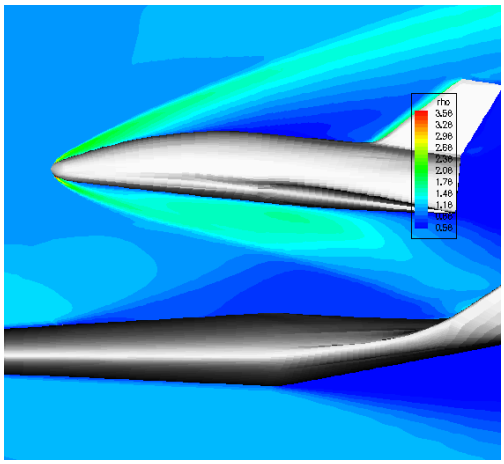

time = 0.052 sec.

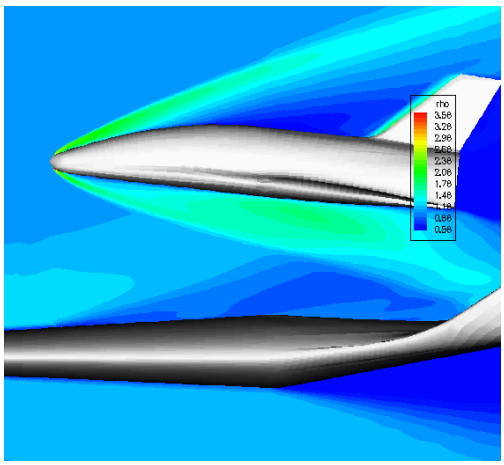

time = 0.064 sec.

Figure VI.9: Instantaneous density contours at six different time levels during separation at M_∞ = 4.04; α = 0.0°; Δα =2.0° - 6.0°; h/l_{EOS} = 0.125-0.325; k_{red} =1.00.

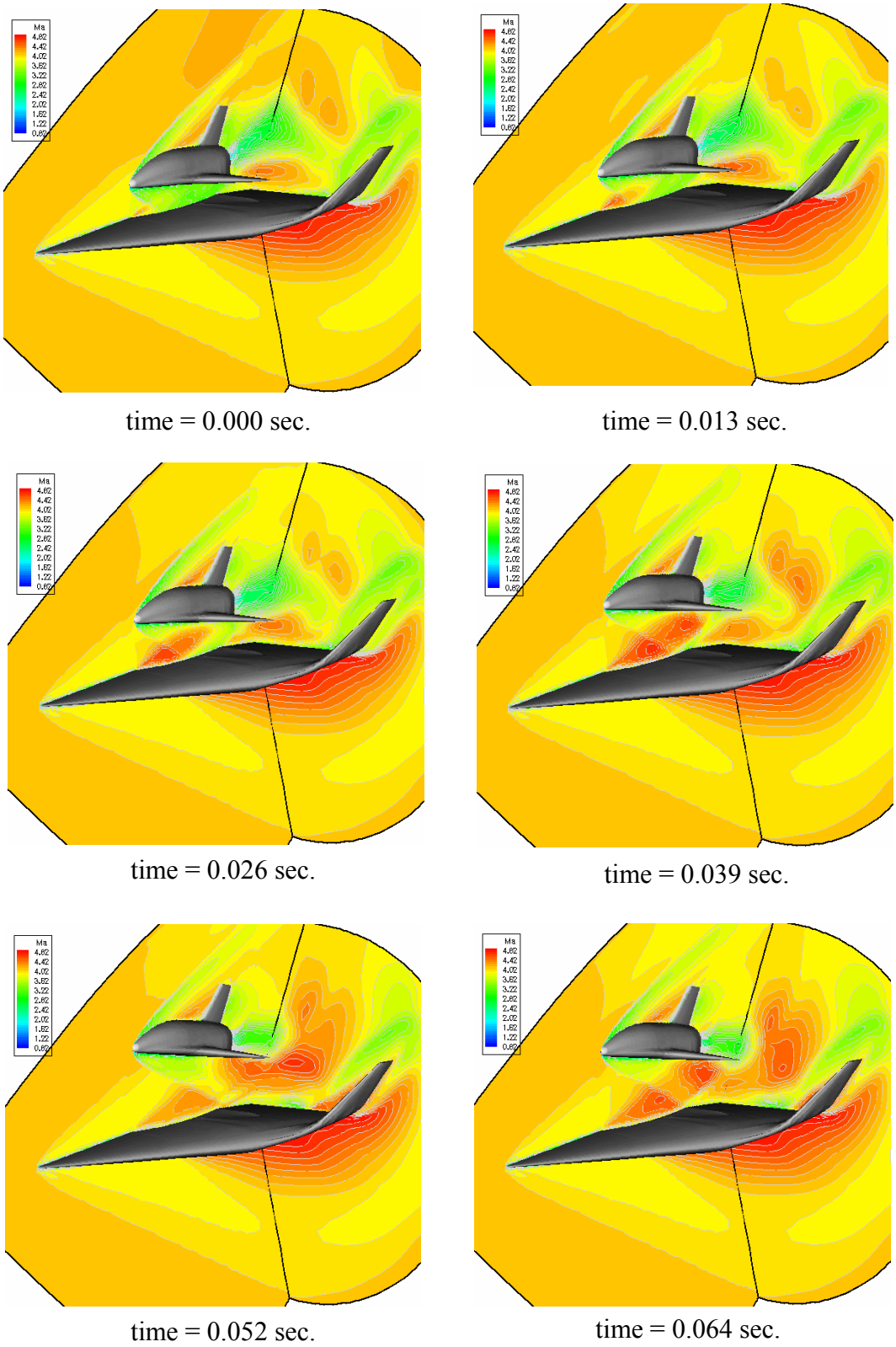

Figure VI.10: Instantaneous Mach contours at six different time levels during separation at M_∞ = 4.04; α = 0.0°; Δα =2.0° - 6.0°.; h/l_{EOS} = 0.125-0.325; k_{red} = 1.00.

The further increase amplitude to the end position, the Mach number generated by the expansion wave from the cavity of the ELAC1C vehicle slightly decreases.

2.3 Comparison between the Steady and Unsteady State Solution

Figures VI.11 show the comparison of aerodynamic characteristics for the various reduced frequencies at a free stream Mach number, M_∞ = 4.04 with angle of attack of the ELAC1C, α = 0.0 deg, the orbital stage angle of attack, $\Delta\alpha$ = 0.0 deg. and the separation distance, h/l_{EOS} = 0.225. The reduced frequency equal to zero describes that the flow is alike the steady condition because the downwash is equal to zero.

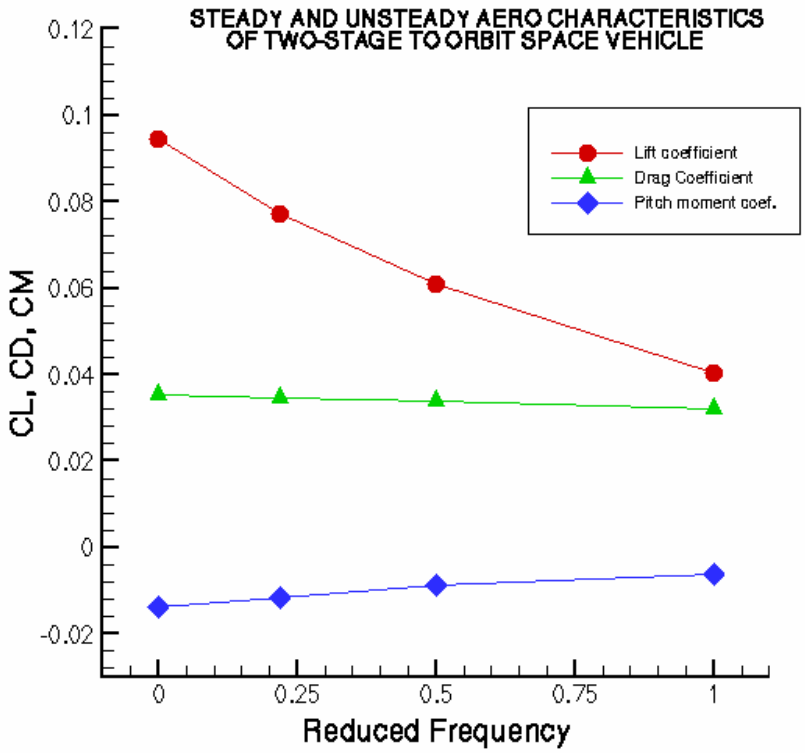

Figure VI.11: Comparison of aerodynamic characteristics of steady and unsteady flows for various reduced frequencies at M_∞ = 4.04, α= 0.0°, $\Delta\alpha$ = 4 .0°, and h/l_{EOS} = 0.225.

Increasing the reduced frequency gives the decreased lift coefficient of the EOS at the middle position of the separation. Compared to the steady state solution, the lift coefficient at the highest reduced frequency, namely k_{red} = 1.00 decreases from 0.1 to 0.039. At the higher reduced frequency, the decrease of the EOS lift during the separation manoeuvre should be taken into account. The down wash effect does not significantly affect on the drag coefficient. The drag coefficient of EOS at a reduced frequency of 1.0 is almost same as the drag coefficient of the steady state solution. Increasing the reduced frequency of the EOS yields the significant decrease in the magnitude of the pitching moment.

Figures VI.12 show the contours of density for the steady and unsteady cases at various reduced frequencies, namely k_{red} = 0.0, 0.22, 0.5, and 1.0.

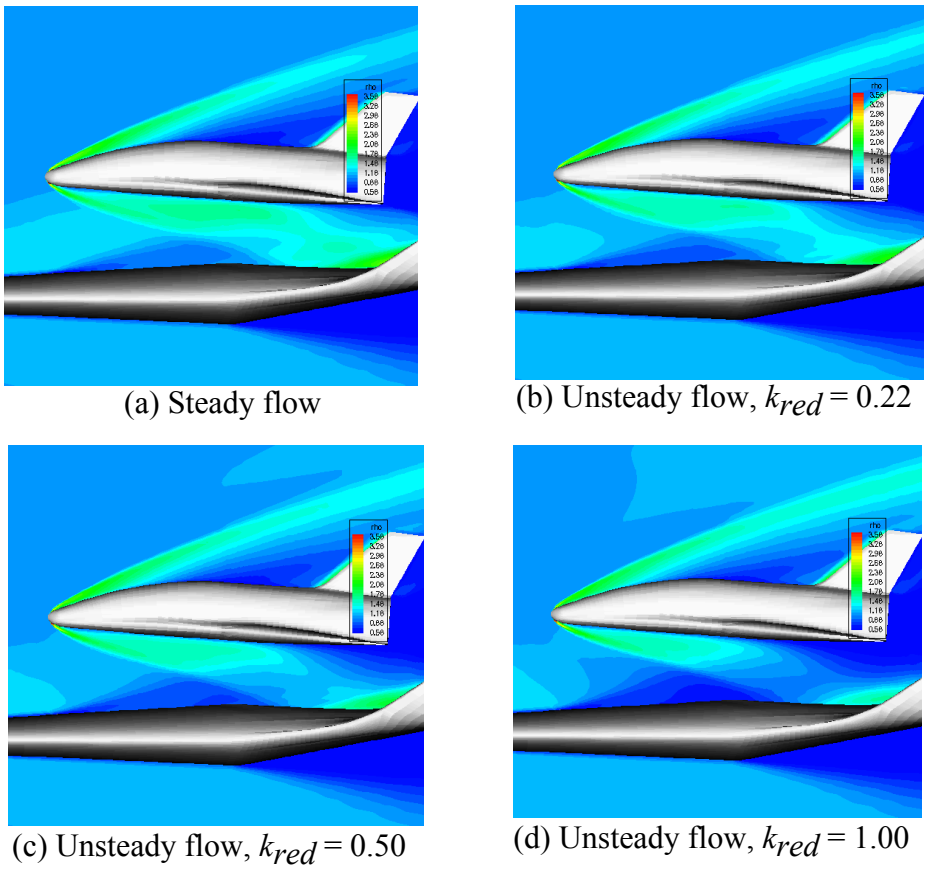

(a) Steady flow

(b) Unsteady flow, k_{red} = 0.22

(c) Unsteady flow, k_{red} = 0.50

(d) Unsteady flow, k_{red} = 1.00

Figure VI.12: Comparison of density contours of steady and unsteady flows at M_∞ = 4.04, α = 0.0°, $\Delta\alpha$ = 4.0°, h/l_{EOS} = 0.225.

Compared to the steady solution, the effect of downwash is clearly indicated by the bending line of the bow shock wave. It also affects flow features in the region above of EOS and in the gap region as shown in Fig. VI.12.

Mach contours for the steady and unsteady cases at various reduced frequencies, namely k_{red} = 0.0, 0.22, 0.5, and 1.0 are shown in Fig. VI.13 The effect of the downwash provides an increase of flow speed in the gap region. This gives a suction effect on both the vehicle stages. However, the effect of induced flow does not give a significant impact to the flow under the ELAC vehicle.

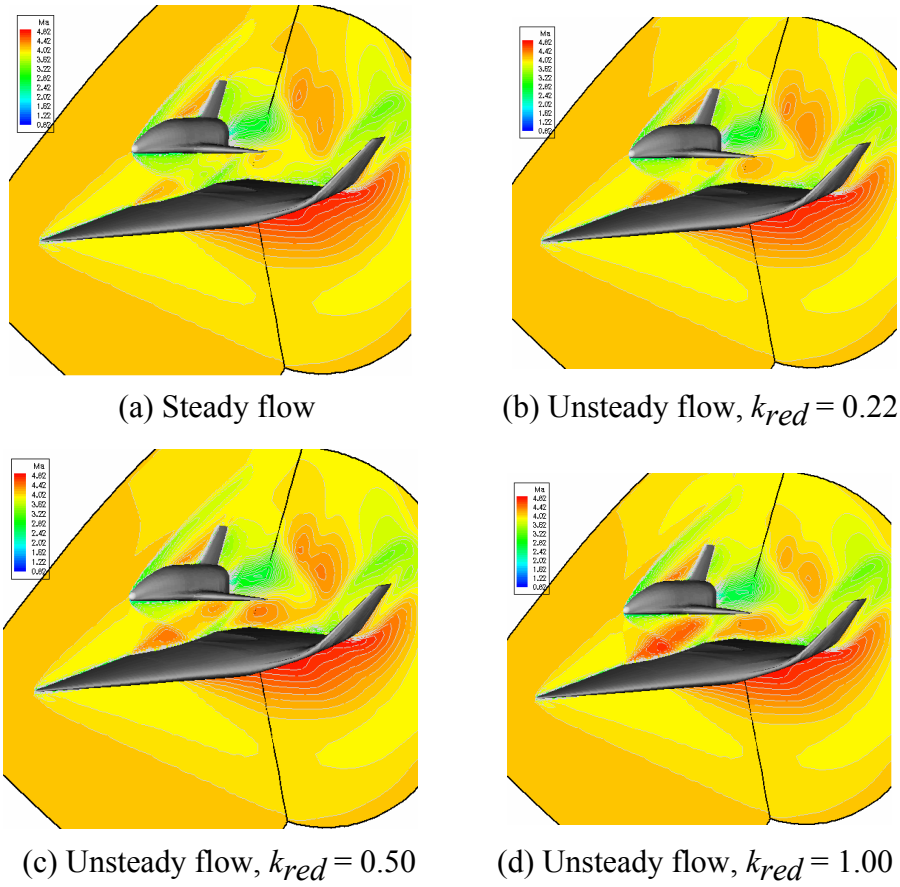

(a) Steady flow (b) Unsteady flow, k_{red} = 0.22

(c) Unsteady flow, k_{red} = 0.50 (d) Unsteady flow, k_{red} = 1.00

Figure VI.13: Comparison of Mach number contours of steady and unsteady flows at M_∞ = 4.04, α = 0.0°, $\Delta\alpha$ = 4.0°, h/l_{EOS} = 0.225.

- **Lift coefficient versus amplitude of steady and unsteady state solutions**

  Figure VI.14 shows the graphs of lift coefficient versus amplitude for the steady and unsteady flows of the EOS vehicle. The amplitude includes the orbital stage angle of attack and separation distance between the stages which change simultaneously. In this figure, the steady flow solutions are computed for three different conditions including the lower, middle, and upper positions.

  Compared to the steady state solution, at the lower position, the effect of downwash provides the additional lift of the EOS. This is caused the downwash inducing a deceleration of the flow in the gap region as shown in Fig VI.10. But, at the moderate and higher amplitudes the downwash cause a decrease in lift coefficient of the EOS. This may due to at the larger gap the downwash gives reciprocal effects on expansion waves generated by the cavity of the ELAC1C vehicle. In addition, the lift coefficient at the lower reduced frequencies is closer to the steady state solution.

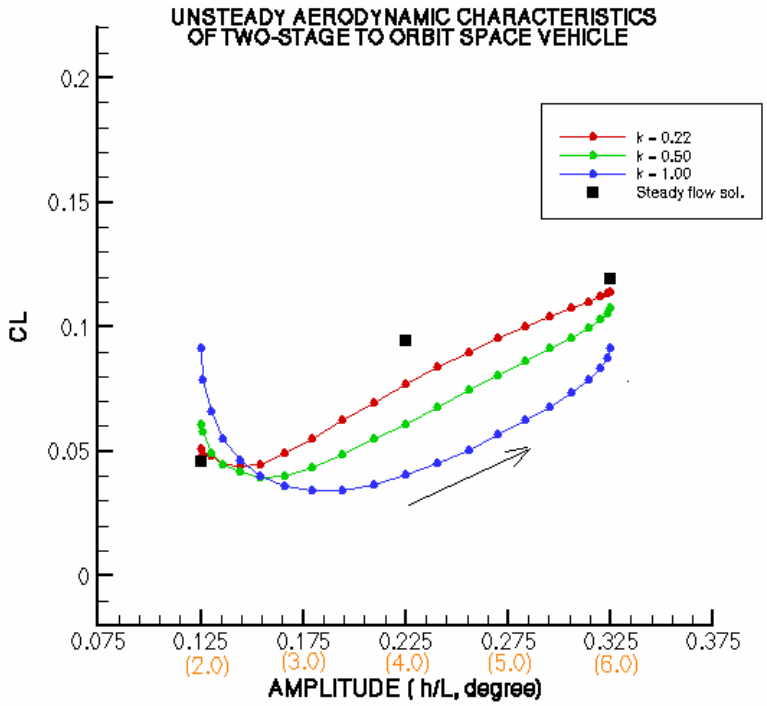

Figure VI.14: Graphs of lift coefficient versus amplitude for various reduced frequencies (M_∞ = 4.04; α = 0.0°)

- **Drag coefficient versus amplitude of steady and unsteady state solutions**
  The graphs of drag coefficient versus amplitudes for the steady and unsteady flows of the EOS vehicle at the various reduced frequencies are depicted in Fig. VI.15. The vehicle drag is mainly contributed by shock waves occurred in the flow field. The unsteady drag coefficient at the same reduced frequency has the similar trend to the unsteady lift coefficient. At the lower position, the downwash effect contributes an additional drag coefficient. The extra drag coefficient becomes higher with increasing the reduced frequency. However, at the moderate and higher amplitudes, the downwash cause a decrease in the drag coefficient. This is due to the contribution of the expansion wave generated by the cavity of the ELAC1C vehicle increases and the reflected shock wave decreases. Further increase of amplitude the effect of the bow shock of the EOS increases, hence the drag increase again as shown in Fig. VI.15. In addition, the drag coefficient for the lower reduced frequencies is closer to the steady state solution.

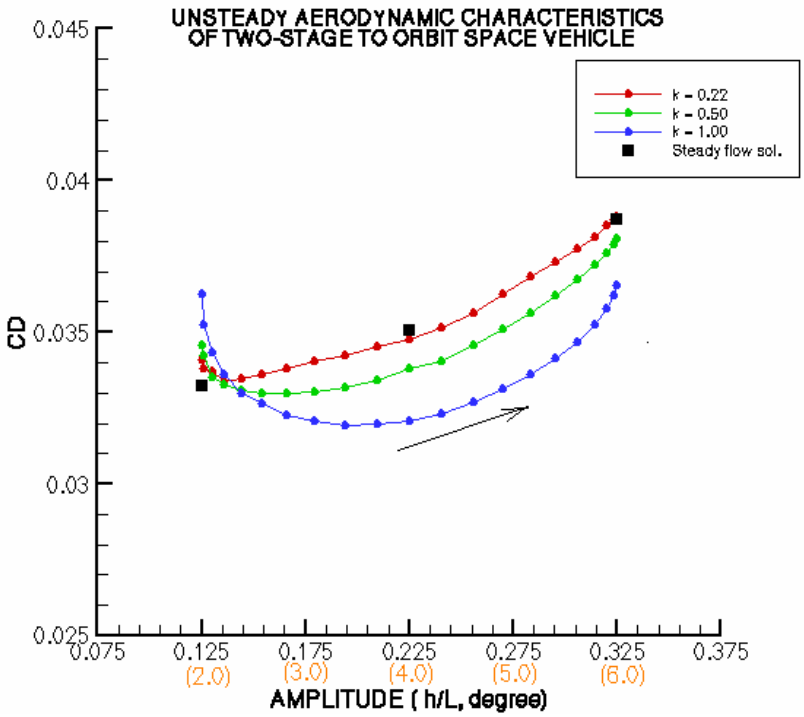

Figure VI.15: Graphs of drag coefficient versus amplitude for various reduced frequencies (M_∞ = 4.04, α = 0.0°.).

- **Pitching moment coefficient versus amplitude**

  The comparison of the steady and unsteady pitching moment coefficients are shown in the graph of Fig.VI.16. The values of the pitching moment coefficients for all amplitudes of the separation are negative. The pitching moment coefficient becomes less negative with the increased amplitude and then before reaching the middle position the pitching moment coefficient becomes more negative with a further increase in the amplitude.

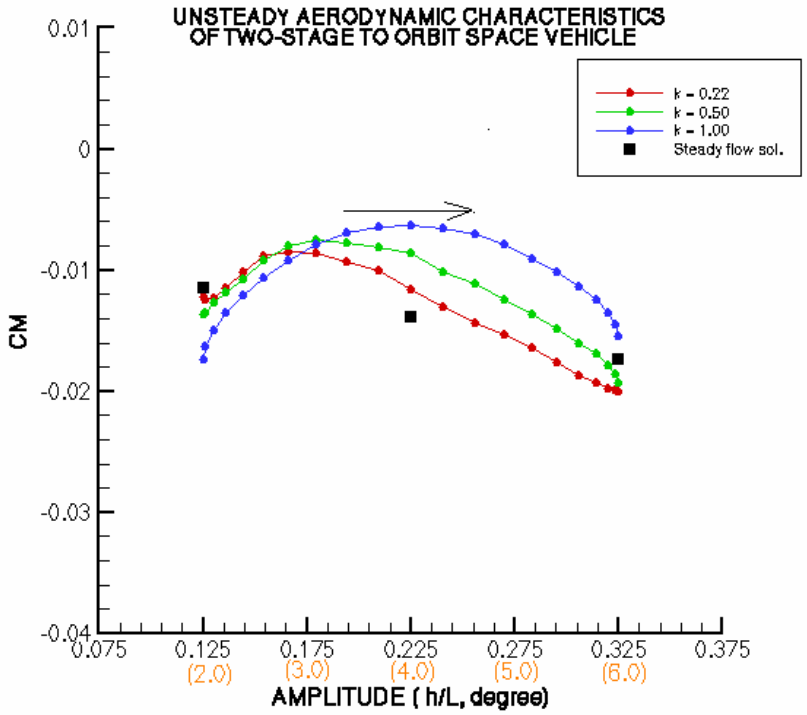

Figure VI.16: Graphs of pitching moment coefficient versus amplitude for various reduced frequencies ($M_\infty = 4.04$, $\alpha = 0.0°$).

At the lower position, the downwash causes the EOS pitching moment coefficient becomes more negative. At higher reduced frequency the pitching moment of EOS increases in a negative value. While, the pitching moment coefficient becomes less negative due to the downwash contribution at the moderate and higher amplitudes.

CHAPTER VII
CONCLUSIONS AND RECOMMENDATIONS

The main goal of this research is to investigate effects of the stage separation manoeuvre on aerodynamics of a TSTO space transportation system using computational method. For this purpose, two different space configurations, namely a simplified (flat plate) and full carrier stage (ELAC 1C) each linked to the orbital stage (EOS) have been employed. To acquire flow solutions in the flow field around the configurations, the three-dimensional unsteady Euler equations are solved using the finite volume method for spatial discretization and the explicit scheme of the first order Runge-Kutta scheme for the temporal discretization. The flux vectors between volumes are computed using the modified AUSM method combined with the MUSLE approach to guarantee higher order accuracy in the spatial domain. The computation accuracy and efficiency are examined by studying the effects of numerical factors including grid density and grid smoothing on flow solution in steady state using the simpler configuration, namely the EOS - flat plate. For the validation of the simulation method, the computational results are compared to the corresponding experimental data at various conditions for both the configuration. As a core research, the calculations of the unsteady stage separation are conducted to simulate the real flow phenomena during the separation manoeuvre for the full configuration.

The calculation steps, namely generating topology and mesh, improving the grid quality and obtaining the flow solution are conducted. Also for the unsteady simulation, moving grids corresponding to the motion of the orbital stage are generated using the dynamic mesh generator. For the initial mesh generation, multi block structured meshes are obtained using the algebraic transfinite interpolation method in the ICEMCFD. The improvement of the grid quality is then performed to achieve orthogonal grids using the solution of Poisson and Laplace equations.

In total, for all computed configuration models, 14 steady state cases are analyzed due to the variations of Mach number, angle of attack, the orbital stage angle of attack and separation distance between stages. In addition, 3 unsteady cases are evaluated due to the variations of reduced frequency changing simultaneously the separation distance between the carrier and orbital stage and the orbital stage angle of attack.

The effects of the grid smoothing improves the grid quality to be orthogonal that yields a more fast convergent solution (higher computation efficiency) and provides a more sharper shock wave line (more accurate solution). In addition, the further improvement of the solution accuracy can be obtained by increasing the grid density, but it must be taken into account for the memory space and computational time.

The simulations for both the configurations can be accomplished with good to excellent agreement to the experimental values. The quality of smoothed meshes is good and fit to the Euler solver (FLMEu solver), and this solver has been proved to be very stable in simulating the separation problem. The comparison of the computational results to the experimental results indicates that the flow solver can provide simulations of the hypersonic space transportation system aerodynamics on reasonable to high accuracy level.

Substantiated by the unsteady aerodynamic characteristics, unsteadiness must be carefully considered in the beginning of the separation manoeuvre when the orbital stage lift decreases. In addition, the drag coefficient of the orbital stage slightly decreases with increasing the separation distance from the carrier stage. The pitching moment coefficient decreases followed by an increase of nose down magnitude with increasing distance and the orbital stage angle of attack which has to be carefully addressed in the flight control system.

For future research, further investigation of the separation process of the space transportation system considers a supporting mechanism to elevate the orbital stage from a position closer to the carrier stage into a position of a full stand of the mechanism. It is intended to initially shift the orbital stage to a position that the separation process progresses safely and efficiently. In addition, when the distance between the orbital and carrier stages is closed the viscous effects in the gap region can not be ignored again. Therefore, the simulation of unsteady viscous of the TSTO space transportation system also becomes a more interest topic. For this, the solution of Navier-Stokes equations, such as Reynolds Averaged Navier-Stokes (RANS) with employing an appropriate turbulent model for the hypersonic flow is necessary to investigate.

REFERENCES

1. Russo, G. (2002), Next Generation Space Transportation System, *Aerotecnica Missili e Spazio*, Vol. **81**, 65 – 72.

2. Kuczera, H., H. Hauck, P. Krammer, P.W. Sacher (1993), The German hypersonic technology programme, *IAF-93-V.4.629*, Graz, Austria.

3. Maita, M., H. Kubota (1998), Japanese space plan/ RLV program, *8th AIAA International Aerospace Planes and Hypersonic System and Technologies Conference*, Norkfolk, VA.

4. GAO (2002), Space transportation challenges facing NASA's space launch initiative, Report to the Subcommittee on Space and Aeronautics, Committee on Science, House of Representative.

5. Yanagihara, M., T. Munenaga (2004), High-speed flight demonstration project, *24th International Congress of the Aeronautical Sciences (ICAS)*, Japan, 711.1 – 10.

6. Hirschel, E.H. (1996), The technology development and verification concept of the German hypersonic program. Aerothermodynamics and propulsion integration for hypersonic vehicles. *AGARD-R-813*, 12.1 – 15.

7. Decker, K. (2003), *Aerodynamik eines zweistufigen Raumtransportsystems beim Wiedereintritt und während der Separation*, Dissertation, Technische Universität München.

8. Laschka, B., C. Breitsamter (2001), Instationäre Hyperschallströmungen – Zwei – und drei dimensionale Berechnungsmethoden, Transatmosphärische Flugsysteme, Grundlagen der Aerothermodynamik, Antriebe und Flugmechanik, Teilprojekt A1, Arbeit- und Ergebnisbericht, *Sonderforschungsbereich 255*.

9. Moelyadi, M.A, C. Breitsamter, B. Laschka (2004), Steady and unsteady calculations on full configuration of two-stage space transportation system during separation, *24th International Congress of the Aeronautical Sciences (ICAS)*, Japan, 222.1 – 12.

10. Connolly, A. (2004) : The final flight of X-43A, http://www.amtech-usa.org/a5/news/110804_x43aFinal.pdf.

11. Kharitonov, A., M. Brodetsky, L. Vasenyov, L. Adamov, C. Breitsamter, M. Heller (2000), Investigation of aerodynamic characteristic of the models of a two-stage aerospace system during separation, *Final Report*, Institute of Theoretical and Applied Mechanics, Russia, and Technische Universität München.

12. Glößner, C. (2001), Druck- und Wärmestromverteilung und aerodynamische Beiwerte auftriebsgestützter Wiedereintrittskörper, Arbeits- und Ergebnisbericht, *Sonderforschungsbereich 253*.

13. Weiland, C. (1996), Stage separation aerodynamics, Aerothermodynamics and Propulsion Integration for Hypersonic Vehicles, *R-813, AGARD*, 11.1 – 27.

14. Schröder, W., R. Behr, S. Menne (1993) , Analysis of hypersonic flows around space transportation system via CFD methods," *AIAA-93-5067*.

15. Cvrlje, T., C. Breitsamter, C. Weishäupl, B. Laschka (2000), Euler and Navier-stokes simulations of two-stage hypersonic vehicle longitudinal motions, *J. Spacecraft and* Rockets, Vol. **37**, No.**2**, 242 – 251.

16. Cvrlje, T., C. Breitsamter, B. Laschka (1999), Unsteady and coupling aerodynamic effects on the lateral motion in hypersonic flight, *AIAA-99-4832, 9th International Space Planes and Hypersonic Systems and Technologies conference*.

17. Rochholz, H., T. Huber, F. Matyas (1995), Unsteady airloads during separation of an idealized two-stage hypersonic vehicle, „ Zeitchrift für Flugwissenschaften und Weltraumforchung, Band **19**, Heft **1**, 2 – 9.

18. Anderson, J.D. (1989), *Hypersonic and High Temperature Gas Dynamic*, New York: Mc Graw-Hill Book Company, 166 - 334.

19. Anderson, J.D.(1991) , *Fundamentals of Aerodynamics*, second edition, McGraw Hill, New York.

20. Dolling, D.S. (1990), Unsteadiness of supersonic and hypersonic shock induced turbulent boundary layer separation, *AGARD-R-764, Ch. 7, Special Course on Three Dimensional Supersonic/Hypersonic Flow Including Separation*.

21. Decker, J.P. (1969), Aerodynamic interference effects caused by parallel-staged simple configurations at mach numbers of 3 and 6, *NASA TN D-5379*.

22. Bernot, P.T. (1975), Abort separation study of a shuttle orbiter and external tank at hypersonic speed, *NASA TM X-3212*.

23. Bonnefond, T., N.P. Adamov, M.D. Brodetsky, L.G. Vasenyov, E.K. Derunov, A.M. Kharitonov (1996), An experimental investigation of aerodynamic interference of ssto winged during separation, *J. Thermophysics and Aeromechanic*s, Vol. **3**.

24. Bonnefond, T., A.M. Kharitonov, M.D. Brodetsky, L.G. Vasenyov, N.P. Adamov, E.K. Derunov (1995), Separation of winged vehicles in supersonic, *AIAA-95-6092, 6th International Aerospace Planes and Hypersonic Technologies Conference*.

25. Anderson, J.D. (1982), *Modern Compressible Flow*, Chapter 7, Mc Graw-Hill Book Company, New York, 172 - 205.

26. Mukovozov, M.V.," Method for determining interference components of aerodynamic characteristics of aircrafts integrated with a body of revolution at mach 3 and 6," *Applied Problem of Aeromechanics and Geo-Cosmic Physics,* Moscow, 1990, 73 – 80.

27. Brenner, P. (1993), Numerical simulation of three dimensional and unsteady aerodynamics about bodies in relative motion applied to a ssto separation, *AIAA-93-5142*.

28. Meakin, R., N. Suhs (1989), Unsteady aerodynamic simulation of multiple bodies in relative motion, *AIAA 89-1996*.

29. Decker, K, B. Laschka (2001), Unsteady aerodynamic of a hypersonic vehicle during a separation phase, *AIAA-2001-1852*.

30. Spekreijse, S.P. (1999), Elliptic generation system, *Handbook of Grid Generation* (Thompson, J. F., et al.), CRC Press LLC, Ch.4, 1 – 29.

31. Liseikin, V.D. (1999), *Grid Generation Method,* Scientific Computation, Springer, Berlin, 1-20, 156 – 180

32. Hirsch, C. (1995), *Numerical Computation of Internal and External Flows, Fundamentals of Numerical Discretisation*, Vol.**1**, New York: John Wiley and Sons Ltd, New York.

33. Blazek, J. (2001), *Computational Fluid Dynamics: Principle and Applications*, Ch. 3, 4, 6, 10, Elvisier Ltd, United Kingdom.

34. Anderson, J,D. (1995), Computational Fluid Dynamics, MCGraw Hill, New York.

35. Liou, M.-S. (1996), A sequel to AUSM: AUSM+, *Journal of Computational Physics*, **129**, 364 – 382

36. Liou, M.-S. (1995), Progress towards an improved CFD method – AUSM+, *AIAA Paper 95-1701*.

37. Jameson, A., W. Schmidt, E. Turkel (1981), Numerical simulation of the Euler equation by finite volume methods using Runge-Kutta time stepping schemes, *AIAA Paper 81-1259*

38. Jameson, A. (1991), Time dependent calculations using multigrid, with applications to unsteady flow past airfoils and wings, *AIAA Paper 91-1596*.

39. Cvrlje, T. (2001), *Instationäre Aerodynamik des Separationsvorgangs zwischen Träger und Orbiter*, Dissertation, Technische Universität München.

40. Pranata, B.B. (1999), *Physical and numerical aspects of aeronautics simulations*, Dissertation, Delft University of Technology, 1999.

41. Hirsch, C. (1995), *Numerical Computation of Internal and External Flows,* Vol.**2**, New York: John Wiley and Sons Ltd, New York.

42. Moretti, G., M. Abbet (1996), A time dependent computational method for blunt-body flows," *AIAA Journal*, vol. **4**, no.**12**, 2136 – 2141.

43. Moelyadi, M.A, L. Jiang, C. Breitsamter (2005), Investigation of steady and unsteady flow characteristics of space transport system during separation, 13th AIAA/CIRA Conference, Italy, (AIAA Paper 05 – 3248).

44. Sach, G., J. Drexler, W. Schoder, (1993), Optimal Separation and Ascent of Lifting Upper Stages, Lectures Notes in Engineering, Springer-Verlag, 1993, 325-331.

45. Breitsamter, C., Simulation parameters of stage separation – Flug Mechanik, Internal Communication Document, SFB 255.

46. Lasckha, B. (1999), Grundlagen der stationären und instationären Strömungen, *Vorlesungsskript*.

47. Moelyadi, M..A. (2002), CFD simulations on aerodynamic characteristics of the ASTRA space transportation system vehicle, Research Report, ASTRA-FLM-TUM-PR-002.

48. Struijs, R., H. Deconinck, P. de Palma, P.L. Roe, K.G. Powell (1991), Progress on multidimensional upwind Euler solvers for unstructured grids, *AIAA Paper 91-1550*.

49. Rossow, C..-C. (1992), Efficient Computation of Invisicd Flow Fields Around Complex Configurations Using a Multiblocks Multigrid Method, *Comm. in Appl. Num. Methods*, **8**, 735 – 747.

50. Kassies, A., R. Tonaccini (1990), Boundary conditions for Euler equations at internal block faces of multi-block domains using local grid refinement, *AIAA paper 90-1590.*

51. Rai, M.M. (1986), A conservative treatment of zonal boundaries for Euler equation calculations, *Journal of Computational Physics*, **62**, 472 – 503.

52. Liseikin, V.D. (1999), *Grid Generation Method,* Scientific Computation, Springer, Berlin, 1-20, 156 – 180.

53. Ericsson, L.E (1982), Generation of boundary-conforming grids around wing-body configuration using transfinite interpolation, *AIAA Journal*, Vol. **20**, **10**, 1313-1320.

54. Swanson, R.C., E. Turkel (1997), On central-difference and Upwind Schemes, *Upwind and High-Resolution Schemes* (Hussaini, M.Y., et al.), Springer-Verlag, Ch.II, 167-181.

55. Steger, J.L., R.F. Warming (1981), Flux-vector splitting of the inviscid gasdynamic equations with application to finite difference methods, *Journal of Computational Physics*, **40**, 263 – 293.

56. Steger, J.L., R.F., Warming (1978), Implicit finite-difference simulation of flow about arbitrary two-dimensional geometries, *AIAA Journal*, **16(7)**, 679 – 686.

57. Van Leer, B. (1982), Flux-vector splitting for the Euler equations, *Proc. 8th Int. Conf. on Numerical Methods in Fluid Dynamics,* Springer Verlag, 507 – 512.

58. Oscher, S., F. Salomon (1982), Upwind difference schemes for hyperbolic systems of conservation laws. *Math. Comp*., **38**, 339 – 374.

59. Roe, P.L. (1981), Approximate Riemann solvers, parameter vectors, and difference schemes, *Journal of Computational Physics*, **43**, 357 – 372.

60. Harten, A. (1983), high resolution scheme for hyperbolic conservation laws, *Journal of Computational Physics,* **49**,. 357 – 393.

61. Liou , M.S., C. J. Jr. Steffen (1993), A new splitting scheme, *Journal of Computational Physics*, **103**, 23 – 39.

62. Wada, Y., M.S: Liou.(1994), A Flux-splitting scheme with higher resolution and robustness for discontinuities, *AIAA Paper 94-0083*.

63. Tatsumi, S., L. Martinelli, A. Jameson (1995), A new high resolution scheme for compressible viscous flow with shocks, *AIAA Paper 95-0466.*

64. Edwards, J.R. (1997), A Low-diffusion flux-splitting for Navier-Stokes calculations, *Computer & Fluids*, **26**, 653 – 659.

65. Rossow, C.-C. (1998), A simple flux-splitting scheme for compressible flows, *Proc. 11th DGLR-Fach Symposium,* Berlin, Germany.

66. Rossow, C.-C. (1985), A flux-splitting scheme for compressible and incompressible flows, *AIAA Paper 85-1680.*

67. Hänel, D., R. Schwane (1989), An implicit flux-vector scheme for the computation of viscous hypersonic flows, *AIAA Paper 89-0274*.

68. Liou, M.S. (1992), On a new class of flux splittings, *in Lecture Notes in Physics*, Vol. **414**, Springer Verlag, Berlin, 115-130.

69. Coquel, F. and Liou, M.S. (1992), Stable and low diffusive hybrid upwind splitting methods, *in Proceedings, 1st European CFD Conference*, Brussel.

70. Radespiel R., N. Kroll (1995), Accurate flux vector splitting for shock and shear layers, *Journal of Computational Physics*, Vol. **121**, 66 – 78.

71. Van Leer, B. (1979), Towards the ultimate conservative difference scheme V. a second order sequel to Gudonov's method, J. Computational Physics, 127, 380 – 397.

72. Kreiselmaier, E., *Berechnung instationärer Tragflügelumströmungen auf der Basis der zeitlinearisierten Eulergleichungen*, Dissertation, Technische Universität München, 1998.

73. Van Albada, G.D, B. Van Leer, W.W. Roberts (1982), A comparative study of computational methods in cosmic gasdynamics, Astronomy and Astrophysics, 108, 76 – 84.

74. Mazaheri, K., P.L. Roe (1997), Numerical wave propagation and steady-state solutions: soft wall and outer boundary conditions, *AIAA Journal*, **35**, 965 – 975.

75. Hayder, M.E., F.Q. Hu, M.Y. Hussaini 1997), Towards perfectly absorbing boundary conditions for Euler equations, *ICASE Report* No. 97-25.

76. Whitfield, D.L., J.M. Janus (1984), Three-dimensional unsteady Euler equations solution using flux vector splitting, *AIAA paper 84-1552*.

77. Pulliam, T.H.(1986), Artificial dissipation models for the Euler equations, *AIAA Journal* , **24** , 1931-1940.

78. Habermann, M., H. Olivier (2000), Upgrade of the Aachen shock tunnel with a detonation driver shock wave laboratory, I*CMAR 2000*, in Novosibirsk, Russia.

79. Breitsamter, C. (2003), Aerodynamic High-Speed Measurements on EOS / Flat Plate Configuration, ITAM reference measurements on EOS/Flat plate interference.

80. ICEM CFD Engineering (2002), *Meshing Tutorial Manual*.

81. Pracht, W.E. (1975), Calculating three-dimensional fluid flows at all speeds with an Eulerian-Lagrangian computing mesh, *J. Computational Physics*, **14**, 132 – 159.

82. Parpia, I. (1988), Van Leer flux vector splitting in moving coordinates, *AIAA Journal*, **26**, 113 – 115.

83. Gaitonde, A.L (1994), A dual-time method for the solution of the unsteady Euler equations, *Aeronautical Journal*, October, pp. 283-291.

84. Anderson, W.K., JL. Thomas, C.L. Rumsey (1987), Extension and applications of flux vector splitting to unsteady calculations on dynamic meshes, *AIAA Paper 87-1152*.

85. Batina, J.T. (1989), Unsteady Euler airfoil solutions using unstructured dynamic meshes, AIAA Paper 89-0115.

86. Thomas, P.D., C.K. Lombard (1979), Geometry Conservation Law and its applications to flow computations on moving grids, *AIAA Journal*, **17**, 1030 – 1037.

87. Guillard, H., C. Farhat (1999), On the significance of the GCL for flow computations on moving meshes, *AIAA Paper 99-0793*.

88. Koobus, B, C. Farhat (1998), Second-order schemes that satisfy the GCL for flow computations on dynamic grids, AIAA Paper 98-0113.

89. Tamura, Y., K. Fujii (1993), Conservations Law for moving and transformed grids, *AIAA Paper 93-3365*.

90. Gordon, W.N., C.A. Hall (1973), Construction of curvilinear coordinate systems and application to mesh generation, *International J. Num. Methods in Eng*., Vol. 7, pp. 461-477.

91. Smith, R.E. (1999), Transfinite interpolation generation systems, *Handbook of Grid Generation* (Thompson, J. F., et al.), CRC Press LLC, Ch.3, 1 – 15.

92. Einfeldt, B. (1988), On Gudonov-type methods for gas dynamics, *SIAM J. Num. Anal.* Vol. **25**, **2.**

APPENDIX A
CONSERVATIVE DIFFERENTIAL FORM OF EULER EQUATION

The Euler equations in a moving finite control volume Ω with S as the boundary can be written as

$$\frac{\partial}{\partial t}\iiint_{\Omega} \mathbf{q}\, d\Omega + \iint_{S}\left[\mathbf{f}\cdot n_x + \mathbf{g}\cdot n_y + \mathbf{h}\cdot n_z\right]dS = 0 \qquad \text{(A.1)}$$

In order to obtain differential form of the Euler equation, all variables in the first and second terms of Eq. (A.1) are first taken inside the integral. For the first term of Eq. (A.1), by assuming the volume integration is fixed in space the time derivative can be moved inside the integral, that is

$$\frac{\partial}{\partial t}\iiint_{\Omega} \mathrm{q}\, d\Omega = \iiint_{\Omega} \frac{\partial}{\partial t}(\mathrm{q})\, d\Omega \qquad \text{(A.2)}$$

Further, the surface integral in the second term of Eq. (A.1) can be converted into a volume integral by applying Gauss's theorem as follows

$$\iint_{S}\left[\mathbf{f}\cdot n_x + \mathbf{g}\cdot n_y + \mathbf{h}\cdot n_z\right]dS = \iiint_{\Omega} \frac{\partial \mathbf{f}}{\partial x} + \frac{\partial \mathbf{g}}{\partial y} + \frac{\partial \mathbf{h}}{\partial z}\partial\Omega \qquad \text{(A.3)}$$

Substituting Eqs. (A.2) and (A.3) into Eq. (A.1), the conservative integral form of the Euler equations in Cartesian coordinate x, y, z can be written as :

$$\iiint_{\Omega} \frac{\partial \mathrm{q}}{\partial t} d\Omega + \iiint_{\Omega} \left(\frac{\partial \mathrm{f}}{\partial x} + \frac{\partial \mathrm{g}}{\partial y} + \frac{\partial \mathrm{h}}{\partial z}\right) d\Omega = 0 \qquad \text{(A.4)}$$

$$\iiint_{\Omega} \left(\frac{\partial \mathrm{q}}{\partial t} + \frac{\partial \mathrm{f}}{\partial x} + \frac{\partial \mathrm{g}}{\partial y} + \frac{\partial \mathrm{h}}{\partial z}\right) d\Omega = 0 \qquad \text{(A.5)}$$

Since the finite control volume is arbitrarily drawn in space, the only way for the integral in Eq. (A.5) to equal zero is for the integrand to be zero at every point within the control volume. Hence, the Euler equations can be written the conservative differential form in Cartesian coordinate system as follows:

$$\frac{\partial \mathbf{q}}{\partial t}+\frac{\partial \mathbf{f}}{\partial x}+\frac{\partial \mathbf{g}}{\partial y}+\frac{\partial \mathbf{h}}{\partial z}=0 \tag{A.6}$$

Furthermore, to obtain the conservative differential of Euler equations in Curvilinear coordinate used in the flow solver of this study, a coordinate transformation from the Cartesian coordinate system x, y and z to the curvilinear coordinate system ξ, η, and ζ, called as Jacobian transformation is required. The time and space derivatives based on the Cartesian coordinate system can be defined as derivatives in the curvilinear system as follows:

$$\frac{\partial}{\partial t}=\xi_t\frac{\partial}{\partial \xi}+\eta_t\frac{\partial}{\partial \eta}+\zeta_t\frac{\partial}{\partial \zeta}+\frac{\partial}{\partial \tau} \tag{A.7}$$

$$\frac{\partial}{\partial x}=\xi_x\frac{\partial}{\partial \xi}+\eta_x\frac{\partial}{\partial \eta}+\zeta_x\frac{\partial}{\partial \zeta} \tag{A.8}$$

$$\frac{\partial}{\partial y}=\xi_y\frac{\partial}{\partial \xi}+\eta_y\frac{\partial}{\partial \eta}+\zeta_y\frac{\partial}{\partial \zeta} \tag{A.9}$$

$$\frac{\partial}{\partial z}=\xi_z\frac{\partial}{\partial \xi}+\eta_z\frac{\partial}{\partial \eta}+\zeta_z\frac{\partial}{\partial \zeta} \tag{A.10}$$

Substituting Eqs. (A.7) to (A.10) into Eq. (A.6), the Euler equation in curvilinear coordinate system can be written as:

$$\frac{\partial \mathbf{q}}{\partial \tau}+\xi_t\frac{\partial \mathbf{q}}{\partial \xi}+\eta_t\frac{\partial \mathbf{q}}{\partial \eta}+\varsigma_t\frac{\partial \mathbf{q}}{\partial \zeta}+\xi_x\frac{\partial \mathbf{f}}{\partial \xi}+\eta_x\frac{\partial \mathbf{f}}{\partial \eta}+\varsigma_x\frac{\partial \mathbf{f}}{\partial \zeta}+$$

$$\xi_y \frac{\partial \mathbf{g}}{\partial \xi} + \eta_y \frac{\partial \mathbf{g}}{\partial \eta} + \zeta_y \frac{\partial \mathbf{g}}{\partial \zeta} + \xi_z \frac{\partial \mathbf{h}}{\partial \xi} + \eta_z \frac{\partial \mathbf{h}}{\partial \eta} + \zeta_z \frac{\partial \mathbf{h}}{\partial \zeta} = 0 \qquad \text{(A.11)}$$

All space and time derivative terms in Eq. (A.11) are now in curvilinear coordinate system, but there are metrics still stated in the Cartesian coordinate system. The following metric transformations are required:

$$\begin{aligned}
\xi_x &= J^{-1}\left(y_\eta z_\zeta - z_\eta y_\zeta\right), & \xi_y &= J^{-1}\left(z_\eta x_\zeta - x_\eta z_\zeta\right), \\
\xi_z &= J^{-1}\left(x_\eta y_\zeta - y_\eta x_\zeta\right), & \xi_t &= -x_\tau \xi_x - y_\tau \xi_y - z_\tau \xi_z, \\
\eta_x &= J^{-1}\left(z_\xi y_\zeta - y_\xi z_\zeta\right), & \eta_y &= J^{-1}\left(x_\xi z_\zeta - z_\xi x_\zeta\right), \\
\eta_z &= J^{-1}\left(x_\zeta y_\xi - y_\zeta x_\xi\right), & \eta_t &= -x_\tau \eta_x - y_\tau \eta_y - z_\tau \eta_z, \\
\zeta_x &= J^{-1}\left(y_\xi z_\eta - z_\xi y_\eta\right), & \zeta_y &= J^{-1}\left(x_\eta z_\xi - z_\eta x_\xi\right), \\
\zeta_z &= J^{-1}\left(x_\xi y_\eta - y_\xi x_\eta\right), & \zeta_t &= -x_\tau \zeta_x - y_\tau \zeta_y - z_\tau \zeta_z,
\end{aligned} \qquad \text{(A.12)}$$

and J is the determinant of the Jacobian of the coordinate transformation:

$$\begin{aligned}
J &= \frac{\partial(x,y,z,t)}{\partial(\xi,\eta,\zeta,t)} \\
&= x_\xi\left(y_\eta z_\zeta - z_\eta y_\zeta\right) - y_\xi\left(x_\eta z_\zeta - z_\eta x_\zeta\right) + z_\xi\left(x_\eta y_\zeta - y_\eta x_\zeta\right)
\end{aligned} \qquad \text{(A.13)}$$

By first multiplying the conservative of Euler equations in Eq. (A.11) with Jacobian determinant, J the compact conservative differential form of the Euler equations can be obtained:

$$\begin{aligned}
&\frac{\partial}{\partial \tau}(J\mathbf{q}) + \frac{\partial}{\partial \xi}\left[J\left(\xi_t \mathbf{q} + \xi_x \mathbf{f} + \xi_y \mathbf{g} + \xi_z \mathbf{h}\right)\right] + \\
&\qquad \frac{\partial}{\partial \eta}\left[J\left(\eta_t \mathbf{q} + \eta_x \mathbf{f} + \eta_y \mathbf{g} + \eta_z \mathbf{h}\right)\right] + \\
&\qquad \frac{\partial}{\partial \zeta}\left[J\left(\zeta_t \mathbf{q} + \zeta_x \mathbf{f} + \zeta_y \mathbf{g} + \zeta_z \mathbf{h}\right)\right] = 0
\end{aligned} \qquad \text{(A.14)}$$

The Eq. (A.14) also can be written as

$$\frac{\partial \mathbf{Q}}{\partial \tau}+\frac{\partial \mathbf{F}}{\partial \xi}+\frac{\partial \mathbf{G}}{\partial \eta}+\frac{\partial \mathbf{H}}{\partial \zeta}=0 \tag{A.15}$$

with the vector of conservative variables $\mathbf{Q} = J\,(\rho,\ \rho u,\ \rho v,\ \rho w,\ e\ )^{\mathrm{T}}$. The inviscid fluxes $\mathbf{F}$, $\mathbf{G}$ and $\mathbf{H}$ in the ξ-, η- and ζ- direction, respectively:

$$\mathbf{F} = J\begin{pmatrix} \rho U \\ \rho u U+\xi_x p \\ \rho v U+\xi_y p \\ \rho w U+\xi_z p \\ U(e+p)-\xi_t p \end{pmatrix}$$

$$\mathbf{G} = J\begin{pmatrix} \rho V \\ \rho u V+\eta_x p \\ \rho v V+\eta_y p \\ \rho w V+\eta_z p \\ V(e+p)-\eta_t p \end{pmatrix} \tag{A.16}$$

$$\mathbf{H} = J\begin{pmatrix} \rho W \\ \rho u W+\zeta_x p \\ \rho v W+\zeta_y p \\ \rho w W+\zeta_z p \\ W(e+p)-\zeta_t p \end{pmatrix}$$

The velocities in curvilinear coordinate (the contravariant velocities) are states

$$\begin{aligned} U &= \xi_x u+\xi_y v+\xi_z w+\xi_t \\ V &= \eta_x u+\eta_y v+\eta_z w+\eta_t \\ W &= \zeta_x u+\zeta_y v+\zeta_z w+\zeta_t \end{aligned} \tag{A.17}$$

APPENDIX B
EULER EQUATIONS FORMULATED FOR MOVING GRIDS

In the cases of the unsteady stage separation of the two-stage space vehicle, it is necessary to solve the governing equations on a moving grid. The most popular methodologies used to tackle such a problem, are the Arbritary Lagrangian Eulerian (ALE) formulation [81][82] and the dynamic grids [83][84][85]. Both approaches are closely related and lead to the same modified form of the governing equations which accounts for the relative motion of the grid with respect to the fluid. In the present study, the dynamic grid approach is utilized.

Written in time-dependent integral form for a moving and /or deforming control volume with a surface element *dS*, the Euler Eq. (II.1) read

$$\frac{\partial}{\partial t}\iiint_{\Omega}\mathbf{q}\,d\Omega+\iint_{s}\left[\left(\mathbf{f}^{\mathbf{M}}\right)\cdot n_x+\left(\mathbf{g}^{\mathbf{M}}\right)\cdot n_y+\left(\mathbf{h}^{\mathbf{M}}\right)\cdot n_z\right]dS=0 \qquad \text{(B.1)}$$

The vector of the conservative variables **q** has the following components

$$\mathbf{q}=\begin{bmatrix}\rho\\ \rho u\\ \rho v\\ \rho w\\ e\end{bmatrix}, \qquad \text{(B.2)}$$

where ρ, u, v, w, e, and p denote the density, the Cartesian velocity components and the internal energy, respectively. The velocity of the deformation of cells is considered in the unsteady Euler Equation as follows

$$\begin{aligned}\mathbf{f}^{\mathbf{M}}&=\mathbf{f}-\dot{\mathbf{x}}\mathbf{q}\\ \mathbf{g}^{\mathbf{M}}&=\mathbf{g}-\dot{y}\mathbf{q}\\ \mathbf{h}^{\mathbf{M}}&=\mathbf{h}-\dot{\mathbf{z}}\mathbf{q}\end{aligned} \qquad \text{(B.3)}$$

with $\dot{x}$, $\dot{y}$ and $\dot{z}$ being the contravariant velocity components of the face of the control volume

$$\begin{aligned}\dot{\mathbf{x}} &= \frac{\partial x}{\partial t} \\ \dot{\mathbf{y}} &= \frac{\partial y}{\partial t} \\ \dot{\mathbf{z}} &= \frac{\partial z}{\partial t}\end{aligned} \tag{B.4}$$

The contravariant velocities in curvilinear coordinate for the Euler equations in Eq. (II.10) can be written as

$$\begin{aligned} U &= \xi_x(u-\dot{x})+\xi_y(v-\dot{y})+\xi_z(w-\dot{z})+\xi_t \\ V &= \eta_x(u-\dot{x})+\eta_y(u-\dot{x})+\eta_z(u-\dot{x})+\eta_t \\ W &= \zeta_x(u-\dot{x})+\zeta_y(u-\dot{x})+\zeta_z(u-\dot{x})+\zeta_t \end{aligned} \tag{B.5}$$

It was first pointed out by Thomas and Lombard [86] that besides the conservation of mass, momentum and energy, the so called Geometric Conservation Law (GCL) must be satisfied in order to avoid errors induced by deformation of control volumes [87][88][89]. The integral form of the GCL are written as

$$\frac{\partial}{\partial t}\int_{\Omega} d\Omega - \iint_{S}\left[n_x\cdot\dot{\mathbf{x}} + n_y\cdot\dot{\mathbf{y}} + n_z\cdot\dot{\mathbf{z}}\right]dS = 0 \tag{B.6}$$

The computation of the control volumes of the grid velocities must be performed in such a way that the resulting numerical scheme preserves the state of a uniform flow, independently of the deformation of the grid [87]. The GCL is automatically satisfied for such moving grids, where the shapes of the control volumes do not changes in time.

APPENDIX C

Transfinite Interpolation Algorithms for Grid Generation

Transfinite interpolation (TFI) is an interpolation procedure applied for algebraic grid generation to provide complete conformity of grids to boundaries in physical domains. It transforms from a rectangular computational domain to an arbitrarily shape physical domain which a physical grid is constrained to lie on or within specified boundaries. In addition, the grid spacing can be controlled directly. The transfinite interpolation was first introduced by William Gordon in 1973 [90] and was used by Lars Eriksson for application to grid generation for computational fluid dynamics (CFD) [53].

The essence of TFI is the specification of univariate interpolation in each of the computational coordinate directions, the forming of the tensor products of the interpolations and finally the summation of Boolean [91]. The univariate interpolations are a linear combination of known information in the physical domain including position and derivatives of the computational coordinate and coefficients. In addition, The blending functions of the coefficients has independent variable specified by the computaional coordinate. The general expressions of the univariate interpolations for three dimensions are

$$\begin{aligned}
\mathbf{U}(\xi,\eta,\zeta) &= \sum_{i=1}^{L}\sum_{n=0}^{P}\alpha_i^n(\xi)\frac{\partial^n \mathbf{X}(\xi_i,\eta,\zeta)}{\partial \xi^n} \\
\mathbf{V}(\xi,\eta,\zeta) &= \sum_{j=1}^{M}\sum_{m=0}^{Q}\beta_j^m(\eta)\frac{\partial^m \mathbf{X}(\xi,\eta_j,\zeta)}{\partial \eta^m} \\
\mathbf{W}(\xi,\eta,\zeta) &= \sum_{k=1}^{N}\sum_{l=0}^{R}\gamma_k^l(\zeta)\frac{\partial^l \mathbf{X}(\xi,\eta,\zeta_k)}{\partial \zeta^l}
\end{aligned} \tag{C.1}$$

Conditions on the blending functions are

$$\frac{\partial^{\bar{n}}\alpha_i^n(\xi_i)}{\partial\xi^{\bar{n}}}=\delta_{i\bar{i}}\delta_{n\bar{n}} \qquad \frac{\partial^{\bar{m}}\beta_j^m(\eta_j)}{\partial\eta^{\bar{m}}}=\delta_{j\bar{j}}\delta_{m\bar{m}} \qquad \frac{\partial^{\bar{l}}\gamma_k^l(\zeta_k)}{\partial\zeta^{\bar{l}}}=\delta_{k\bar{k}}\delta_{l\bar{l}} \tag{C.2}$$

$$\bar{i}=1,2,\cdots,L \qquad \bar{j}=1,2,\cdots,M \qquad \bar{k}=1,2,\cdots,N$$
$$\bar{n}=1,2,\cdots,P \qquad \bar{m}=1,2,\cdots,Q \qquad \bar{l}=1,2,\cdots,R$$

The forming of the tensor product of the univariate interpolations are performed as follows:

$$\begin{aligned}
\mathbf{UW}=\mathbf{WU}&=\sum_{i=1}^{L}\sum_{k=1}^{N}\sum_{l=0}^{R}\sum_{n=0}^{P}\alpha_i^n(\xi)\gamma_k^l(\zeta)\frac{\partial^{ln}\mathbf{X}(\xi_i,\eta,\zeta_k)}{\partial\zeta^l\partial\xi^n}\\
\mathbf{UV}=\mathbf{VU}&=\sum_{i=1}^{L}\sum_{j=1}^{M}\sum_{m=0}^{Q}\sum_{n=0}^{P}\alpha_i^n(\xi)\beta_j^m(\eta)\frac{\partial^{nm}\mathbf{X}(\xi_i,\eta_j,\zeta)}{\partial\eta^m\partial\xi^n}\\
\mathbf{VW}=\mathbf{WV}&=\sum_{j=1}^{M}\sum_{k=1}^{N}\sum_{m=0}^{Q}\sum_{l=0}^{R}\beta_j^m(\xi)\gamma_k^l\frac{\partial^{lm}\mathbf{X}(\xi,\eta_j,\zeta_k)}{\partial\zeta^l\partial\xi^m}\\
\mathbf{UVW}&=\sum_{i=1}^{L}\sum_{j=1}^{M}\sum_{k=1}^{N}\sum_{l=0}^{R}\sum_{m=0}^{Q}\sum_{n=0}^{P}\alpha_i^n(\xi)\beta_j^m(\eta)\gamma_k^l(\zeta)\frac{\partial^{lmn}\mathbf{X}(\xi_i,\eta_j,\zeta_k)}{\partial\zeta^l\partial\eta^m\partial\xi^n}
\end{aligned} \tag{C.3}$$

The boolean sum of the three insterpolations is

$$\mathbf{X}(\xi,\eta,\zeta)=\mathbf{U}\oplus\mathbf{V}\oplus\mathbf{W}=\mathbf{U}+\mathbf{V}+\mathbf{W}-\mathbf{UV}-\mathbf{UW}-\mathbf{VW}+\mathbf{UVW} \tag{C.4}$$

The simple TFI can be derived from the Eqs. (C.1) – (C.4) using linear interpolation functions for all coordinate directions and specify the positional data of the six bounding surfaces, namely taking $P=Q=R=0$ and $L=M=N=2$ in Eq. (C.1). The linear blending functions that satisfy the δ function condtions in Eq. (C.2) are

$$\begin{aligned}
\alpha_1^0(\xi)&=1-\xi\\
\alpha_2^0(\xi)&=\xi\\
\beta_1^0(\eta)&=1-\eta\\
\beta_2^0(\eta)&=\eta
\end{aligned} \tag{C.5}$$

$$\gamma_1^0(\zeta) = 1 - \zeta$$
$$\gamma_2^0(\zeta) = \zeta$$

The univariate interpolations and tensor products are

$$\mathbf{U}(\xi_I, \eta_J, \zeta_K) = (1-\xi_I)\,\mathbf{X}(0, \eta_J, \zeta_K) + \xi_I\,\mathbf{X}(1, \eta_J, \zeta_K)$$
$$\mathbf{V}(\xi_I, \eta_J, \zeta_K) = (1-\eta_J)\,\mathbf{X}(\xi_I, 0, \zeta_K) + \eta_J\,\mathbf{X}(\xi_I, 1, \zeta_K)$$
$$\mathbf{W}(\xi_I, \eta_J, \zeta_K) = (1-\zeta_K)\,\mathbf{X}(\xi_I, \eta_J, 0) + \zeta_K\,\mathbf{X}(\xi_I, \eta_J, 1)$$
$$\mathbf{UW}(\xi_I, \eta_J, \zeta_K) = (1-\xi_I)(1-\zeta_K)\,\mathbf{X}(0, \eta_J, 0) + (1-\xi_I\,\zeta_K)\,\mathbf{X}(0, \eta_J, 1)$$
$$+ \xi_I(1-\zeta_K)\,\mathbf{X}(1, \eta_J, 0) + \xi_I\,\zeta_K\,\mathbf{X}(1, \eta_J, 1)$$
$$\mathbf{UV}(\xi_I, \eta_J, \zeta_K) = (1-\xi_I)(1-\eta_J)\,\mathbf{X}(0, 0, \zeta_K) + (1-\xi_I)\eta_J\,\mathbf{X}(0, 1, \zeta_K)$$
$$+ \xi_I(1-\eta_J)\,\mathbf{X}(1, 0, \zeta_K) + \xi_I\,\eta_J\,\mathbf{X}(1, 1, \zeta_K)$$
$$\mathbf{VW}(\xi_I, \eta_J, \zeta_K) = (1-\eta_J)(1-\zeta_K)\,\mathbf{X}(\xi_I, 0, 0) + (1-\eta_J)\zeta_K\,\mathbf{X}(\xi_I, 1, 0)$$
$$+ \eta_J(1-\zeta_K)\,\mathbf{X}(\xi_I, 0, 1) + \eta_J\,\zeta_K\,\mathbf{X}(\xi_I, 1, 1)$$
$$\mathbf{UVW}(\xi_I, \eta_J, \zeta_K) = (1-\xi_I)(1-\eta_J)(1-\zeta_K)\,\mathbf{X}(0,0,0) +$$
$$+ (1-\xi_I)(1-\eta_J)\zeta_K\,\mathbf{X}(0,0,1) + (1-\xi_I)\eta_J(1-\zeta_K)\,\mathbf{X}(0,1,0)$$
$$+ \xi_I(1-\eta_J)(1-\zeta_K)\,\mathbf{X}(1,0,0) + (1-\xi_I)\eta_J\,\zeta_K\,\mathbf{X}(0,1,1)$$
$$+ \xi_I(1-\eta_J)\zeta_K\,\mathbf{X}(1,0,1) + \xi_I\,\eta_J(1-\zeta_K)\,\mathbf{X}(1,1,0)$$
$$+ \xi_I\,\eta_J\,\zeta_K\,\mathbf{X}(1,1,1) \qquad \text{(C.6)}$$

Using, the Boolean sum in Eq. (C.4), the expression for a transfinite interpolation grid ($I = 1, \ldots, \hat{I}$, $J = 1, \ldots, \hat{J}$, $K = 1, \ldots, \hat{K}$) with linear interpolation functions can be written as:

$$\mathbf{X}(\xi_I, \eta_J, \zeta_K) = \mathbf{U}(\xi_I, \eta_J, \zeta_K) + \mathbf{V}(\xi_I, \eta_J, \zeta_K) + \mathbf{W}(\xi_I, \eta_J, \zeta_K)$$
$$- \mathbf{UW}(\xi_I, \eta_J, \zeta_K) - \mathbf{UV}(\xi_I, \eta_J, \zeta_K)$$
$$- \mathbf{VW}(\xi_I, \eta_J, \zeta_K) + \mathbf{UVW}(\xi_I, \eta_J, \zeta_K) \qquad \text{(C.7)}$$

APPENDIX D

Poisson and Laplace Algorithms for Grid Generation

The grid generation system of elliptic second-order partial differential equations are so-called Poisson systems with control functions to be specified producing the best possible grids in the sense of smoothness and grid point distribution [30]. The complete three dimensional representation of the Poisson's equation can be written [7]:

$$\begin{aligned} &g^{11}\left(\mathbf{r}_{\xi\xi}+\mathbf{P}\mathbf{r}_{\xi}\right)+g^{22}\left(\mathbf{r}_{\eta\eta}+\mathbf{Q}\mathbf{r}_{\eta}\right)+g^{33}\left(\mathbf{r}_{\zeta\zeta}+\mathbf{R}\mathbf{r}_{\zeta}\right)+ \\ &2\left(g^{12}\mathbf{r}_{\xi\eta}+g^{23}\mathbf{r}_{\eta\zeta}+g^{13}\mathbf{r}_{\xi\zeta}\right)=0 \end{aligned} \tag{D.1}$$

By assuming orthogonal at the boundary, the contravariant metric coefficients g^{ij} with i ≠ j can be set be equal to zero, thus the term with the mixed partial derivatives in Eq. (D.1) can be cancelled away:

$$g^{11}\left(\mathbf{r}_{\xi\xi}+\mathbf{P}r_{\xi}\right)+g^{22}\left(\mathbf{r}_{\eta\eta}+\mathbf{Q}\mathbf{r}_{\eta}\right)+g^{33}\left(\mathbf{r}_{\zeta\zeta}+\mathbf{R}\mathbf{r}_{\zeta}\right)=0 \tag{D.2}$$

The contravariant metric coefficients in Eq. (D.1) can be expressed in the covariant metric ones, namely:

$$g^{11}=g_{22}\,g_{33}\quad,\ g^{22}=g_{33}\,g_{11}\quad,\ g^{33}=g_{11}\,g_{22} \tag{D.3}$$

where

$$g_{11}=\left|r_{\xi}\right|^{2}\quad,\ g_{22}=\left|r_{\eta}\right|^{2}\quad,\ g_{33}=\left|r_{\zeta}\right|^{2}$$

The derivatives with respect to the curvilinear coordinated are represented by second order finite difference as follows

$$x_{\xi}^{m}\approx 0{,}5\cdot\left(x_{i+1,j,k}^{m}-x_{i-1,j,k}^{m}\right)$$

$$
\begin{aligned}
x_{\eta}^{m} &\approx 0{,}5 \cdot \left(x_{i,j+1,k}^{m} - x_{i,j-1,k}^{m}\right) \\
x_{\zeta}^{m} &\approx 0{,}5 \cdot \left(x_{i,j,k+1}^{m} - x_{i,j,k-1}^{m}\right) \\
x_{\xi\xi}^{m} &\approx x_{i+1,j,k}^{m} - 2\,x_{i,j,k}^{m} + x_{i-1,j,k}^{m} \\
x_{\eta}^{m} &\approx x_{i,j+1,k}^{m} - 2\,x_{i,j,k}^{m} + x_{i,j-1,k}^{m} \\
x_{\zeta}^{m} &\approx x_{i,j,k+1}^{m} - 2\,x_{i,j,k}^{m} + x_{i,j,k-1}^{m}
\end{aligned}
\tag{D.4}
$$

By rearranging the differential equation of Poisson in Eq. (D.2) and applying the derivatives in Eq. (D.4), the iterative solution for obtaining physical grid points can be expressed as:

$$
\begin{aligned}
x_{i,j,k}^{m} = \frac{1}{2\left(g^{11}+g^{22}+g^{33}\right)} \Big[& g^{11}\left(x_{i+1,j,k}^{m}\left(1+0{,}5\mathbf{P}\right) + x_{i-1,j,k}^{m}\left(1-0{,}5\mathbf{P}\right)\right) \\
& + g^{22}\left(x_{i,j+1,k}^{m}\left(1+0{,}5\mathbf{Q}\right) + x_{i,j-1,k}^{m}\left(1-0{,}5\mathbf{Q}\right)\right) \\
& + g^{33}\left(x_{i,j,k+1}^{m}\left(1+0{,}5\mathbf{R}\right) + x_{i,j,k-1}^{m}\left(1-0{,}5\mathbf{R}\right)\right)\Big]
\end{aligned}
\tag{D.5}
$$

The source terms **P**, **Q**, **R** are responsible for the motion of the grid lines and provide the control of grid point spacing and distribution. The source terms are at first calculated on the surfaces of every block by using orthogonal regularities obtained by inverting the Laplace's equation system. The Laplace's equation can be written as [7][30] :

$$
\begin{aligned}
\mathbf{P}_{\xi\xi} + \mathbf{P}_{\eta\eta} + \mathbf{P}_{\zeta\zeta} &= 0 \\
\mathbf{Q}_{\xi\xi} + \mathbf{Q}_{\eta\eta} + \mathbf{Q}_{\zeta\zeta} &= 0 \\
\mathbf{R}_{\xi\xi} + \mathbf{R}_{\eta\eta} + \mathbf{R}_{\zeta\zeta} &= 0
\end{aligned}
\tag{D.6}
$$

and the inverted equation can be expressed as:

$$\begin{aligned} \mathbf{P} &= \frac{X\,\xi_x + Y\,\xi_y + Z\,\xi_z}{-\,g^{11} D_\xi} \\ \mathbf{Q} &= \frac{X\,\eta_x + Y\,\eta_y + Z\,\eta_z}{-\,g^{'22} D_\eta} \\ \mathbf{R} &= \frac{X\,\zeta_x + Y\,\zeta_y + Z\,\zeta_z}{-\,g^{'33} D_\zeta} \end{aligned} \qquad \text{(D.7)}$$

with

$$\begin{aligned} X &= g^{11} x_{\xi\xi} + g^{'22} x_{\eta\eta} + g^{'33} x_{\eta\eta} \\ Y &= g^{11} y_{\xi\xi} + g^{'22} y_{\eta\eta} + g^{'33} y_{\eta\eta} \\ Z &= g^{11} z_{\xi\xi} + g^{'22} z_{\eta\eta} + g^{'33} z_{\eta\eta} \end{aligned} \qquad \text{(D.8)}$$

and the determinant *D*, by analogy to the Jaconian Matrix, can be determined as follows:

$$\begin{aligned} D_\xi &= x_\xi\,\xi_x + y_\xi\,\xi_y + z_\xi\,\xi_z \\ D_\eta &= x_\eta\,\eta_x + y_\eta\,\eta_y + z_\eta\,\eta_z \\ D_\zeta &= x_\zeta\,\zeta_x + y_\zeta\,\zeta_y + z_\zeta\,\zeta_z \end{aligned} \qquad \text{(D.9)}$$

On the surface of solid and far field mirror points the first off-body points are used to determine differentials which are used in calculating the source terms on the surface. Then, these surface source terms are smoothly distributed into inner points of every block by a Laplace algorithm. Finally, the point distribution in the whole computing region will be calculated using the algorithm of the Poisson in Eq. (D.5) iteratively until reaching a given convergence value.

APPENDIX E

UPWIND DISCRETIZATION SCHEME

E.1 Flux Vector Splitting

Flux Vector Splitting (FVS) is a method to split the inviscid flux into positive into positive and negative contributions. The first Flux Vector Splitting method was proposed by Steger [55]. In this method, the inviscid flux is split by separating the velocity ***a*** into a positive and a negative component as:

$$a = a^{+} + a^{-} \tag{E.1}$$

where $a^{+} = \frac{1}{2}\left(a + |a| \right)$ and $a^{-} = \frac{1}{2}\left(a - |a| \right)$ and discretize them using a backward and forward differencing, respectively. Although the method becomes popular, it contained a lack of differentiability of the flux at sonic and shock points causing a problem in the flow variables.

An ingenious direct solution of the discontinuity problem of Steger's splitting was introduced by van Leer. He splits the flux based on polynomial expansions in Mach number for which the requirement is put, amongst others, that no discontinuities are present. The mass flux, for example, may be written as function of Mach number as:

$$\mathbf{F_m} = \rho U = \rho M_{\xi}\, a \text{, where } M_{\xi} = \frac{U}{a} \tag{E.2}$$

where a is the speed of sound. With the conditions that $\mathbf{F} = \mathbf{F}^{+} + \mathbf{F}^{-}$ and that $\mathbf{F}$ be continuous at $M = \pm 1$ the proper choice would be:

$$\mathbf{F}_{\mathbf{m}}^{\pm} = \pm \frac{\rho a}{4}\left(M_{\xi} \pm 1 \right)^2 \tag{E.3}$$

The detailed description of the van Leer may be found in the original paper of van Leer [57] and in [41] and for applications with moving meshes it is

described in [82][84]. In the moving mesh case the Mach number defined in Eq. (IV.4) is the Mach number relative to the speed of the cell face, $M_\xi = \left[(u-\dot{x})\xi_x + (v-\dot{y})\xi_y + (w-\dot{z})\xi_z\right]/a$. The convective flux can be written as a function of M_ξ as follows:

$$\mathbf{F} = J\left|\nabla\xi\right| \begin{bmatrix} \rho\, a M_\xi \\ \rho\, u a M_\xi + \xi_x p \\ \rho\, v a M_\xi + \xi_y p \\ \rho\, w a M_\xi + \xi_z p \\ \rho\, E a M_\xi + p\left(a M_\xi - \xi_t\right) \end{bmatrix} \tag{E.4}$$

Following the approach of the van Leer flux for $\left|M_\xi\right| < 1$ is

$$\mathbf{F} = J\left|\nabla\xi\right|\mathbf{F}_\mathbf{m}^{\pm} \begin{bmatrix} 1 \\ \xi_x\left(-U \pm 2a\right)/\gamma + u \\ \xi_y\left(-U \pm 2a\right)/\gamma + v \\ \xi_z\left(-U \pm 2a\right)/\gamma + w \\ \left(\gamma U + \xi_t\left(\gamma - 1\right)\right)\left(-U + 2a\right)/\left(\gamma - 1\right) + 2a^2/\left(\gamma^2 - 1\right) + k \end{bmatrix} \tag{E.5}$$

where the mass flux $F_\mathbf{m}^{\pm}$ is taken from Eq. (E.3) and k is the kinetic energy per unit mass. For supersonic flow condition the flux return to its unsplit form:

$$\mathbf{F} = J \begin{bmatrix} \rho\, U \\ \rho\, u U + \xi_x p \\ \rho\, v U + \xi_y p \\ \rho\, w U + \xi_z p \\ \rho\, E U + p\left(U - \xi_t\right) \end{bmatrix} \tag{E.6}$$

Unfortunately the superiority of van Leer's splitting in capturing shock discontinuities does not extend to its performance in capturing contact discontinuities. This is due to the convective term which does not vanish when the contact discontinuity is at rest.

E.2 Flux Difference Splitting

Furthermore a more complicated concept than the flux vector splitting is the flux difference splitting. This obtains a very good performance in capturing the contact discontinuities. The first Flux Difference Splitting method was proposed by Gudonov [92]. The original Gudonov method is a semi-analytical method. In the Gudonov method, the fundamental solution is the Riemann problem solution of the flow in a shock tube, see Fig. E.1. At rest, $t \leq 0$, the pressure on the right side of the diaphragm is lower than the one on the left side. After the diaphragm breaks, a shock wave moves to the right, a contact discontinuity also moves to the right with different (lower) speed and an expansion fan moves to the left. The state at time $t > 0$ is a function of the initial state at $t = 0$, namely Q_L and Q_R. For a more detailed discussion about the Riemann problem is given in Ref. [25].

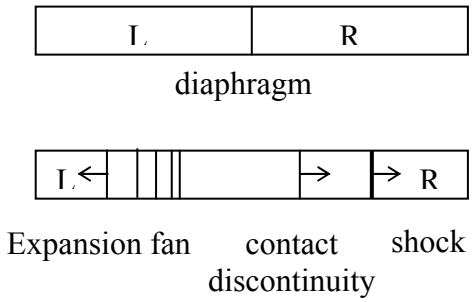

Figure E.1: Riemann's problem, shock tubes at rest and after the diaphragm has broken

The Gudonov method for solving a hyperbolic equation proceeds as follows. At a certain time level the discontinuous state of the flow is replaced by a piecewise constant distribution, see Fig. E.2. The state in a cell is obtained by averaging the values in a cell as:

$$Q_i = \frac{1}{\Delta x} \int_{i-\frac{1}{2}}^{i+\frac{1}{2}} Q(x,t)\,dx \qquad \text{(E.7)}$$

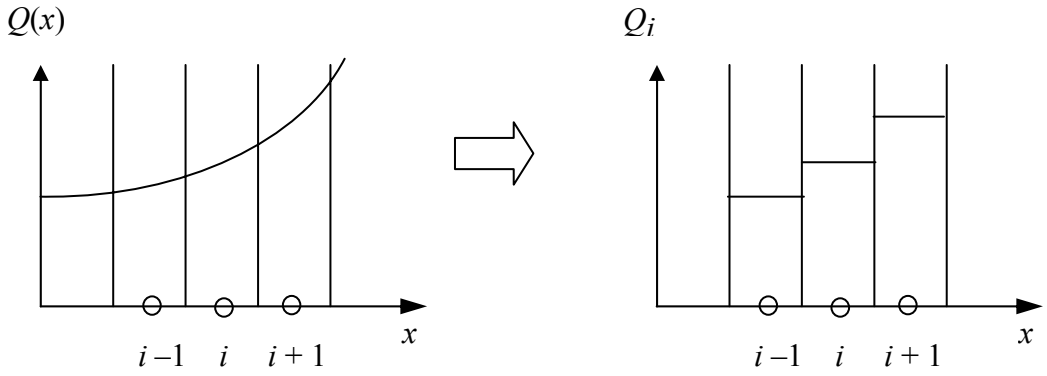

Figure E.2: Definition of discontinuity at cell faces in Gudonov's method

Consequently the outcome is a discontinuity at every cell face. These discontinuities are then considered as a Riemann problem with the cell faces as the diaphragm of a shock tube and the current time level as $t = 0$. For example: at cell face $i + \frac{1}{2}$ the states are $Q_L = Q_i$ and $Q_R = Q_{i+1}$. The state at the next time level is obtained by solving the Riemann problem at time $t = \Delta t$. This step is the physical step of the Gudonov method. After solving the Riemann problem, the state in a cell will obtain contributions from two neighboring cells. The state at the next time level in a cell is obtained by averaging these contributions. The averaging processes, the first and the third stage, are of numerical nature. They can be considered to be independent from the physical stage.

The exact solution of Riemann's problem for the Euler equations requires the solution of a set of nonlinear algebraic equations [33]. This is considered to be time consuming because it has to be done for each cell face. Hence, an approximate Riemann solver is usually applied which should be able to represent the important features of the problem, but less computational effort. This approach is also justified because even when using the exact Riemann solver, the solution is averaged in the cell. Up to now, the approximate Riemann solver which are considered to be the best and simplest are Roe's approximate Riemann solver [59].

APPENDIX F
Aerodynamic Force and Moment Coefficients Data Set for Steady Flows of Two-Stage Space Transport System with the Idealized Flat Plate

Aerodynamic Characteristics Data Set								
Mach = 4.04 **$\alpha / \Delta\alpha$ = 0/0** **h/l_{EOS} = 0.150**		CL		CD		Cm	
		exp	comp	exp	comp	exp	comp
accuracy	Grid (10^3)	**EOS vehicle**					
10^{-2}	113	-0.0115	-0.00939	0.0294	0.0269	-0.0041	-0.0107
10^{-3}	113		-0.01070		0.0262		-0.0109
3×10^{-4}	113		-0.01148		0.0264		-0.0110
10^{-3}	252		-0.01138		0.0273		-0.0104
10^{-3}	493		-0.01180		0.0277		-0.0106
Mach = 4.04 **Accuracy = 10^{-3}** **Grid = 493 x 10^3**		CL		CD		Cm	
		exp	comp	exp	comp	exp	comp
α	$\Delta\alpha$ / h/l_{EOS}	**EOS vehicle**					
0	0 / 0.225	-0.0120	-0.0127	0.0299	0.0277	-0.0059	-0.0084
0	3 / 0.225	0.0293	0.0263	0.0304	0.0283	-0.0062	-0.0071
$\alpha/\Delta\alpha$ = 0/0 **Accuracy = 10^{-3}** **Grid = 493 x 10^3**		CL		CD		Cm	
		exp	comp	exp	comp	exp	comp
Mach	h/l_{EOS}	**EOS vehicle**					
6.80	0.150	-	-0.01540	-	0.0222	-	-0.0093
7.90	0.150	-	-0.01541	-	0.0213	-	-0.0091

APPENDIX G
Aerodynamic Force and Moment Coefficients Data Set for Steady Flows of Full Configuration of Two-Stage Space Transport System

Aerodynamic Characteristics Data Set								
Mach = 4.04			C_L		C_D		Cm	
			exp	comp	exp	comp	exp	comp
α	$\Delta\alpha$	h/l_{EOS}	**EOS vehicle**					
0	0	0.225	0.0366	0.0292	0.0337	0.0293	-0.0072	-0.0073
3	0	0.225	0.0449	0.0398	0.0304	0.0308	-0.0057	-0.0095
0	2	0.225	0.0747	0.0626	0.0326	0.0322	-0.0069	-0.0147
0	5	0.225	0.1311	0.1104	0.0304	0.0368	-0.0082	-0.0259
0	0	0.325	0.0332	0.0225	0.0317	0.0287	-0.0137	-0.0161
α	$\Delta\alpha$	h/l_{EOS}	**ELAC 1C vehicle**					
0	0	0.225	-0.0491	-0.0504	0.0164	0.0133	0.0089	0.0077
3	0	0.225	-0.0026	-0.0061	0.014	0.0106	0.0145	0.0123
0	2	0.225	-0.0538	-0.0556	0.0164	0.0131	0.0105	0.0086
0	5	0.225	-0.0623	-0.0628	0.0163	0.0131	0.0133	0.0105
0	0	0.325	-0.0394	-0.0439	0.0164	0.013	0.0062	0.0057

APPENDIX H
Aerodynamic Force and Moment Coefficients of the Computational Data Set for Unsteady Flows

Computational Aerodynamic Characteristics Data Set					
EOS vehicle			**Ma = 4.04, α = 0.0 deg., k_{red} = 0.22**		
Time (s)	$\Delta\alpha$ (deg.)	h/l_{EOS}	CL	CD	Cm
0.000	2.000	0.125	0.0508	0.0341	-0.0122
0.017	2.025	0.126	0.0487	0.0338	-0.0124
0.033	2.098	0.130	0.0484	0.0337	-0.0123
0.050	2.218	0.136	0.0448	0.0334	-0.0115
0.066	2.382	0.144	0.0438	0.0335	-0.0102
0.083	2.586	0.154	0.0448	0.0336	-0.0088
0.099	2.824	0.166	0.0492	0.0338	-0.0084
0.116	3.092	0.180	0.0552	0.0340	-0.0086
0.132	3.382	0.194	0.0624	0.0342	-0.0093
0.149	3.687	0.209	0.0696	0.0345	-0.0101
0.165	4.000	0.225	0.0771	0.0348	-0.0117
0.182	4.313	0.241	0.0838	0.0352	-0.0130
0.198	4.618	0.256	0.0898	0.0356	-0.0144
0.215	4.908	0.270	0.0956	0.0363	-0.0154
0.231	5.176	0.284	0.1003	0.0368	-0.0164
0.248	5.414	0.296	0.1042	0.0373	-0.0177
0.264	5.618	0.306	0.1074	0.0378	-0.0187
0.281	5.782	0.314	0.1099	0.0382	-0.0193
0.297	5.902	0.320	0.1121	0.0385	-0.0198
0.314	5.975	0.324	0.1132	0.0387	-0.0199
0.330	6.000	0.325	0.1137	0.0388	-0.0200

Computational Aerodynamic Characteristics Data Set					
EOS vehicle			**Ma = 4.04, α = 0.0 deg., k_{red} = 0.50**		
Time (s)	$\Delta\alpha$ (deg.)	h/l_{EOS}	CL	CD	Cm
0.000	2.000	0.125	0.0607	0.0346	-0.0136
0.007	2.025	0.126	0.0577	0.0342	-0.0136
0.014	2.098	0.130	0.0494	0.0335	-0.0127
0.022	2.218	0.136	0.0448	0.0333	-0.0118
0.029	2.382	0.144	0.0416	0.0331	-0.0107
0.036	2.586	0.154	0.0394	0.0330	-0.0092
0.043	2.824	0.166	0.0399	0.0330	-0.0080
0.051	3.092	0.180	0.0435	0.0331	-0.0075
0.058	3.382	0.194	0.0487	0.0332	-0.0077
0.065	3.687	0.209	0.0549	0.0334	-0.0082
0.072	4.000	0.225	0.0609	0.0338	-0.0086
0.080	4.313	0.241	0.0678	0.0341	-0.0101
0.087	4.618	0.256	0.0745	0.0346	-0.0112
0.094	4.908	0.270	0.0806	0.0351	-0.0124
0.101	5.176	0.284	0.0861	0.0356	-0.0136
0.109	5.414	0.296	0.0912	0.0362	-0.0148
0.116	5.618	0.306	0.0957	0.0367	-0.0160
0.123	5.782	0.314	0.0995	0.0372	-0.0170
0.130	5.902	0.320	0.1029	0.0376	-0.0179
0.138	5.975	0.324	0.1055	0.0379	-0.0186
0.145	6.000	0.325	0.1077	0.0381	-0.0193

Computational Aerodynamic Characteristics Data Set					
EOS vehicle			**Ma = 4.04, α = 0.0 deg., k_{red} = 1.00**		
Time (s)	$\Delta\alpha$ (deg.)	h/l_{EOS}	CL	CD	Cm
0.000	2.000	0.125	0.0915	0.0362	-0.0174
0.004	2.025	0.126	0.0788	0.0353	-0.0163
0.007	2.098	0.130	0.0662	0.0344	-0.0149
0.011	2.218	0.136	0.0553	0.0336	-0.0135
0.014	2.382	0.144	0.0466	0.0330	-0.0121
0.018	2.586	0.154	0.0402	0.0326	-0.0106
0.022	2.824	0.166	0.0360	0.0323	-0.0092
0.025	3.092	0.180	0.0341	0.0321	-0.0079
0.029	3.382	0.194	0.0343	0.0319	-0.0070
0.033	3.687	0.209	0.0367	0.0320	-0.0065
0.036	4.000	0.225	0.0405	0.0321	-0.0063
0.040	4.313	0.241	0.0454	0.0323	-0.0066
0.043	4.618	0.256	0.0506	0.0327	-0.0070
0.047	4.908	0.270	0.0565	0.0331	-0.0079
0.051	5.176	0.284	0.0624	0.0336	-0.0091
0.054	5.414	0.296	0.0681	0.0341	-0.0102
0.058	5.618	0.306	0.0734	0.0347	-0.0113
0.062	5.782	0.314	0.0785	0.0352	-0.0124
0.065	5.902	0.320	0.0833	0.0358	-0.0135
0.069	5.975	0.324	0.0876	0.0362	-0.0145
0.072	6.000	0.325	0.0913	0.0366	-0.0155